

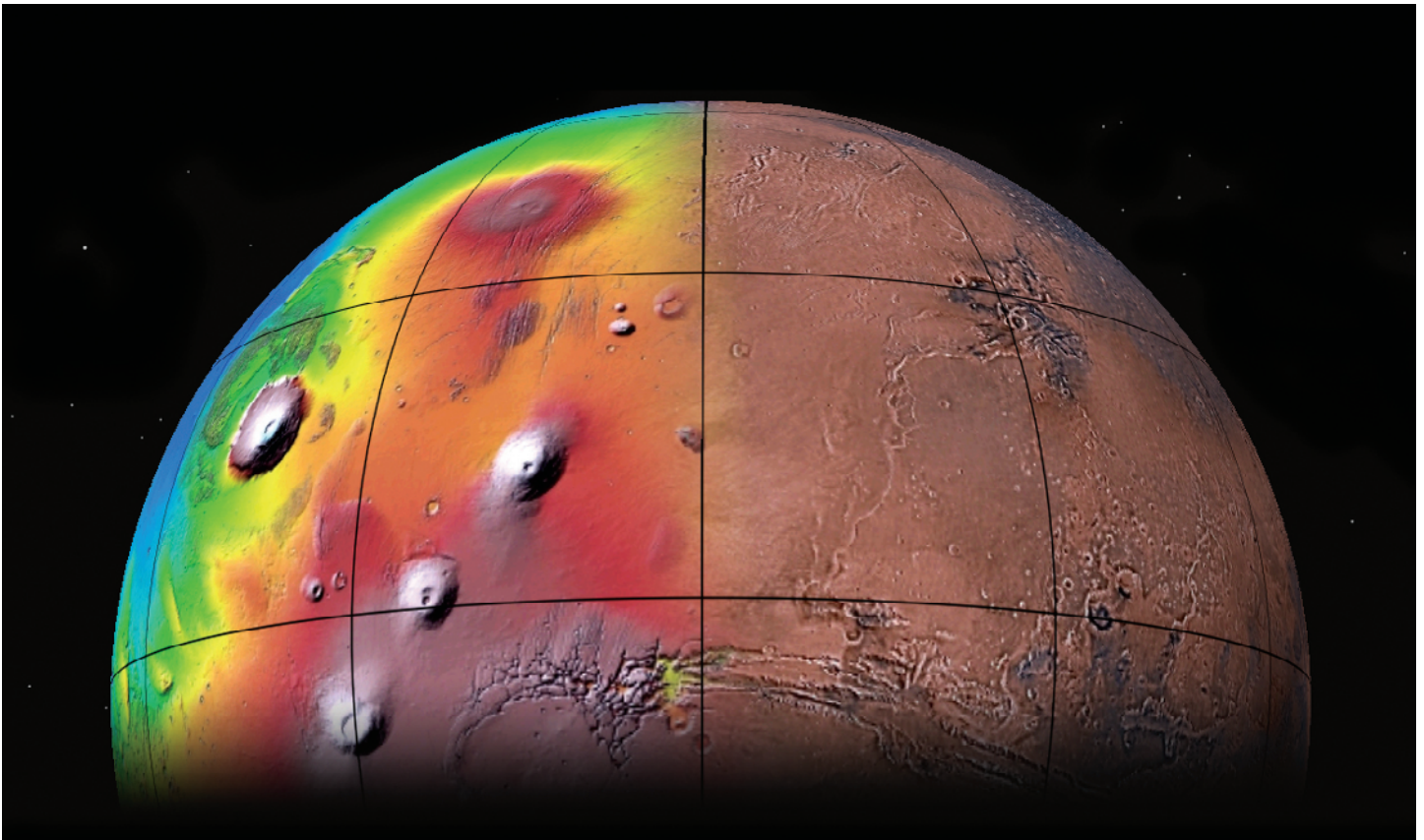
Prepared for the National Aeronautics and Space Administration

Geologic Map of Mars

By Kenneth L. Tanaka, James A. Skinner, Jr., James M. Dohm, Rossman P. Irwin, III, Eric J. Kolb, Corey M. Fortezzo, Thomas Platz, Gregory G. Michael, and Trent M. Hare

Pamphlet to accompany

Scientific Investigations Map 3292



View of the northern part of the western hemisphere of Mars. Left half shows a color elevation, shaded relief view highlighting the immense shields of the Tharsis rise. Right half shows a true-color view of the vast Valles Marineris and Kasei Valles canyon systems, which connect to the dark basin of Chryse Planitia at upper right. (*Image data from NASA.*)

2014

U.S. Department of the Interior
U.S. Geological Survey

This page intentionally left blank.

Contents

Introduction	1
Physiographic Setting	2
Data	3
Mapping Methods.....	3
Map Development and Author Roles	4
Unit Delineation.....	4
Unit Groups	5
Unit Names and Labels.....	5
Contact Types	5
Line Feature Types.....	6
Drafting	6
Age Determinations.....	6
Geologic History.....	9
Noachian Period	9
Early Noachian Epoch.....	10
Middle Noachian Epoch	10
Late Noachian Epoch	11
Hesperian Period	12
Early Hesperian Epoch.....	12
Late Hesperian Epoch	13
Amazonian Period.....	13
Early Amazonian Epoch	14
Middle Amazonian Epoch	14
Late Amazonian Epoch	15
Major Results.....	15
Acknowledgments	15
References Cited.....	16

Tables

1. Martian epoch lower boundary ages.....	25
2. Assigned model ages for selected Mars global map units	26
3. Total crater densities for map units on Mars	32
4. Impact craters and basins (and possible impact-like features of other origin) on Mars	34
5. Basis for time-stratigraphic assignments for each map unit as shown in the Correlation of Map Units.....	37
6. Percentages of previously mapped Viking-based map units for each unit in this Mars global map	39
7. Percentages of map units in this Mars global map for each previously mapped Viking-based map unit	41

This page intentionally left blank.

Introduction

Mars is the fourth planet from the Sun and the outermost of the rocky, terrestrial planets that make up the inner solar system. Of this planetary family, Mars is only larger than Mercury. Surface gravity on Mars is 3.71 m/s^2 , which is 37.6 percent that of the Earth's. The present atmospheric pressure is low ($\sim 0.6 \text{ kPa}$) relative to Earth's (101 kPa), and the atmosphere is mostly carbon dioxide (95%). The obliquity of Mars is presently 25° and may have varied by tens of degrees over the past tens of millions of years and longer (Laskar and others, 2004).

The Martian polar ice caps, observable from Earth, are made up mostly of water ice. Thus the possibilities of liquid water and habitable environments on or near the surface of Mars have driven interest in the planet (for example, Des Marais, 2010). Orbiting at a distance on average about 50 percent farther from the Sun than the Earth, Mars is the only other planet besides the Earth that is within the solar system's potential habitable zone (Kopparapu and others, 2013).

Beginning in the late 1960s with the Mariner 4, 6, and 7 fly-bys, spacecraft began imaging the planet from closer perspectives (Snyder and Moroz, 1992). Mariner 9 (1971–72) was the planet's first orbiter, and it successfully imaged the entire globe at 2 to 3 km/pixel resolution. These early spacecraft revealed the planet's Moon-like cratered highlands, immense volcanoes, huge tectonic rifts, and, strikingly, evidence for flowing water in the planet's ancient past, based on identification of branching valley network systems and broad outflow channels. The next major phase of spacecraft exploration in the late 1970s and early 1980s involved the two Viking Orbiters and two Viking Landers. The orbiters imaged the surface at tenfold to hundredfold increased detail, and the landers performed the first biological experiments in search of Martian life (*, Klein and others, 1992¹). The most recent phase of Mars exploration, since the late 1990s, has led to significant increase in the types, spatial resolution, and amount of data returned both from Mars orbit and the surface (*, Barlow, 2008; Bell, 2008). Post-Viking orbiters include Mars Global Surveyor, Mars Odyssey, Mars Express, and Mars Reconnaissance Orbiter. These have delivered high-resolution visible, thermal, and multispectral imaging; laser altimetry; radar, gravity, and magnetic sounding; and other measurements of the Martian surface, atmosphere, and crust. Rovers and stationary landers, including Mars Pathfinder, Spirit and Opportunity Mars Exploration Rovers, Mars Phoenix, and the Curiosity Mars Science Laboratory, have performed increasingly sophisticated surface investigations.

Each major phase of exploration has resulted in a global geologic map, which encapsulates the most significant advances in understanding of Martian surface evolution. The first global map of Mars was produced by Scott and Carr (1978) at a scale of 1:25,000,000 using Mariner 9 visible wavelength images (2–3 km/pixel resolution). That map included compilation of a partly completed, 30-quadangle, 1:5,000,000-scale geologic map series drafted by various authors. Scott and Carr (1978)

identified 24 global geologic units among 5 terrain groups and established the 3 principal time-stratigraphic divisions for Mars—the Noachian, Hesperian, and Amazonian Periods (from oldest to youngest). The second global map of Mars was published in three parts at a scale of 1:15,000,000. Western and eastern equatorial regions ($\text{lat} < 57^\circ$) were produced by Scott and Tanaka (1986) and Greeley and Guest (1987), respectively. Polar regions ($\text{lat} > 55^\circ$) were produced by Tanaka and Scott (1987). Viking Orbiter images mostly between 100 and 300 m/pixel resolution served as the bases for these maps, which identified 90 map units, including units of local to global extent. Some of these units were used as referents to subdivide the time-stratigraphic periods of Scott and Carr (1978) into epochs (Early, Middle, and Late Noachian; Early and Late Hesperian; and Early, Middle, and Late Amazonian), as well as to establish the crater-density values for their boundaries (Tanaka, 1986). Both the Mariner 9- and Viking-based geologic maps were originally drafted over shaded-relief-map bases that were manually airbrushed using reference images (Batson and others, 1979).

Herein, we present a new global geologic map of Mars, which records the distribution of geologic units and landforms on the planet's surface through time, based on unprecedented variety, quality, and quantity of remotely sensed data acquired since the Viking Orbiters. These data have provided morphologic, topographic, spectral, thermophysical, radar sounding, and other observations for integration, analysis, and interpretation in support of geologic mapping. In particular, the precise topographic mapping now available has enabled consistent morphologic portrayal of the surface for global mapping; whereas previously used visual-range image bases were less effective, because they combined morphologic and albedo information and, locally, atmospheric haze. Also, thermal infrared image bases used for the new map tended to be less affected by atmospheric haze, making them reliable for analysis of surface morphology and texture at even higher resolution than the topographic products. Moreover, following publication of the Viking-based global map of Mars, a multitude of geologic maps of different parts of the Martian surface at various scales using the Viking Orbiter and subsequent datasets were produced to address important questions regarding Martian surface geology and evolution; major results from these efforts, mostly at 1:1,000,000 and smaller (zoomed-out) scales, have been incorporated herein (the locations of these maps are shown in fig. 2). Finally, a host of other published studies have contributed to the interpretations and geologic reconstruction contained herein. To keep our reference list at a reasonable length, we precede some citation lists with an asterisk (*, see footnote 1) to indicate that other useful, particularly earlier, publications exist.

We used digital photogeologic mapping techniques to identify and discriminate 44 geologic units (encompassing $\sim 1,300$ separate occurrences) and 12 linear feature types ($> 3,500$ individual features mapped, not all shown on map, included in digital files), which collectively document major episodes of unit emplacement and modification. Along with cross-cutting relations, analysis of global as well as specific detailed impact crater size-frequency distributions provide an unprecedented documentation of relative and modeled absolute

¹An asterisk (*) is included where only a small sample, generally recent, of the many representative publications are cited.

ages of map units and their individual occurrences (see tables 1–3 and D1² at <http://pubs.usgs.gov/sim/3292/> and fig. 1), as well as chronostratigraphic ages for all impact craters and basins >150 km in diameter (table 4). Key stratigraphic relations and crater-density data are used to constrain the time-stratigraphic age assignments for each map unit as shown in the Correlation of Map Units; this information is summarized in table 5. Due to our focus on global (vs. regional) reconstructions, we avoid dividing units based upon modest regional variations in age and physical character. These efforts result in an improved characterization of Mars compared to the previous, Viking-based mapping (tables 6 and 7) and, therefore, provide a refined portrayal of Mars' geologic character and evolution.

Physiographic Setting

The global topography of Mars defines broad regions of geologic significance that include geographic names established by the International Astronomical Union (IAU). We include only names of major features and a representative selection of others mentioned herein; see the topographic map of Mars (U.S. Geological Survey, 2003) and the Gazetteer of Planetary Nomenclature (<http://planetarynames.wr.usgs.gov/>) for more detailed information about and portrayals of Martian geographic features.

Densely cratered, rugged highlands cover much of the southern latitudes and some parts of the northern hemisphere of Mars, including Arabia Terra, Terra Sabaea, and Tempe Terra. Most highlands are between 0 to 5,000 m above datum, which is defined at Mars' mean planetary radius (Smith and others, 1999, 2001). However, Arabia Terra and parts of other highland areas north of the equator lie at 0 to –3,000 m elevations. The northern plains lie even lower in elevation, mostly in the range of –4,000 to –5,000 m. They are much less cratered than the highlands, indicating that burial by younger rock and sediment sequences has obscured much of the earlier geologic record. The three largest, well-preserved impact basins in the Martian cratered highlands are Hellas basin (~2,400 km in diameter and includes the deepest surface point on the planet at –8,200 m elevation), Isidis basin (~1,500 km in diameter) along the highland-lowland margin, and Argyre basin (~900 km in diameter). Utopia Planitia forms the floor of a giant (nearly 3,000 km in diameter) circular basin northeast of Isidis Planitia, interpreted

by many to be an ancient impact basin (*, McGill, 1989). Other circular but generally less well defined broad depressions that also may be impact structures occur across Mars (*, Schultz and others, 1982; Frey, 2006).

The zone of transition between the Martian highlands to the south and the lowlands to the north (mostly –1,000 to –4,000 m) is marked by diverse landforms, including scarps, knobs, mesas, and plateaus that are hundreds of meters to a few kilometers in relief. These landforms extend from the southern margins of Acidalia Planitia eastward to the southern margin of Amazonis Planitia. A gigantic system of linear canyons, Valles Marineris, forms along the northern margin of the Thaumasia plateau and extends for >2,000 km from Noctis Labyrinthus along the eastern margin of the Tharsis rise. The canyon system connects to the east with chaotic fields of knobs and mesas that mark the source regions of the broad outflow channels of circum-Chryse; the channels dissect highland surfaces to depths of several kilometers over areas that extend a few thousand kilometers prior to their entrance into Chryse Planitia (*, Rotto and Tanaka, 1995), where the Viking 1 Lander and Mars Pathfinder sites occur (*, Golombek and others, 1997; Crumpler and others, 2001).

Regionally focused, long-lived volcanism resulted in the formation of high-standing and broad rises and shields, plateaus, and local edifices. The Tharsis rise (or region) consists of an immense assemblage of flow fields that extend 5,000 km east-west by 6,000 km north-south. The rise is capped by some of the largest volcanic constructs in the solar system, including Olympus Mons, Alba Mons, and the three aligned Tharsis Montes (Ascraeus Mons, Pavonis Mons, and Arsia Mons). In addition, the Tharsis rise includes fields of smaller volcanoes, as well as tectonically deformed, elevated terrains that include parts of Tempe Terra, Noctis Fossae, Claritas Fossae, Ceraunius Fossae, and the Thaumasia highlands (*, Tanaka and others, 1991; Dohm and others, 2001a). The summit of Olympus Mons stands at 21,229 m—the highest elevation on Mars—and the mountain is surrounded by several blocky, lobate aureoles that extend for hundreds of kilometers. Other regional volcanic centers include the Elysium rise (composed of Elysium Mons and surrounding volcanoes and lava-flow fields), Hesperia Planum and Malea Planum (northeast and southwest margins of Hellas Planitia, respectively), and Syrtis Major Planum (west margin of Isidis Planitia). Smaller volcanoes and volcano-like edifices ranging from tens to a few hundred kilometers in diameter are distributed across the southern highlands, with a particular concentration south of the Tharsis rise.

Both of the Martian poles are capped by plateaus that are elevated a few kilometers above the surrounding plains. The circular, north polar plateau—Planum Boreum—occurs near the geographic center and low point (approx. –5,000 m elevation) of the northern lowlands. Planum Boreum is ~1,000 km in diameter and is partly surrounded by vast dune fields, including Olympia Undae. The south polar plateau—Planum Australe—occurs within southern cratered highlands standing at 1,000 to 1,500 m elevation. Planum Australe has an ellipsoidal planimetric shape (~1,100 x 1,400 km). Both poles contain characteristic spiral troughs that expose the depths of the polar plateau,

²Table D1 is a Microsoft Excel spreadsheet file in .xlsx format available online only. This table provides a more complete presentation of the crater size-frequency data and results for the same 48 counting areas provided in table 2. The additional information includes total numbers of craters; whether a resurfacing correction was used; diameter ranges used for model crater size-frequency fits; numbers of craters in fit ranges; cumulative densities and density errors of craters >1 km in diameter per million km² for model-fit isochrons; actual cumulative crater densities for diameter steps at 0.5, 1, 2, 5, and 16 km; ratios of actual to expected values of cumulative densities, based on estimated densities projected from values at next larger diameter step; instrument that obtained the image data used; image numbers; and image resolutions.

including one large reentrant in the north (Chasma Boreale) and three reentrants in the south (Chasma Australe, Promethei Chasma, and Ultimium Chasma).

Data

The primary base maps for this geologic mapping investigation are the Mars Global Surveyor (MGS) Mars Orbiter Laser Altimeter (MOLA) digital elevation model (DEM) (463 m/pixel resolution at lower latitudes to 115 m/pixel near the poles) (Smith and others, 2001) and the Mars Odyssey (ODY) Thermal Emission Imaging System (THEMIS) daytime infrared (IR) image mosaic (100 m/pixel) (Christensen and others, 2004). Both data sets are registered to the spheroid of Mars, with an equatorial radius of 3,396.19 km and a polar radius of 3,376.2 km (Seidelmann and others, 2002). Longitude increases to the east, and latitude is planetocentric, in compliance with IAU (International Astronomical Union), International Association of Geodesy, NASA (National Aeronautics and Space Administration), and U.S. Geological Survey standards.

The MOLA-derived shaded-relief image used for the base represents more than 600 million single altimeter measurements gathered between 1999 and 2001, adjusted for consistency (Smith and others, 2001; Neumann and others, 2001, 2003), and converted to planetary radii values. Using these values, elevations above the areoid were determined from the Martian gravity field solution GMM-2B (Lemoine and others, 2001). The average accuracy of each point is originally ~100 m in horizontal position and ~1 m in radius (Neumann and others, 2001). However, the total elevation uncertainty is at least ± 3 m due to the global error in the areoid (± 1.8 m according to Lemoine and others, 2001) and regional uncertainties in its shape. The measurements were converted into a digital elevation model (DEM; Neumann and others, 2001) using Generic Mapping Tools software, with a resolution of 128 pixels/degree (or 463 m/pixel at the equator). The MOLA DEM does not contain data at lat $>88^\circ$ N. and S. due to the 92.8° inclination of the MGS orbit (Smith and others, 2001).

A shaded-relief image was generated from the DEM with a sun angle of 45° from horizontal and a sun azimuth of 335° , as measured clockwise from north.

The artificially illuminated MOLA DEM serves as the base for the printed geologic map. To provide a true global view on a single map sheet, Robinson projection was selected at 1:20,000,000 scale. Polar regions (lat $>70^\circ$ N. or S.) are represented in stereographic projection. The printed map scale forms the basis for determining the digital mapping parameters and the minimum size of mappable features, as discussed in the Mapping Methods section.

The THEMIS daytime and nighttime IR 100 m/pixel global mosaics (version 11; P.R. Christensen, N.S. Gorelick, G.L. Mehall, and K.C. Murray, THEMIS Public Data Releases, Planetary Data System node, Arizona State University, <http://themis-data.asu.edu>) represent thermal infrared energy emitted in nine wavelength bands, which relate to the temperature and emissivity of the surface (Christensen and others,

2004; Edwards and others, 2011). For the daytime mosaic, about 21,000 THEMIS daytime images were selected with the following parameters: shutter closing time <150 seconds, incidence angle $<85^\circ$, minimum surface temperature >160 K, and 0 percent saturated pixels from lat 90° S. to 90° N. with unsummed (full-resolution) data. For the nighttime mosaic, images were selected with the following parameters: shutter closing time <150 seconds, incidence angle $>95^\circ$, minimum surface temperature >160 K, and 0 percent saturated pixels from lat 75° S. to 75° N. with unsummed data. The daytime mosaic covers ~95 percent of the planet, with data gaps most common between lat 50° and 70° N. The daytime data are generally indicative of morphology, as temperature variations are dominated by surface orientations relative to solar incidence. The THEMIS IR nighttime mosaic covers the region within lat $\pm 60^\circ$ and has some missing data at the highest latitudes, resulting in about 80 percent total coverage of the planet. Nighttime IR data represent the thermal inertia of the surface materials, showing that brighter materials have cooled less and, thus, are likely composed of coarser-grained materials, indurated surfaces, and (or) bedrock (*, Ferguson and others, 2006; Putzig and Mellon, 2007). These data were used to assist in discriminating contacts in regions where the intrinsic thermal inertias of map units were not overly obscured or altered (Christensen and others, 2004).

Initial geologic mapping results using the base maps were verified and honed through integrating other data sets, including MOLA-derived products (especially color-shaded-relief and slope-detrended maps) and local, higher-resolution images via web-linked image footprints using geographic information system (GIS) software. Where available, higher-resolution images provided important information regarding unit texture and stratigraphic relations. In some instances, THEMIS visual range images (18 to 36 m/pixel) (Christensen and others, 2004) and Mars Reconnaissance Orbiter (MRO) Context Camera (CTX) images (5 to 6 m/pixel) (Malin and others, 2007) were consulted where THEMIS IR data are lacking or where identification of small features and textures on scales of tens of meters was required to confirm unit characteristics and to determine and (or) refine contact locations and stratigraphic relations. Other spacecraft data sets (for example, spectral and radar sounding) were not directly used for geologic mapping. Rather, we consulted and implemented published topical investigative results that relied on these types of data, as noted through citation, to help characterize and interpret map units and features and their relations that pertain to global geologic history.

Mapping Methods

Photogeologic mapping methods that are routinely employed to identify geologic units on Mars have a heritage in approaches applied to remotely sensed image and topographic data acquired through terrestrial and lunar sensors (*, Wilhelms, 1990; Smith and Pain, 2009). Geomorphic characteristics not only can be recognized in such data, but they generally are more ubiquitous, mappable, and interpretable with respect to the type, timing, and physical modification of bedrock geologic

materials than are compositional signatures and other data sets. The latter primarily reveal surficial information or very low resolution geophysical data that pertain to buried materials and structures (though all existing information informs on aspects of the geology of Mars). Geomorphic characteristics that are most useful to geologic mapping include stratigraphic relations (for example, layers, layer truncations, and unit embayments and (or) burial), lithologic properties (for example, impact, mass-wasting, and volcanic morphologies), and modification features (for example, tectonic, fluvial, and periglacial landforms). In addition, terrestrial photogeologic mapping studies based on simulated planetary data sets have applied ground truth to test the reliability of planetary photogeologic mapping approaches (*, Tanaka and others, 2009; Skinner and Fortezzo, 2013), leading to a conservative and defensible methodology that we employ here. With some minor refinement to defining crater-density boundaries (Werner and Tanaka, 2011; Michael, 2013), the eight-epoch chronology system of Tanaka (1986) is employed in the current map.

Map Development and Author Roles

The methods described in the following subsections chiefly result from (1) our collective experience mapping Mars (*, Scott and Tanaka, 1986; Tanaka and Scott, 1987; Dohm and others, 2001a; Tanaka and others, 2005; Skinner and Herkenhoff, 2012; Tanaka and Fortezzo, 2012; Irwin and Grant, 2013); (2) the state of the art in handling global mapping data sets using digital mapping technologies (see below); (3) methods used in recent terrestrial geologic maps at global (*, Bouysee, 2009) and continental (*, Reed and others, 2005) scales; (4) guidance provided by the Geologic Mapping Subcommittee of NASA's Planetary Geology and Geophysics Program and its Planetary Geologic Mapping Handbook (Tanaka and others, 2010); and (5) the application of the interrelated, guiding principles of consistency, simplicity, clarity, utility, and communicability as chosen by our mapping team.

The production of a global map necessitates spatial and categorical generalization of geologic units and features that would otherwise be mapped in more detail at larger scales (*, Varnes, 1974). These generalizations can be accommodated at the selected map scale by carefully balancing cartographic symbols and geologic descriptions. However, unlike many terrestrial examples of small-scale geologic maps (*, Bouysee, 2009), the map presented herein represents original mapping work, augmented with a variety of published topical science investigations, rather than the compilation and generalization of multiple larger-scale geologic map products.

The initial mapping of units and features by region was the responsibility of four of the authors: Tharsis region and Argyre basin (Dohm), northern lowlands and Arabia Terra (Skinner), southern highlands (Irwin), and south polar region and Hellas basin (Kolb). To establish consistency, the global-line-feature mapping and contact attributing were later given to a single mapper (Fortezzo). The entire map was edited and compiled under the direction of the lead author (Tanaka) through

iterative reviews with primary mappers as well as mapping team discussions, when the schemes for unit naming, grouping, and coloring, as well as for contact and line-feature attributing were developed. Outcrop unit assignments were based partly on age, which required determination of high-accuracy, local crater-density ages of type localities (Platz and Michael). To assist in global unit and outcrop age assignments, we compiled cumulative crater densities for all unit occurrences through a global crater database (Robbins and Hynek, 2012) (see Age Determinations section below). Data management and validation and GIS software oversight (Hare) ensured spatial accuracy and efficiency in mapping.

Unit Delineation

Map units identify temporally unique geologic materials of substantial thickness and extent for portrayal at map scale. Identifying characteristics that establish geologic uniqueness include primary (formational) morphology, IR brightness (daytime or nighttime), and (or) albedo characteristics from visual-range-image data, stratification, relative age, and spatial geologic associations, which are described in the Description of Map Units. Primary characteristics and landforms in this map include lobate scarps (identifying flow boundaries within or at the margin of a unit), layering (presence and thickness of layers), dunes, plains, and shields and cones (indicative of volcanic vents). The primary versus secondary (modification) nature of some morphologic features is uncertain, and defining units using secondary features was avoided (although they were commonly helpful in establishing time gaps between adjacent units, as well as typical modification history; they are noted in the additional characteristics column in the Description of Map Units). Our unit delineation approach thus differs from the previous global geologic maps of Mars, which included secondary morphologic and albedo features among the principal attributes of map units. For the Noachian units, we did not delineate Noachian crater ejecta within them, as shown in many other Mars geologic maps (*, Scott and Carr, 1978; Scott and Tanaka, 1986), because of the difficulty in many cases of identifying the limit of the ejecta plus the fact that most Noachian materials are interpreted to include impact ejecta.

Units are delineated by relative age as borne out by stratigraphic overlap and embayment relations, and their chronostratigraphic ages were determined by the densities of impact crater populations. Units were assigned ages according to the three periods previously defined by Scott and Carr (1978) and the eight epochs that the periods were later divided into by Tanaka (1986). Many units are likely to consist of complexly intermixed materials of contrasting age and provenance. Such intercalations are neither consistently observable nor possible to represent using regional to global data sets and small map scales. We ignored surficial materials that are estimated to be meters thick (or smaller), including dust, duricrust, desert pavement, and icy soils and mantles (*, Mustard and others, 2001; Putzig and Mellon, 2007). These generally are too thin to recognize and map at global scale. An exception is the approximately meter-thick Amazonian polar cap unit that constitutes

distinctively bright, mappable surfaces in the polar regions (*, Langevin and others, 2005; Tanaka and Fortezzo, 2012). Because of improvements not only in data resolution and quality but also in mapping approaches and thoroughness of crater dating, many unit exposures have improved age assignments with more consistent accuracy compared to those of the Viking-based global map (Scott and Tanaka, 1986; Greeley and Guest, 1987; Tanaka and Scott, 1987).

Unit Groups

Global and continental scale maps of Earth are necessarily made up of broadly inclusive units that can be grouped naturally, given their composition and (or) geographic occurrence. For example, in the “Geological Map of the World” (Bouysee, 2009), onshore and offshore areas make up the major unit groups, each consisting of lithologic divisions. Also, in the “Geological Map of North America” (Reed and others, 2005), materials are grouped lithologically as sedimentary, volcanic, plutonic, metamorphic, and undivided crystalline rock types. Both of these maps further divide the lowest-rank groups into units according to chronostratigraphic age.

Similarly, we employ a unit grouping scheme that uses both geographic setting and lithologic divisions for unit names and labels. Geographic setting consists of highland, lowland, transitional, basin, polar, and apron groups, all containing multiple units subdivided primarily by age and, in some cases, primary morphologic character. The lithologic units are composed of volcanic and impact (crater) categories. All groups (except the globally distributed impact unit) coincide closely with major geographic zones (see Physiographic Setting), and some groups typically have either low or high kilometer-scale roughness (Kreslavsky and Head, 2000; see Description of Map Units).

In contrast, the previous Viking-based global geologic map included formations and assemblages that, in some cases, distinguished materials of similar origin and age but were associated with a particular geographic feature that was incorporated into the name. The post-Viking geologic map of the northern plains of Mars (Tanaka and others, 2005) dispensed with formation names for units but still incorporated geographic nomenclature in many unit names. Thus, the new map presented here is closer to the approach used in the original, Mariner 9-based map that grouped 24 geomorphic units (lacking formal geographic names) into 5 terrain types.

Unit Names and Labels

Unit names and labels consist of the following components: (1) age, (2) unit group, and (3) subtype (optional). For the first time in a map of Mars, the age assignments are included in the unit names to the precision of epochs where possible. This approach is consistent with approaches used in most terrestrial geologic maps (*, Reed and others, 2005; Bouysee, 2009). Moreover, the approach elevates the prominence and statistical integrity of crater-density dating efforts applied to map units, which is one of the most significant advancements resulting from this map. The interpreted age of each geologic unit is

identified in the unit label, where capital letters show the stratigraphic period (N, Noachian; H, Hesperian, A, Amazonian) and epoch is denoted by the use of a preceding lower-case letter (e, Early; m, Middle; l, Late). Where units include more than one epoch within a period, the epochs are not discriminated in the unit names and labels—the Correlation of Map Units (CMU) specifies the interpreted epoch range. In a few cases, observed superposition relations noted in the Description of Map Units (DMU) can be more precisely defined than shown in the CMU, which does not portray temporal relations within epochs. In addition, for units spanning more than one Martian period, the youngest period is followed by the oldest in the unit label and name (for example, HN, Hesperian and Noachian). The unit group designation follows the age component in both unit labels and names (a, apron; b, basin; h, highlands; i, impact; l, lowlands; p, polar; t, transition; v, volcanic).

In some instances, we needed to discriminate particular unit subtypes. Hence, the first letter of a modifying word follows unit group names and labels (c, cap; d, dune; e, edifice; f, field; m, massif; o, outflow; u, undivided). The term, “cap”, represents high-albedo, residual ice sheets that cover parts of the polar plateaus. Dune refers to typical yet diverse (barchan, linear, star, chained, and other complex shapes and patterns) eolian bedforms. Edifice represents topographic features consistent with volcanic construction. Field represents groups of relatively small (less than a few tens of kilometers across) volcanic vents and their contiguous lava plains. Massif represents especially rugged, high-relief, heavily cratered materials that typically form the rims of large impact basins. Outflow represents deposits that occur within—and are genetically linked to—large-scale outflow channels. Undivided units refer to layered sequences that may be hundreds of meters to kilometers thick; layering provides a basis for potential stratigraphic divisions in larger-scale mapping, particularly where unconformities and (or) lithologic changes can be identified. For example, the Amazonian polar undivided unit (Apu) is divided into four sequential units at 1:2,000,000 scale (Tanaka and Fortezzo, 2012).

Contact Types

Contacts are shown as either certain (solid), approximate (dashed), or internal (solid with younger (y) and older (o) labels). Certain contacts are considered to be well defined by morphologic and (or) IR brightness/albedo boundaries at digital mapping scale (1:5,000,000). Approximate contacts are imprecise due to weakly evidenced, obscured, gradational, and (or) complex unit boundaries. We identified internal contacts within Late Hesperian and Late Amazonian volcanic units (IHv and IAv, respectively), where one flow field overlaps and postdates another, and within some occurrences of unit AHv, where the ejecta of one crater overlaps that of another. In places, high-resolution images were used to augment global MOLA and THEMIS daytime IR base maps for contact mapping. For example, CTX images were locally used to verify and refine the contact between Amazonian and Hesperian transition undivided units (AHtu and Htu), based on recognition of relatively small landforms. Given the mapping

scale and smoothing applied to the drafted linework, extensive cartographic generalization occurs in which the detailed form of complex contacts evident at larger scale has been subdued or lost at the 1:20,000,000 map scale.

Line Feature Types

Our map includes line features categorized by major geologic types based on their typical morphologic forms (see Explanation of Map Symbols). The cartographic nature of this global product necessitates balanced spatial representation, rather than thorough identification of morphologic and tectonic features. Major feature types are classified according to preservation state (fresh, subdued, partly buried, or buried) and width (greater than or less than 10 km) in the digital map product (see map feature GIS attribute table for width designations).

Wrinkle ridges generally indicate tectonic contraction resulting from deep-seated (several kilometers or more) thrust faulting (*, Golombek and others, 2001). Broad grabens (>10 km wide) indicate deep-seated rifting (*, Hauber and others, 2010), whereas narrow grabens are indicative of either hour-glass-configured normal faults (*, Schultz and others, 2007) or shallow detachment along horizontal mechanical interfaces that may be underlain by dikes or hydrofractures (*, Tanaka and others, 1991; Grosfils and Head, 1994). Outflow channels likely formed as the result of catastrophically erupted, pressurized groundwater (*, Baker and others, 1992), whereas narrow valleys likely formed through outburst floods and (or) precipitation-driven surface runoff (*, Howard and others, 2005). (See Hynek and others, 2010, for more detailed mapping of valleys.) In some cases, mass flows, glaciers, and lava flows may also be responsible for channel formation, and rilles form a specific channel type that generally narrows downslope and is attributed mainly to thermal erosion (*, Nummedal and Prior, 1981; Lucchitta, 1982; Leverington, 2011). Ridges and scarps, where diagnostic morphologic associations are absent, may result from a variety and combination of geologic processes, including tectonic and impact deformation; fluvial, glacial, and mass-wasting erosion; and volcanism (*, Anderson and Anderson, 2010). Spiral troughs are particular erosional features related to erosion and transport of the polar plateaus by insolation and katabatic winds (*, Howard, 1978, 2000; Smith and Holt, 2010). Flow directions are mapped to show major trends of volcanic flows. Crater rims >100 km in diameter are drawn where regionally prominent, but possible buried craters (including quasi-circular depressions of Frey, 2006) suggested by tectonic features and shallow circular depressions are excluded. Some impact craters include circular, partial to complete peak rings within them, which are mapped as ridges (Lyot, Lowell, and Schiaparelli). Locally, pit crater chains occur where subsurface excavation led to collapse, likely related to dilational faulting and fissuring and possibly enhanced locally by groundwater flow (*, Wyrick and others, 2004). Rims of volcanic calderas >100 km across indicate sites of large-scale magma-chamber collapse, associated with effusive flank eruptions and central explosive eruptions, and are identified on the largest volcanic edifices of Mars (*, Crumpler and others, 1996; Williams and others, 2009).

Drafting

We used the Environmental Systems Research Institute, Inc. (Redlands, CA) ArcGIS software package to co-register and analyze available datasets. Simple Cylindrical versions of MOLA and THEMIS IR mapping bases were created in lossless GeoJPEG2000 format. For consistency and legibility at map scale, we defined drafting parameters within our digital GIS environment. First, the vertex spacing of drafted linework was set at 5 km (4 vertices per millimeter at 1:20,000,000 scale), which provides sufficient detail and curve rounding when a smoothing algorithm is applied to the linework. We drafted linework while viewing the map base data at 1:5,000,000 scale to ensure sufficient accuracy at print scale. The minimum line-feature length is 100 km, and the minimum outcrop dimensions are 40 km wide by 100 km long for legibility. Given differences between drafting and production scales, we avoided mapping narrow outcrops using parameters consistent with our minimum width specifications. Minimum spacing between linework, including both contacts and other line features, is 40 km. However, we exercised some flexibility in the size and spacing cutoffs to represent critical geologic and stratigraphic relations, including some narrow wall rock outcrops of Valles Marineris. Also, we generalized some segmented, en echelon grabens that were too short to map as single segments by mapping them as single collective features to show the occurrence of particular structural fabrics.

Line symbols were adapted from standard drafting conventions (Federal Geographic Data Committee, 2006). In general, units within groups were assigned to color families (yellow for the impact unit; greens for lowland units; blues for polar units; bluish greens for basin units; reds, oranges, and purples for volcanic units; and browns, oranges, and gray tones for apron, transition, and highland units). This approach is similar to that used in previous Martian global map-unit color schemes (Scott and Carr, 1978; Scott and Tanaka, 1986).

Age Determinations

The relative age of each map unit was determined using the scheme of three chronostratigraphic periods and eight epoch divisions of the periods that are based on the crater densities of key referent surfaces (table 1; Tanaka, 1986; Werner and Tanaka, 2011). Detailed crater size-frequencies were obtained for representative counting localities for 23 of the 44 map units (table 2 and fig. 1) primarily from HRSC (High Resolution Stereo Camera, onboard the Mars Express spacecraft) data at 12.5 m/pixel and secondarily CTX data at 5 to 6 m/pixel using the GIS extension CraterTools (Kneissl and others, 2011) and the Craterstats software (Michael and Neukum, 2010). Selection of representative counting localities was required, because (1) the total areas and numbers of craters of specific units were too large for complete counts, (2) many of the units exhibited diverse or modified morphologies and other characteristics that made dating areas displaying the most typical morphologies the most desired, (3) parts of unit surfaces have been modified

by erosion, tectonism, deposition followed by exhumation, and other resurfacing processes that would also result in atypical crater populations (and thus avoided), and (4) some areas had inadequate, high-resolution (HRSC and CTX) image coverage (for a more thorough treatment, see Platz and others, 2013). In some cases, pertinent crater counts that adequately date the units have been published and are cited where the units are described in the Geologic History section for comparison with (or in lieu of) crater counts in this map (tables 2, 3, and D1). For some units having great durations as established by stratigraphic relations, high degrees of post-emplacment crater obliteration, and (or) wide variations in crater densities, detailed crater counts are not helpful in constraining their ages and thus were not obtained.

Model ages derived from the Hartmann and Neukum (2001) chronology function are based on the Ivanov (2001) crater production function. Parts of the crater size-frequency distributions that fit well to the production function over continuous ranges of diameter were used to determine model ages. The Craterstats software performs adjustments that allow for the fitting of multiple resurfacing ages at progressively smaller diameter craters. Thus, many counts resulted in two or more age populations (table 2). Each crater count was tested for spatial randomness to avoid surfaces where crater populations may have been affected by secondary craters or by inhomogeneous resurfacing (Michael and others, 2012).

Because of their widespread occurrence and role in establishing global stratigraphy, we focused much of our attention on the stratigraphic differentiation of Noachian highland unit outcrops, wherein our mapping identified three morphologic-chronostratigraphic categories: (1) Early Noachian—highest relief and highest density of impact craters, (2) Middle Noachian—moderate relief and intermediate density of impact craters, and (3) Late Noachian—low local relief and relatively low density of impact craters. Although contacts between these units generally are not sharply defined, most follow topographic breaks where surface landforms become embayed, buried, and (or) markedly subdued. Where counts of all impact craters (including buried and otherwise modified craters) yielded multiple surface ages, the nature of the unit being dated was specifically assessed to determine the most appropriate age. For example, model age determinations for Early Noachian units were applied to the oldest crater-retention ages, whereas model ages of some younger units were applied to a younger resurfacing age in the crater distribution. This assumption was verified by examining the appearance of the actual craters being counted. In most instances, we confirmed that buried crater populations pre-date the unit. Moreover, we were able to verify that the ages that we had suspected for these and other stratigraphically significant units were generally correct in the representative areas, which verified our stratigraphy. Once we verified that the epoch and period crater-density boundaries of Tanaka (1986) and Werner and Tanaka (2011) were still valid when applied to this new map, we then could use crater counts to verify or reassign the unit designations for otherwise equivocal outcrops.

Given the above analysis, we now define the Early, Middle, and Late Noachian highland units as new referents

for their respective epochs, thus revising those ages based on the previous Viking-based maps of Mars (Tanaka, 1986). We have similarly defined new referent units for the Hesperian and Amazonian epochs (table 1), which for the Hesperian have heritage to previously used referents (Tanaka, 1986). The Early Hesperian Epoch is defined by the Early Hesperian volcanic unit (eHv), which includes materials of volcanic plains in Hesperia Planum on which the Hesperian Period definition was founded (Scott and Carr, 1978). The unit also includes broad volcanic flow fields spread around the Tharsis region, as well as making up Syrtis Major Planum. The Late Hesperian lowland unit (lHl) defines its epoch, following the precedent of Tanaka (1986). A new Early Amazonian referent is the areally small Early Amazonian basin unit (eAb)—the only map unit confined to this epoch in spite of the epoch's apparent approximately 2-b.y. duration (table 1). Similarly, only the Middle Amazonian lowland unit (mAl) occurs solely within its epoch. Finally, a new referent for the Late Amazonian is the Amazonian polar undivided unit (Apu), which forms ice-rich layered plateaus at both poles (commonly referred to as “polar layered deposits”). Although the base of this unit is poorly defined, it significantly contains a record of recent climate variation on Mars.

Our approach to crater counting was limited to representative locations ranging in size from $4 \times 10^3 \text{ km}^2$ to $90 \times 10^3 \text{ km}^2$, where all observed craters were counted down to minimum diameters of between 100 to 400 m depending on the area size and surface age (presented in detail by Platz and others, 2013; see also table 2 and fig. 1 showing areas counted). For most of these locations, we determined two model ages (in other cases, one or three). The older age based on the largest craters present was often assigned as unit formation age to ancient highland and thick volcanic units. The reported resurfacing age is also provided to highlight that surfaces experienced post-formation modification through erosion, deposition, deformation, or impact cratering. For younger units that do not completely bury older surfaces, the resurfacing age has been used to infer unit formation ages (for example, at locality 34 in table 2 and fig. 1, the mapped Late Noachian highland unit, lNh, buries an Early Noachian surface). The older ages reported in those cases correspond to the ages of underlying units that were partly buried by the young surface of interest. Although craters were counted to minimum diameters between 100 and 400 m, the minimum diameter used to fit the isochrons was generally $\geq 400 \text{ m}$ (in four instances the minimum diameter was between 200 and 350 m).

We also excluded visible clusters, chains, and strewn fields of secondary impact craters from the counting area. Each measured crater size-frequency distribution was also tested for spatial randomness using the procedure of Michael and others (2012) and discarding any that were not sufficiently random (see also Platz and others, 2013).

Remaining outcrops were too large (some exceeding $100 \times 10^3 \text{ km}^2$), too numerous, or otherwise problematic for counting craters approximately $<1 \text{ km}$ in diameter, and they required a simplified although less precise crater-dating approach. For these, we applied the global impact crater database that consists of all craters with diameters $>1 \text{ km}$ (Robbins and Hynek, 2012).

This database was imported into our GIS project, enabling automatic generation of cumulative crater densities for the entire unit areas (including as needed assimilation of superposed unit AHi outcrops), as well as individual occurrences that could be compared with the assigned and calculated boundary densities for craters >1 km (N1), >5 km (N5), and >16 km (N16) in diameter that define epoch boundaries (table 3). This approach required merging the Amazonian and Hesperian impact unit (AHi) into subjacent units, which allowed proper inclusion of the impact craters that define unit AHi. This exercise was performed for all units where unit AHi occurrences were superposed.

Our representative counts of the Middle Noachian highland unit (table 2 and fig. 1; see also Platz and others, 2013) indicate that craters >10 km in diameter have been preserved, validating our application of N(16) values to discriminate most surfaces for their relative age to the upper and lower boundaries of the Middle Noachian. For the Late Noachian/Early Hesperian and Early Hesperian/Late Hesperian boundaries, N(5) was more accurate based on the statistical preservation of craters larger than this diameter. Though most Amazonian surfaces display craters preserved down to 1 km diameter, some potentially Early Amazonian surfaces of unit AHtu are missing craters as large as 5 to 6 km in diameter due to mass wasting and erosion. Most outcrops in our initial mapping had an N(1), N(5), or N(16) value that corresponded with the age of the unit to which they were assigned. Where the crater density was in clear disagreement with the initial age assignment, the outcrop was re-assigned to a morphologically similar unit whose age was in agreement with the outcrop (for example, switching a unit designation from eNh to mNh or eHv to INv based on crater density). This procedure commonly resulted in the merging of adjacent outcrops that had the same unit designation. Some outcrops do not contain crater populations that yield statistically meaningful crater densities. In these instances, direct crater-density dating is not well constrained, although crosscutting and overlap relations with adjacent units helped to establish meaningful stratigraphic assignments.

Crater populations for many Late Noachian and younger surfaces include topographically subdued, often rimless craters that likely belong to buried surfaces. Thus, we did not include such craters when deriving crater densities from the global crater data base in order to obtain accurate ages. We recognize, though, that the unit surface age provides only a minimum age constraint, whereas older age constraints come from the ages of surfaces buried or embayed by the unit. In some cases, such as for the Late Hesperian lowland unit (IHl) and the Amazonian and Hesperian volcanic edifice units (Ave and Hve, respectively), the oldest parts of the units are buried, which means that the age of initiation of unit emplacement is unconstrained. To show this lack of constraint, the lower edges of the unit boxes have sawtooth-edged age boundaries in the CMU. In addition, some transition units have two major, inseparable components of different age—combinations of Noachian highland material and Hesperian or Amazonian plains or apron material. The age ranges for these units span the development of both components.

When dating impact craters and basins >150 km in diameter, our results are generally consistent with those of Robbins and others (2013), who dated 76 of the 102 features that they identified in this size range. We have dated nearly all of the features using stratigraphic and geomorphic observations (table 4), crater densities (tables 2 and 4), and other work (noted in table 4). The identification, measurement, and dating of 28 craters are considered to be moderately to highly uncertain (these are marked with an asterisk in table 4), and one crater is now considered to be in error (S.J. Robbins, written commun., 2013). Some discrepancies result, particularly for features that we assigned Late Noachian and younger ages, given how the crater extents were mapped and (in our approach) the number of craters identified within and superposed upon the crater ejecta. In addition, Robbins and others (2013) determined ages based on diameters >10 km to fit to absolute-age schemes, whereas we used craters >5 and >16 km in diameter to determine epoch ages. For example, the mapped extent for Galle crater includes the continuous ejecta, whereas Robbins and others (2013) dated only the rim of Galle. We find 7 to 9 superposed craters >5 km diameter (the relative positions of two craters are equivocal), yielding an N(5) density of 43 ± 16 to 55 ± 18 that corresponds most likely to the Early Amazonian (Werner and Tanaka, 2011). The method of Robbins and others (2013) yielded a median age within the Late Noachian. The ejecta of Galle overlie the Hesperian and Noachian basin unit covering Argyre Planitia, which has a distinctly higher density of craters ($N(5) = 209 \pm 25$, indicating a Late Noachian or Early Hesperian age).

Many outcrops, particularly of Middle and Late Amazonian units, could not be accurately dated using craters larger than 1 km. However, in some cases, published crater counts of smaller craters for these units exist and were utilized for our age designations (*, Vaucher and others, 2009; Hauber and others, 2011; Skinner and others, 2012). Other outcrops and units have been eroded, mantled, or otherwise obscured to the point that crater densities are not indicative of unit age. Post-Noachian impact craters are generally identified and mapped based on the relatively pristine morphologic expression of their rim and ejecta but are too numerous to date individually. As such, they are grouped into a single Amazonian and Hesperian impact unit (AHi). The vast lava-flow fields comprising most of the central extents of the Tharsis and Elysium rises show ranges of ages and pathways of individual flows and local flow fields, commonly with no distinct separations of mappable areas of flows of different epochs. In such cases, we map the flows conservatively as the Amazonian and Hesperian volcanic unit (AHv), although previous mapping distinguished multiple flow units based on their mean crater densities (Scott and Tanaka, 1986).

In summary, assignment of relative ages to the map units has been performed to the precision of the eight time-stratigraphic epochs of Mars (Tanaka, 1986; table 1), as shown in the Correlation of Map Units. These assignments are based on (1) stratigraphic relations revealed by the map, as well as (2) crater size-frequency data provided herein and from other sources (table 5). Thus, the robustness of each age assignment varies according to the quality, quantity, and applicability of mapping results coupled with crater statistical data.

Geologic History

This global map builds upon previous mapping results and provides new findings and synthesizes other research regarding the geology of Mars, based largely on spacecraft data obtained since the late 1990s. The geologic map includes detailed stratigraphic relations and crater-density statistics that allow for the reconstruction of regional to global geologic events that shaped the surface of Mars. We provide interpretations of the processes that resulted in the present-day landscape of Mars, given our mapping-based analysis as well as other published work. Processes that have effectively modified geological units through temporally extended or punctuated resurfacing have resulted in a geologic and stratigraphic record that is both complex and only partly accessible through mapping.

Noachian Period

The Noachian Period includes the oldest observed geologic activities and resultant units on the surface of Mars, effectively recording rapidly declining impact bombardment from the Early to Late Noachian Epochs (*, Tanaka, 1986; Hartmann and Neukum, 2001). As a consequence of impact cratering and concurrent degradation processes, primary morphologies tens to hundreds of meters in relief and smaller, including tectonic, volcanic, erosional, sedimentary, and impact landforms, were effectively destroyed—especially those that formed during the Early and Middle Noachian Epochs. An exception is strata exposed in eroded Noachian sequences, including areas of the highlands that contain dense arrays of channels, as well as the walls of Valles Marineris (unit *Nhu*). Valley systems (*, Craddock and Howard, 2002; Fassett and Head, 2008a; Hynes and others, 2010) are locally associated with basin-filling deposits (*, Fassett and Head, 2008b) and suggest the occurrence of distributed, unmapped, thin outcrops of fluvial sediments included in Noachian units. In addition, Noachian highland volcanic edifices (*, Hodges and Moore, 1994; Xiao and others, 2012) suggest that highland materials include variable amounts of volcanic rocks. Noachian units also contain post-Noachian crater ejecta, which generally is included in the units except where we delineated outcrops >100 km across of the Amazonian and Hesperian impact unit (*AHi*). Larger volcanoes mapped as the Noachian volcanic edifice unit (*Nve*) display crater ages indicative of multiple stages of activity (Werner, 2009).

The Noachian geologic record in the lowlands is largely unknown, except for a few degraded and fractured Noachian outcrops east of the Elysium rise and at Acidalia Mensa (mapped as the Hesperian and Noachian transition unit, *HNT*), the arcuate Acheron Fossae structure north of Olympus Mons (mapped as the Late Noachian highland unit, *INh*), and unmapped, buried, and degraded crater forms that pre-date the Hesperian plains-forming materials (Frey and others, 2002). The highland-lowland transition zone has been modified due to erosion by liquid water, water-ice, wind, and gravity-driven processes (*, McGill, 2002, 2005;

Tanaka and others, 2005; Dickson and others, 2008; Chuang and Crown, 2009; Fairén and others, 2011; Davila and others, 2013), as well as by endogenic-driven deformation (*, Phillips and others, 2001).

The Noachian is also characterized by the highest mean global erosion rates (Golombek and others, 2006) and formation of extensive valley networks possibly peaking in intensity near the end of the period (*, Howard and others, 2005; Irwin and others, 2005; Fassett and Head, 2008a,b; Hoke and Hynes, 2009; Hynes and others, 2010). Large impact and perhaps tectonic landforms that pre-date the Noachian appear to be preserved in the highlands and lowlands (*, Schultz and others, 1982; Nimmo and Tanaka, 2005; Andrews-Hanna and others, 2008), despite later burial and modification (*, Hiesinger and Head, 2000; Frey and others, 2002; Tanaka and others, 2005). Large extensional and contractional tectonic structures, hundreds to thousands of kilometers long, including Phlegra Montes, Tanais Fossae, older structures of Claritas Fossae, and scarp- and ridge-bounded basins in Terra Cimmeria and Terra Sirenum, point to a changing landscape during the Early and Middle Noachian Epochs, prior to the major rise of the Tharsis region (*, Baker and others, 2007).

Noachian geological units typically have a spectral signature that indicates a high abundance of basaltic compositions, including iron- and low-calcium-bearing pyroxenes and olivine, reported to mark modest crustal differentiation (*, Bibring and others, 2005, 2006). Early and Middle Noachian rocks also contain phyllosilicates and chlorite, which are interpreted to have formed through aqueous alteration (*, Poulet and others, 2005; Murchie and others, 2009; Ehlmann and others, 2011; Ody and others, 2012). Chloride salts within Middle Noachian to Early Hesperian highland units occur in some valleys and basins and are thought to be produced by evaporation of briny water that carved valley networks (*, Murchie and others, 2009; Osterloo and others, 2010). Change to a more acidic environment fueled by extensive volcanism and volatile release, such as related to incipient Tharsis rise development (*, Dohm and others, 2001b; Phillips and others, 2001), may explain the reduced signature of phyllosilicates beginning in the Middle to Late Noachian in highland and transition units, after which sulfate-rich layered deposits in Meridiani Planum (unit *HNhu*) formed (*, Bibring and others, 2006; Ehlmann and others, 2011).

The Martian highlands display zones of intense crustal magnetization in Terra Cimmeria and Terra Sirenum. The magnetization patterns may correspond to some exposed Noachian rock outcrops and structures, possibly indicating dynamic crustal evolution prior to Tharsis rise development (Dohm and others, 2013). Also, magnetization is weak in the vicinity of large impact basins, the northern plains, and volcanic regions, indicating that thermal events erased the possibly more widespread magnetization of early crustal rocks (*, Acuña and others, 2001; Connerney and others, 2001; Langlais and others, 2004). Thus, the Martian magnetic field apparently disappeared prior to the majority of the Early Noachian geomorphic and geologic record, including Hellas basin (*, Nimmo and Tanaka, 2005; Frey, 2006).

Early Noachian Epoch

The oldest crust on Mars consists of Early Noachian materials and inferred, buried pre-Noachian materials associated with topographically subtle basins that may be vestiges of impacts. These materials largely postdate formation of the broad northern lowlands, which comprise the earliest recognized geographic feature of the planet and are likely either of impact or tectonic origin (*, Nimmo and Tanaka, 2005; Frey, 2006; Andrews-Hanna, 2008). Our dating of the largest impacts in the global crater database of Robbins and Hynek (2012) indicates that the Early Noachian Epoch included formation of at least 65 impact basins that are >150 km in diameter (table 4; see also Werner, 2008; Robbins and others, 2013). Eighteen of these basins are deeply buried or highly degraded and their identification, diameter, and age have greater uncertainty when compared to other basins. The largest basin is defined by Hellas Planitia (~2,400 km in diameter) and includes the lowest surface elevation on Mars. The Hellas basin, as an impact feature, includes an asymmetric (~5,000 km in diameter northeast-southwest and ~6,000 km in diameter northwest-southeast) annulus of terrain elevated between 1 and 2 km above the surrounding highlands, comprising a volume similar to that missing from within the basin (Smith and others, 1999). The interior and southeastern parts of the annulus are made up of massifs and intervening troughs and plains of the Early Noachian highland massif unit, *eNhm*, whereas remaining high-standing, rugged areas are the Early Noachian highland unit, *eNh*. The western and northwestern parts of the rim and annulus of Hellas basin are deformed by concentric and oblique ridges (Hellas Montes) and troughs (for example, Scylla Scopulus), which may have been the result of a low-angle impact directed southeast (Tanaka and Leonard, 1995). The ~1,160-km-diameter south polar basin is partly outlined by the Promethei Rupes scarp, which forms the extant basin rim and is largely buried by Planum Australe.

Outcrops of unit *eNh* in the remainder of the highlands are common east of Hellas basin in Terra Cimmeria and Terra Sirenum, corresponding to the zone of strong crustal magnetization, but are sparse around Argyre basin and in most highlands north of the equator in Arabia, Margaritifer, and Xanthe Terrae and northern Terra Sabaea. Some outcrops of unit *eNh* in the southern parts of the Tharsis rise contain dense arrays of linear to sinuous troughs interpreted to be narrow grabens and wide rifts, indicating crustal extension (*, Dohm and others, 2001a; Hauber and others, 2010). Other ridges made up of unit *eNh* trending concentric to the margin of Daedalia Planum may have resulted from crustal contraction due to Syria Planum-centered uplift (*, Banerdt and others, 1992; Schultz and Tanaka, 1994). About two-thirds of mapped Noachian highland edifices (unit *Nhe*) and volcanic edifices (unit *Nve*) may be Early Noachian, which attests to early, widespread volcanism with a concentration south of the Tharsis region (Scott and Tanaka, 1981a; Xiao and others, 2012). Small valleys dissect Early Noachian units in places, and some fluvial dissection and mass wasting likely subdued prominent landforms during this epoch. Overall, Early

Noachian materials consist mostly of impact breccias and melts, igneous rocks, and some sedimentary sequences.

Middle Noachian Epoch

The Middle Noachian highland unit (*mNh*) dominates highland regions wherever the Early Noachian highland unit (*eNh*) is sparse or absent, including regions that border the highland/lowland transition zone in Arabia Terra and south of Elysium Planitia, as well as those that surround Argyre basin. Unit *mNh* also forms relatively low lying surfaces adjacent to higher-standing outcrops of unit *eNh*; commonly a slope break separates these units, wherein narrow (unmapped) valleys incise the steeper parts of the *eNh* unit. Unit *mNh* likely consists of a higher proportion of sedimentary and volcanic materials relative to unit *eNh*, which may reflect climate conditions conducive to precipitation and runoff (Irwin and others, 2013).

The highlands contain at least 15 Middle Noachian impact basins that are >150 km in diameter (table 4). Argyre and Isidis basins are regionally defined by topographic depressions surrounded by the Middle Noachian highland massif unit (*mNhm*). For Argyre basin, the massif unit has a mean outer diameter of ~1,500 km and is surrounded by the Middle Noachian highland unit to a diameter of ~3,000 km. Unlike Hellas basin, this outer zone does not form a distinctly elevated annulus but includes broad, irregular troughs and ridges that are oriented mostly circumferential to the basin and that likely represent structural rings associated with basin formation.

The Isidis basin is located along the highland/lowland transition and displays morphologic characteristics that are different than the similarly sized Hellas and Argyre basins. For example, Isidis basin has a discontinuous rim of the Middle Noachian highland massif unit (*mNhm*), which extends for a diameter of ~2,100 km and is interspersed with less rugged, lower-relief Middle Noachian highland unit (*mNh*) and post-Noachian units. Circumferential, mostly narrow troughs encircle the northwest (Nili Fossae) and southeast (Amenthes Fossae) parts of the Isidis basin rim. The troughs likely formed through crustal extension during the Middle Noachian and were reactivated into the Hesperian, given that they locally cut the Early Hesperian transition unit (*eHt*). Oenotria Scopuli are basin-facing, circumferential scarps that displace and modify the Early Noachian highland unit (*eNh*) at a radial distance of 1,400 to 1,500 km from the center of Isidis that appear to form a basin-ring structure. Carbonate, rare on the surface of Mars, occurs in a consistent stratigraphic horizon, in places surrounding Isidis basin, and reflects neutral to alkaline conditions at the time of formation, likely by alteration of an olivine-rich layer (*, Ehlmann and others, 2008); also, diverse assemblages of altered silicate minerals indicative of low-grade metamorphic or hydrothermal aqueous alteration occur in Noachian terrain west of Isidis basin (*, Ehlmann and others, 2009).

Noachian highland and volcanic edifices (units *Nhe* and *Nve*, respectively) are fewer in the Middle Noachian than in the Early Noachian, perhaps due to increased global compressional stress and crustal thickening, which restricted the ascent of magma away from regional magmatic centers such as Tharsis

and Elysium (*, Xiao and others, 2012). Embayment by unit INh shows that the Thaumasia highlands uplifted mostly during the Middle Noachian, and the development of densely spaced, narrow grabens and rifts across the Thaumasia highlands at this time indicates their contemporaneity with the uplift (Dohm and others, 2001a; Hauber and others, 2010).

Late Noachian Epoch

Modification of the Martian cratered highlands continued in the Late Noachian by volcanic, sedimentary, and impact processes, although at overall reduced rates and extents (*, Golombek and others, 2006; Tanaka and others, 2014). These processes resulted in the accumulation of deposits in both inter- and intra-crater basins, mapped herein as the Late Noachian highland unit (INh). Unit INh includes ejecta associated with three impact craters that are >150 km across: Becquerel and Green craters and Orcus Patera (table 4). Unit INh occurs mostly near unit eNh outcrops, as well as along the eastern margins of Thaumasia Planum and Tempe Terra. They also occur locally in Middle Noachian-dominated Arabia Terra, northern Terra Sabaea, other areas along the highland/lowland transition zone, and the annulus of Argyre Planitia. These associations suggest that areas of higher relief experienced enhanced precipitation and erosion, resulting in sedimentation in adjacent topographic depressions (including impact craters) near the end of the Noachian Period (*, Howard and others, 2005; Irwin and others, 2005; Mest and Crown, 2006; Fassett and Head, 2008a,b; Grant and others, 2009; Hynek and others, 2010). In some cases, outflow channels such as Mawrth and Ma'adim Valles were carved by large water discharges resulting from overtopping of highland basins or breakouts from over-pressured aquifers (*, Carr, 1979; Irwin and others, 2004; Irwin and Grant, 2009).

Denudation is indicated along the margins of Thaumasia Planum and Tempe Terra by local terraces, which are interpreted to be eroded strata and mapped as unit Nhu. The deposition of the resulting detritus may have contributed to outcrops of unit INh. Within Argyre and Hellas Planitiae, basin floors are occupied by the Noachian and Hesperian basin unit (HNb), suggesting infilling by sedimentation and perhaps volcanism (*, Leonard and Tanaka, 2001; Moore and Wilhelms, 2001, 2007; Hiesinger and Head, 2002). Also, the northeastern margin of Hellas basin includes an outcrop of unit INh resulting from fluvial sedimentation and volcanism that has been dissected and modified by later fluvial activity and other processes (Bleamaster and Crown, 2010).

The layered Hesperian and Noachian highland undivided unit (HNhu) in Meridiani Planum has been directly (though locally) observed by the Opportunity Mars Exploration Rover (*, Squyres and others, 2006). Previous work indicates a Late Noachian to Hesperian age for this outcrop (Hynek and Phillips, 2008), and large craters within and buried by the unit indicate a Middle Noachian age for the underlying surface (that of unit mNh) (locality 24 in table 2). This deposit of unit HNhu is composed of sulfate-rich eolian and fluvial material covered by a hematite-rich erosional lag (*, Grotzinger and others, 2005)

and may result primarily from aeolian deposition followed by groundwater alteration (*, Andrews-Hanna and others, 2007), as well as by fluvial and marine processes (*, Dohm and others, 2009a).

The oldest recognizable volcanic flows and plains-forming deposits on Mars are mapped as the Late Noachian volcanic unit (unit INv), which occurs in the Tharsis region and Hellas basin. The most extensive outcrop of unit INv forms a furrowed deposit in Malea Planum that appears to be sourced from circular paterae displaying low rims and depressed centers (*, Leonard and Tanaka, 2001; Plescia, 2004; Williams and others, 2009). The two most distinctive paterae in this region, Amphitrites and Peneus Paterae, are mapped as the Noachian volcanic edifice unit (Nve). Tyrrhenus Mons, northeast of Hellas basin (also mapped as unit Nve), exhibits highly dissected flanks surrounding a central caldera complex and provides evidence for prolonged volcanic activity beginning with explosive volcanism emplacing pyroclastic flows in the Late Noachian (*, Greeley and Crown, 1990; Gregg and others, 1998). Apollinaris Mons (units Nve and Hve) occurs along the highland-lowland transition zone and reveals a long history of volcanic, hydrologic, and perhaps hydrothermal activity (*, El Maarry and others, 2012). Several irregularly shaped, unmapped depressions tens of kilometers across of Late Noachian to Early Hesperian age along the transition zone in northern Arabia Terra have been proposed to be volcanic calderas (Michalski and Bleacher, 2013). Outcrops of unit INv that contain lava-flow lobes occur in Thaumasia Planum, as well as in scattered plains south of Daedalia Planum. Some outcrops of unit INh north of Olympus Mons (deformed by Acheron Fossae), in southwestern Tempe Terra, and in parts of the Thaumasia highlands may be volcanic given their proximity to the Tharsis region, but swarms of grabens and other modificational features may have obscured potential volcanic morphologies.

Late Noachian crustal deformation is confirmed where tectonic structures transect Late Noachian surfaces that are partly buried by Early Hesperian outcrops. These include (1) dense swarms of narrow grabens of Claritas Fossae and in Icaria Planum radial to Syria Planum, likely in response to lithospheric flexure due to loading by the Tharsis rise (*, Banerdt and others, 1992; Tanaka and Davis, 1988; Anderson and others, 2001); (2) generally west-northwest-trending grabens of Acheron Fossae (Kronberg and others, 2007); and (3) grabens within and resulting from uplift of the Thaumasia highlands (*, Dohm and others, 2001a). Although Late Noachian surfaces are commonly deformed by wrinkle ridges, the cumulative amount of deformation is comparable to that on Early Hesperian surfaces, suggesting that contractional deformation was minor in the Late Noachian. The Valles Marineris troughs began to form during this epoch by rifting, as indicated by crosscutting and stratigraphic relations among rock materials and tectonic structures, particularly along the western margin of Thaumasia Planum (Witbeck and others, 1991; Dohm and others, 2001a, 2009b). Most of these structures relate to development of the Tharsis rise, indicating that this immense feature had become the dominant magmatic and tectonic locus for the planet by the

end of the Noachian (*, Tanaka and others, 1991; Anderson and others, 2001).

Hesperian Period

The Hesperian represents an intermediate period of Mars' evolutionary chronology that generally preserves much more diverse processes than the Noachian, due to less cumulative impact gardening and reduced mean erosion rates (*, Hartmann and Neukum, 2001; Golombek and others, 2006). Hesperian activity was dominated by extensive volcanism, tectonism, chaos and outflow channel development; northern plains and polar accumulations; and mass wasting and deposition along the highland/lowland transition zone. Generally, resurfacing of the Martian cratered highlands was more localized during the Hesperian Period, which included at least four large impacts 150 to 200 km in diameter (Gale, Holden, Lowell, and Bakhuisen). Acidic weathering conditions during the Hesperian led to sulfate enrichment of layered deposits in Valles Marineris and Gale crater (Hesperian transition undivided unit, Htu) and in Schiaparelli, Terby, and other highland craters (Hesperian and Noachian highland undivided unit, HNhu) (*, Bibring and others, 2006). Tharsis-related volcanism and catastrophic outflow flooding were major contributors to resurfacing during the Hesperian Period at local to possibly global scales (*, Hynek and others, 2003; Baker and others, 2007; Dohm and others, 2009a). The overall amount of formation of precipitation-fed runoff valleys and sedimentary deposits was reduced relative to that of the Noachian, leading to just a few local highland examples (*, Grant and Schultz, 1990; Mest and Crown, 2002, 2003; Mangold and others, 2008). Nine occurrences of the Hesperian volcanic edifice unit (Hve) are mapped in the Tharsis, Elysium, and northeast Hellas basin regions, and the southern fan deposit of Apollinaris Mons also is mapped as unit Hve (the remainder of the volcano is made up of unit Nve). Although construction of Martian volcanic edifices appears to be dominated by effusive volcanism, evidence for pyroclastic volcanism is apparent at Apollinaris Mons and Hadriacus Mons and in the Elysium region (*, Tanaka and others, 1992; Crown and Greeley, 1993, 2007; El Maarry and others, 2012).

Some of the most pronounced erosion of geologic terrains on Mars took place during the Hesperian. Along the highland/lowland transition zone, complex arrays of remnant Noachian highland-material inliers are surrounded by Hesperian plains-forming mass-wasting deposits (*, Tanaka and others, 2005), including the Hesperian and Noachian transition unit (HNt). Troughs of Valles Marineris and depressions east and northeast of Valles Marineris were the sites of extensive collapse and flood discharges that resulted in (1) the modification of Noachian highland units to form "chaotic terrain" (Sharp, 1973), mapped herein as the Hesperian transition unit (Ht), and (2) the carving of and sedimentation within outflow channels (forming the Hesperian transition outflow unit, Hto) (*, Rotto and Tanaka, 1995; Tanaka, 1997; Chapman and others, 2010). The eastern rim of Hellas basin presents another area of outflow channel erosion (Crown and others, 1992, 2005; Tanaka and Leonard, 1995). In the highland/lowland transition zone south

of the Elysium rise, layered, wind-carved deposits (units Htu and AHtu) may be pyroclastic or other eolian fines (identified as the Medusae Fossae Formation; Scott and Tanaka, 1982, 1986; Hynek and others, 2003; Mandt and others, 2008), perhaps sourced locally (Scott and Tanaka, 1982) from Tharsis volcanoes (Hynek and others, 2003) or from Apollinaris Mons (Kerber and others, 2011). Locally, unit Htu includes possible aqueous deposits (DiBiase and others, 2013). Watters and others (2007) noted that units Htu and AHtu generally have a low radar dielectric constant, consistent with either highly porous sediment or ice-rich material covered with thin lags. Consistent with our age assignments, Kerber and Head (2010) and Zimbelman and Scheidt (2012) both found that a large proportion of these units (although they mapped them differently) were originally formed in the Hesperian.

The oldest mapped outcrops of ice-rich polar deposits span the Hesperian Period. The plains-forming Hesperian polar unit (Hp) and edifice-forming Hesperian polar edifice unit (Hpe) surround Planum Australe and may have been emplaced through cryovolcanic eruption (Tanaka and Kolb, 2001) and (or) from accumulation of a glacial ice sheet (Head and Pratt, 2001). Unit Hp is marked by narrow sinuous ridges that represent either inverted fluvial channels or eskers (*, Head and Pratt, 2001; Tanaka and Kolb, 2001; Ghatan and Head, 2004). Additional polar mounds and depressions of unit Hpe form Scandia Tholi and Scandia Cavi near Planum Boreum and may result from mud volcanism and diapirism (Tanaka and others, 2003, 2011; Skinner and Mazzini, 2009). The basal materials of Planum Boreum comprise a thickly layered mixture of ice and dust (Phillips and others, 2008; Putzig and others, 2009; Tanaka and Fortezzo, 2012) mapped as the Hesperian polar undivided unit (Hpu).

Early Hesperian Epoch

The Early Hesperian volcanic unit (eHv) identifies areally extensive lava fields that partly bury the margins and high-standing internal surfaces of the Tharsis rise, as well as Hesperia and Syrtis Major Plana (*, Hiesinger and Head, 2004). The Spirit Mars Exploration Rover demonstrated that the Gusev crater floor is covered by lavas that date to this time (*, Squyres and others, 2004; Greeley and others, 2005). The Early Hesperian highland unit (eHh) is likely made up of a variety of plains-forming rocks and sediments of uncertain origin. Components may include volcanic rocks proximal to major volcanic centers and perhaps interbedded eolian and lacustrine sediments throughout inter-crater highland basins, some that show dissection, including inlet and outlet valleys (*, Grant and Schultz, 1990; Cabrol and Grin, 1999; Goudge and others, 2012). Four unit HNt outcrops close to one another in Terra Sirenum and Terra Cimmeria include dense clusters of degraded mesas and knobs. Plains with scattered knobs mapped as the Early Hesperian transition unit (eHt) occur along the highland/lowland boundary and east of Elysium rise, apparently resulting from mass-wasting and other resurfacing processes (*, Tanaka and others, 2003). Some of the knobs may be juvenile volcanic or mud vents (Skinner and Tanaka, 2007), although the presence

of buried crater and trough forms in the unit suggests it is dominated by unconsolidated sediments rather than by volcanic rock. In eastern Hellas Planitia, the Early Hesperian basin unit (eHb) may have been emplaced and modified by eolian, lacustrine, and (or) volcanic processes (*, Tanaka and Leonard, 1995; Moore and Wilhelms, 2001, 2007; Crown and others, 2005; Bleamaster and Crown, 2010).

Tectonism during the Early Hesperian was dominated over most of Mars by widespread crustal contraction, perhaps related to planetary cooling, which formed arrays of moderate- to high-relief wrinkle ridges in most unit outcrops of this age (units eHh, eHv, eHt, and eHb) (*, Tanaka and others, 1991; Watters, 1993). Wrinkle ridges vary in orientation and commonly follow buried circular impact structures (*, Watters, 1993). The chasmata of Valles Marineris continued to form during the Early Hesperian (Witbeck and others, 1991) as a result of at least limited crustal extension, perhaps along steeply dipping faults (Andrews-Hanna, 2012). Crustal extension, related to increased regional magmatism, resulted in the formation of graben arrays in volcanic rocks (unit eHv) within and marginal to the Tharsis rise (*, Anderson and others, 2001). Some Early Hesperian rocks are dissected by fluvial channels, including those in southwestern Hesperia Planum, suggesting persistent, volcanically driven groundwater discharge toward Hellas Planitia in the Hesperian (*, Squyres and others, 1987; Crown and others, 1992, 2005; Tanaka and Leonard, 1995; Price, 1998).

Late Hesperian Epoch

The Late Hesperian volcanic unit (IHv) covers several areas of the Tharsis region and a small area that extends southwest from Tyrrhenus Mons (Greeley and Crown, 1990); Syria and Solis Plana and Noctis Fossae are the most areally extensive. Unit IHv appears to be dominated by lava flows, and two internal contacts demarcate sub-regions of contrasting relative ages, as determined by overlap relations and flow trends. The Late Hesperian volcanic field unit (IHvf) includes many small shields and fissure vents around Syria Planum. Unit IHvf also occurs in central and northeastern parts of the Tharsis region and on the western flank of Elysium Mons (*, Tanaka and others, 1992; Moore, 2001; Hauber and others, 2011). The Amazonian and Hesperian volcanic unit (AHv) includes most lava-flow surfaces that generally slope away from Tharsis, Alba, and Elysium Montes. Although individual flow surface ages are highly variable (*, Platz and Michael, 2011), we note that Late Hesperian flows are common in this unit, except in close proximity to the Tharsis Montes, where the flows are Amazonian in age (Scott and Tanaka, 1981b, 1986). Unit IHvf has been modified by extensional tectonism during the Late Hesperian, resulting in narrow grabens oriented both radial and concentric to shield structures, as well as to the elliptical crest of Syria Planum (*, Anderson and others, 2001, 2004).

The Late Hesperian transition unit (IHt) covers many lower-elevation, plains-forming parts of the highland-lowland transition zone, as well as the floor and some flank areas of Valles Marineris and a knobby plain southeast of Hesperia Planum. This unit consists of materials emplaced from erosion,

re-deposition, and mass-wasting of material from adjacent, higher-standing highland outcrops (Witbeck and others, 1991; Tanaka and others, 2003, 2005). The Amazonian and Hesperian transition undivided unit (AHtu) forms the later of the two transition undivided units, which may have been emplaced beginning in the Late Hesperian. This later unit appears to have accumulated after a hiatus, evidenced by inverted fluvial landforms (*, Burr and others, 2009), wrinkle ridges, and a denser impact crater population on the surface of unit Htu. Unit AHtu may be largely reworked from unit Htu and from itself on a continuous or episodic basis (Kerber and others, 2011). We also include in this unit an outcrop located west of Kasei Valles, surrounded by and stratigraphically within unit AHv, that is pitted and possibly layered as evidenced by changes in pit size with levels in the exposure.

Unit IHt and parts of unit IHv contain wrinkle ridges, although these have less relief than adjacent, Early Hesperian surfaces, indicating continuing global contraction after the Early Hesperian but with lower cumulative strain. Dendritic valleys locally occur on unit IHt around Echus Chasma, documenting precipitation-driven overland flow (Mangold and others, 2008). Other evidence for fluvial erosion in the Late Hesperian is sparse.

The termination of the Late Hesperian Epoch is identified herein as the broad-scale cessation of the emplacement of sedimentary plains in the northern lowlands as represented by the Late Hesperian lowlands unit, IHI (Tanaka, 1986; Parker and others, 1989; Tanaka and others, 2003, 2005; Werner and others, 2011). This unit was likely emplaced (and subsequently modified) through a variety of geologic processes and may form complexly intercalated deposits, perhaps dominated by highland debris transported via outflow channels into Chryse Planitia and the lowlands beyond (*, Parker and others, 1989; Baker and others, 1991; Kreslavsky and Head, 2002; Fairén and others, 2003; Buczkowski and Cooke, 2004; Dohm and others, 2009a). Other contributing processes may include mass wasting and fluvial dissection of the highland-lowland transition zone (*, Frey and others, 1988; Maxwell and McGill, 1988; Tanaka and others, 2001, 2003), volcanism, and eolian erosion and deposition. The IHI unit includes scattered, heavily modified materials forming low-relief and perhaps thinly buried knobs and mesas, some of which may pre-date the Late Hesperian. Unit IHI embays unit IHt and other older units, indicating distinct temporal separation. The Late Hesperian basin unit (IHb) makes up most of Hellas Planitia and may have resulted from a combination of volcanic, lacustrine, glacial, and eolian deposition (Kargel and Strom, 1992; Tanaka and Leonard, 1995; Moore and Wilhelms, 2001, 2007).

Amazonian Period

Although the Amazonian may be the longest geologic period for Mars (table 1), a cold, dry, and oxidizing environment (Bibring and others, 2006), reduced global impact flux (Hartmann and Neukum, 2001), and sporadic—though perhaps more regionally concentrated and episodic—volcanism and fluvial/glacial activity (*, Dohm and others, 2008; Neukum

and others, 2010; Grant and Wilson, 2011) suggest that rates of material deposition and cumulative amounts of geologic modification in comparison with previous epochs were significantly reduced (Golombek and others, 2006; Tanaka and others, 2014). Accumulation of polar layered deposits and dunes (*, Kolb and Tanaka, 2001; Koutnik and others, 2002), mid-latitude ice-cored lobate debris aprons (*, Pierce and Crown, 2003; Chuang and Crown, 2005; Plaut and others, 2009), and possible lower-latitude relict mountain glacial moraines likely relate to obliquity-driven effects on the climate during various episodes within the Amazonian (*, Laskar and others, 2002; Head and others, 2003). Magmatic-driven processes may have also contributed to environmental change (*, Dohm and others, 2008).

The history of polar ice and sediment accumulations is best documented for the Late Amazonian. The Amazonian polar unit (**Ap**) makes up Cavi Angusti (adjacent to Planum Australe) and is poorly dated due to modification by pits and coalesced depressions that may have resulted from removal of ice by sublimation and cryovolcanism or volcanic activity (Tanaka and Kolb, 2001; Ghatan and others, 2003).

The Amazonian volcanic edifice unit (**Ave**) consists of the largest shield volcanoes in the Tharsis region—Olympus, Alba, Ascraeus, Pavonis, and Arsia Montes. The ages of the materials buried within these edifices are unknown and may be Hesperian or earlier in age, given that surrounding lava plains of the Tharsis rise date back at least to the Late Noachian (unit **INv**). Volcanism during this period accounts for a large portion of unit **AHv** that surrounds Tharsis, Elysium, and Alba Montes. In contrast, the periphery of Olympus Mons includes several lobes of a rugged, ridged terrain mapped here as the Amazonian apron unit (**Aa**). These deposits, also known as the Olympus Mons “aureole deposits” (*, Morris, 1982; Morris and Tanaka, 1994), are interpreted to have formed by gravity-spreading of outer parts of the volcano’s shield (*, McGovern and Morgan, 2009). Unit **Aa** also includes landslides and slumps in Valles Marineris, which likely formed throughout the Amazonian (Quantin and others, 2004). The Amazonian and Hesperian transition unit (**AHtu**) continued to accumulate during the Amazonian, perhaps through volcanic air-fall deposition and eolian reworking (*, Scott and Tanaka, 1982; Hynek and others, 2003; Mandt and others, 2008; Kerber and others, 2011).

Early Amazonian Epoch

Galle and Lyot impact basins, each ~220 km in diameter and mapped as unit **AHi**, formed during this epoch. Hummocky flows compose the Amazonian volcanic unit (**AV**) in two settings. Northwest of Elysium Mons, unit **AV** flows are dissected by channels and extend >1,400 km from the margin of the Elysium rise into Utopia basin and are interpreted to be volcanically induced debris flows (lahars) that emanated from the rise and subsequently were modified by fluvial activity (*, Christiansen, 1989; Tanaka and others, 1992; Russell and Head, 2003). The **AV** unit located northwest of Olympus Mons is likely Early to Middle Amazonian lava flows (Tanaka and others, 2005), which appear to originate from beneath the Amazonian apron unit (**Aa**) and extend 2,000 km from the edifice. Average slopes

are only 0.01° for the Olympus Mons outcrop and 0.05° for the Elysium rise and Utopia basin flows. The latter largely grade into the hummocky, flat Early Amazonian basin unit (**eAb**) that fills the lowest part of Utopia Planitia. The unit also occurs as a single outcrop in the low-elevation part of Hellas Planitia, which displays layering and reticulate ridge patterns at high resolution and may be the result of deposition in ice-covered lakes and of subsequent deformation (Moore and Wilhelms, 2001, 2007).

Modest tectonism during the Early Amazonian occurred in areas where volcanism and sedimentation appear to have contributed to local crustal loading. Northeast of Alba Mons, northernmost extensions of densely arrayed narrow grabens dissect the Late Hesperian lowland unit (**IHI**); the overall fault system that deforms Alba Mons may have resulted from regional rifting due to northwest-southeast extension and local, hotspot-induced buoyant doming of the Alba Mons shield (*, Tanaka, 1990; Cailleau and others, 2005). In addition, gravitational shear stresses resulting from the immense shield may have caused it to spread northward toward the lowlands, prior to building of the summit edifice (Ivanov and Head, 2006). Northwest of Alba Mons, wrinkle ridges oriented circumferential to the edifice may have formed in response to lithospheric loading imposed by growth of the shield and by overall loading of the Tharsis rise (*, Banerdt and others, 1992; Watters, 1993; Head and others, 2002). Wrinkle ridges associated with Utopia and Isidis Planitiae similarly may have resulted from loading by emplacement of volcanic, lowland, and basin units, including units **AHv**, **Av**, **IHI**, **eAb**, and possibly earlier transition units; deformation may have begun in the Hesperian (or Noachian) and continued into the Early Amazonian (Thomson and Head, 2001; Head and others, 2002; Tanaka and others, 2003, 2005).

Middle Amazonian Epoch

This epoch features emplacement of the Middle Amazonian lowland unit (**mAl**), based on superposition relations and crater counts (Werner and others, 2011; Skinner and others, 2012). This unit formerly covered much of the northern lowlands, but the majority of the unit appears to have been removed (Skinner and others, 2012), accounting for extensive remnant crater-topped mounds and mesas of the unit commonly referred to as “pedestal craters” (*, Kadish and others, 2010). The unit may be mostly dust and ice derived from erosion of the Hesperian polar undivided unit (**Hpu**); subsequent, gradual erosion of unit **mAl** led to pedestal crater formation and perhaps re-deposition as the Amazonian polar undivided unit (**Apu**) (Skinner and others, 2012).

Elsewhere, Middle Amazonian geologic activity included (1) continued but reduced volcanism in the Tharsis and Elysium regions (contributing to units **AHv** and **Av**) (Hauber and others, 2011; Platz and Michael, 2011) and perhaps in the highland-lowland transition zone (unit **AHtu**) (*, Hynek and others, 2003) and (2) apron unit (**Aa**) development at Olympus Mons and Valles Marineris and along the highland-lowland transition (unit **ANa**). Evidence for Middle Amazonian tectonism is sparse (*, Anderson and others, 2001).

Late Amazonian Epoch

This epoch includes substantial coverage of low-lying parts of Amazonis Planitia by sparsely cratered lava flows sourced southwest of Olympus Mons and flow fields south and east of the Elysium rise that erupted from Cerberus Fossae (*, Fuller and Head, 2002; Plescia, 2003; Tanaka and others, 2005; Dohm and others, 2008; Vaucher and others, 2009; Hamilton and others, 2010; Hauber and others, 2011; Platz and Michael, 2011). Part of the Cerberus Fossae flows reach into Amazonis and Arcadia Planitiae, where they overlie older volcanic flows as well as transitional and lowland units. These outcrops, as well as other flows surrounding the base of Olympus Mons and south of Alba Mons, are mapped as the Late Amazonian volcanic unit (IAV). In Elysium Planitia, unit IAV includes a branch that extends northward along the eastern margin of Elysium Mons (Hamilton and others, 2010; Hamilton, 2013). The Late Amazonian volcanic field unit (IAVf) is composed of groups of small basaltic shields, fissure vents, and emanating lava flows; the unit occurs in central parts of the Tharsis rise and at Cerberus Fossae, commonly along graben swarms (*, Bleacher and others, 2007; Vaucher and others, 2009; Hauber and others, 2011). Formation of narrow grabens and wrinkle ridges during the Late Amazonian is limited to volcanic regions and generally follows older deformation patterns.

The Amazonian polar undivided unit (Apu) was emplaced on the polar plateaus, Planum Boreum and Planum Australe, during the Late Amazonian (Tanaka and Kolb, 2001; Koutnik and others, 2002; Tanaka, 2005; Tanaka and others, 2008; Tanaka and Fortezzo, 2012). These deposits are overlain by residual ices, forming the Late Amazonian polar cap unit (IAPc). The south polar ice cap is colder than the north polar ice cap due to its higher elevation and includes carbon dioxide ice overlying water ice (*, Byrne, 2009), as well as a buried, pitted radar-transparent material as much as 300 m thick that is interpreted to be carbon dioxide ice (Phillips and others, 2011). Planum Boreum is surrounded by the most extensive accumulations of dune sands on Mars, mapped as the Late Amazonian polar dune unit (IAPd) (Tanaka and Fortezzo, 2012); unmapped, smaller patches of dunes occur globally (*, Hayward and others, 2007). The Late Amazonian apron unit (IAa) occurs along the western to northwestern flanks of the Tharsis Montes and Olympus Mons and was mapped in greater detail by Morris and Tanaka (1994), Scott and Zimbelman (1995), and Scott and others (1998). This unit is dominated by ribbed, lobate aprons that are interpreted as drop moraines produced by cold-based glaciers (*, Head and others, 2003).

Major Results

Several advancements in the characterization and analysis of Martian geology have resulted from this global mapping effort, in part determined by additional studies (see cited references):

1. This map is based mainly on improved topographic and image data not available in the previous global mapping

effort, enabling much more consistent observation of critical morphologic details and stratigraphic relations that have resulted in a very different and more refined map (compare tables 6 and 7). Highland materials make up 44 percent of the surface, volcanic materials 22 percent, and other basin, transition, lowland, polar, apron, and impact materials make up the remaining 34 percent (Tanaka and others, 2014).

2. Compilation of stratigraphic relations and crater-density statistics for map units on a global scale have resulted in the most accurate planet-wide dating of Martian geologic materials yet achieved (see also Platz and others, 2013). A revised list of referent map units has been selected to define each of the eight Martian epochs (table 1). For the first time on a geologic map of Mars, chronostratigraphic ages are incorporated in unit names.
3. The surface of Mars is appreciably older overall than previously understood. The Noachian makes up 45 percent of the surface, the Hesperian 29 percent, and the Amazonian 26 percent. (For more details on the character and resurfacing rates of Mars through time, see Tanaka and others, 2014).
4. The Early, Middle, and Late Noachian highland units (eNh, mNh, and lNh, respectively) have statistically distinct ages, and the units occur at progressively lower mean elevations with successively younger age. Crater morphology statistics indicate that Noachian resurfacing was spatially non-uniform, long-lived, and gravity driven, which is consistent with volcanism and arid-zone fluvial and aeolian erosion (Irwin and others, 2013).
5. All impact basins >150 km in diameter have been dated and show a dramatically reduced rate of formation over time: >65 for Early Noachian, >15 for Middle Noachian, ~3 for Late Noachian, ~4 for Hesperian, and 2 for Early Amazonian (table 4).

Acknowledgments

Stuart Robbins (University of Colorado, Boulder) generously supplied us with his global digital crater database of Mars (Robbins and Hynek, 2012) prior to its publication. We are indebted to Mike Carr, David Crown, Ernst Hauber, Brian Hynek, Scott Mest, Mike Shand, Mike Smith, and David Williams for constructive reviews. We also benefited from discussions, conference presentations, and publications of many other researchers referenced herein. Most of this work was supported by NASA's Planetary Geology and Geophysics Program. Work by Platz was funded by the Helmholtz Association through the research alliance "Planetary Evolution and Life" and a German Research Foundation (Deutsche Forschungsgemeinschaft) grant (PL613/1), and efforts by

Michael by the German Space Agency (Deutsches Zentrum für Luft- und Raumfahrt, Bonn), grant 50QM1001 (High Resolution Stereo Camera on Mars Express), on behalf of the German Federal Ministry of Economics and Technology.

References Cited

- Acuña, M.H., Connerney, J.E.P., Wasilewski, R.P., and 11 others, 2001, Magnetic field of Mars—Summary of results from the aerobraking and mapping orbits: *Journal of Geophysical Research*, v. 106, no. E10, p. 23,404–23,417.
- Anderson, R.C., Dohm, J.M., Golombek, M.P., and 5 others, 2001, Significant centers of tectonic activity through time for the western hemisphere of Mars: *Journal of Geophysical Research*, v. 106, p. 20,563–20,585.
- Anderson, R.C., Dohm, J.M., Haldemann, A.F.C., Hare, T.M., Baker, V.R., 2004, Tectonic histories between Alba Patera and Syria Planum, Mars: *Icarus*, v. 171, p. 31–38.
- Anderson, R.S., and Anderson, S.P., 2010, *Geomorphology—The mechanics and chemistry of landscapes*: New York, Cambridge University Press, 654 p.
- Andrews-Hanna, J.C., 2012, The formation of Valles Marineris—1. Tectonic architecture and the relative roles of extension and subsidence: *Journal of Geophysical Research*, v. 117, no. E03006 (doi:10.1029/2011JE003953).
- Andrews-Hanna, J.C., Phillips, R.J., and Zuber, M.T., 2007, Meridiani Planum and the global hydrology of Mars: *Nature*, v. 446, p. 163–166 (doi:10.1038/nature05594).
- Andrews-Hanna, J.C., Zuber, M.T., and Banerdt, B., 2008, The Borealis basin and the origin of the Martian crustal dichotomy: *Nature*, v. 453, p. 1212–1215 (doi:10.1038/nature07011).
- Baker, V.R., Carr, M.H., Gulick, V.C., Williams, C.R., and Marley, M.S., 1992, Channels and valley networks, in Kieffer, H.H., Jakosky, B.M., Snyder, C.W., and Matthews, M.S., eds., *Mars: Tucson*, University of Arizona Press, p. 493–522.
- Baker, V.R., Maruyama, Shigenori, Dohm, J.M., 2007, Tharsis superplume and the geological evolution of early Mars, in Yuen, D.A., Maruyama, Shigenori, Karato, S.-I., and Windley, B.F., eds., *Superplumes—Beyond plate tectonics*: Dordrecht, Springer, p. 507–523.
- Baker, V.R., Strom, R.G., Gulick, V.C., and 3 others, 1991, Ancient oceans, ice sheets, and the hydrological cycle on Mars: *Nature*, v. 352, p. 589–594.
- Bandfield, J.L., Hamilton, V.E., and Christensen, P.R., 2000, A global view of Martian surface compositions from MGS-TES: *Science*, v. 287, p. 1626–1630.
- Banerdt, W.B., Golombek, M.P., and Tanaka, K.L., 1992, Stress and tectonics on Mars, in Kieffer, H.H., Jakosky, B.M., Snyder, C.W., and Matthews, M.S., eds., *Mars: Tucson, Ariz.*, University of Arizona Press, P. 249–297.
- Banks, M.E., Byrne, Shane, Galla, Kapil, and 6 others, 2010, Crater population and resurfacing of the Martian north polar layered deposits: *Journal of Geophysical Research*, v. 115, no. E08006 (doi:10.1029/2009JE003523).
- Barlow, N.G., 2008, *Mars—An introduction to its interior, surface, and atmosphere*: Cambridge, Cambridge University Press, 264 p.
- Batson, R.M., Bridges, P. M., and Inge, J.L., 1979, *Atlas of Mars, the 1:5,000,000 map series*: National Aeronautics and Space Administration Special Publication 438, 146 p.
- Bell, J.F., ed., 2008, *The Martian surface—Composition, mineralogy, and physical properties*: Cambridge, Cambridge University Press, 636 p.
- Bibring, J.-P., Langevin, Yves, Gendrin, Aline, and 37 others, 2005, Mars surface diversity as revealed by the OMEGA/Mars Express observations: *Science*, v. 307, p. 1576–1581.
- Bibring, J.-P., Langevin, Yves, Mustard, J.F., and 40 others, 2006, Global mineralogical and aqueous Mars history derived from OMEGA/Mars Express data: *Science*, v. 312, p. 400–404.
- Bleacher, J.E., Greeley, Ronald, Williams, D.A., and 2 others, 2007, Trends in effusive style at the Tharsis Montes, Mars, and implications for the development of the Tharsis province: *Journal of Geophysical Research*, v. 112, no. E09005 (doi:10.1029/2006JE002873).
- Bleamaster, L.F., and Crown, D.A., 2010, Geologic map of MTM–40277, –45277, –40272, and –45272 quadrangles, eastern Hellas Planitia regions of Mars: U.S. Geological Survey Scientific Investigations Map 3096, scale 1:1,000,000.
- Bouysee, Philippe, 2009, *Geological map of the world at 1:50,000,000 (3rd ed.)*: Paris, France, Commission for the Geological Map of the World, scale 1:50,000,000, two sheets and explanatory notes.
- Buczowski, D.L., and Cooke, M.L., 2004, Formation of double-ring circular grabens due to volumetric compaction over buried impact craters—Implications for thickness and nature of cover material in Utopia Planitia, Mars: *Journal of Geophysical Research*, v. 109, no. E02006 (doi:10.1029/2003JE002144).
- Burr, D.B., Nega, M.-T., Williams, R.M.E., and 3 others, 2009, Pervasive aqueous paleoflow features in the Aeolis/Zephyria Plana region, Mars: *Icarus*, v. 200, p. 52–76 (doi:10.1016/j.icarus.2008.10.014).
- Byrne, Shane, 2009, The polar deposits of Mars: *Annual Reviews of Earth and Planetary Science*, v. 37, p. 535–560.
- Cabrol, N.A., and Grin, E.A., 1999, Distribution, classification, and ages of Martian impact crater lakes: *Icarus*, v. 142, p. 160–172.
- Cailleau, Béatrice, Walter, T.R., Janle, Peter, and Hauber, Ernst, 2005, Unveiling the origin of radial grabens on Alba Patera volcano by finite element modeling: *Icarus*, v. 176, p. 44–56 (doi:10.1016/j.icarus.2005.01.017).
- Carr, M.H., 1979, Formation of Martian flood features by release of water from confined aquifers: *Journal of Geophysical Research*, v. 84, p. 2995–3007.
- Chapman, M.G., Neukum, Gerhard, Dumke, Alexander, and 8 others, 2010, Noachian-Hesperian geologic history of

- the Echus Chasma and Kasei Valles system on Mars—
New data and interpretations: *Earth and Planetary
Science Letters*, v. 294, p. 256–271 (doi:10.1016/j.
epsl.2009.11.032).
- Christensen, P.R., Jakosky, B.M., Kieffer, H.H., and 8 others,
2004, The Thermal Emission Imaging System (THEMIS)
for the Mars 2001 Odyssey mission: *Space Science
Reviews*, v. 110, p. 85–130.
- Christiansen, E.H., 1989, Lahars in the Elysium region of Mars,
Geology, v. 17, p. 203–206.
- Chuang, F.C., and Crown, D.A., 2005, Surface characteristics
and degradational history of debris aprons in the Tempe
Terra/Mareotis Fossae region of Mars: *Icarus*, v. 179, p.
24–42 (doi:10.1016/j.icarus.2005.05.014).
- Chuang, F.C., and Crown, D.A., 2009, Geologic map of MTM
35337, 40337, and 45337 quadrangles, Deuteronilus
Mensae region of Mars: U.S. Geological Survey Scientific
Investigations Map 3079, scale 1:1,000,000.
- Connerney, J.E.P., Acuña, M.H., Wasilewski, P.J., and 5 others,
2001, The global magnetic field of Mars and implications
for crustal evolution: *Geophysical Research Letters*, v. 28,
no. 21, p. 4015–4018.
- Craddock, R.A., and Howard, A.D., 2002, The case for rainfall on
a warm, wet early Mars: *Journal of Geophysical Research*,
v., 107, no. E11, 5111 (doi:10.1029/2001JE001505).
- Crown, D.A., Bleamaster, L.F., III, and Mest, S.C., 2005, Styles
and timing of volatile-driven activity in the eastern Hellas
region of Mars: *Journal of Geophysical Research*, v. 110,
no. E12S22 (doi:10.1029/2005JE002496).
- Crown, D.A., and Greeley, Ronald, 1993, Volcanic geol-
ogy of Hadriaca Patera and the eastern Hellas region
of Mars: *Journal of Geophysical Research*, v. 98, p.
3431–3451.
- Crown, D.A., and Greeley, Ronald, 2007, Geologic map
of MTM –30262 and –30267 quadrangles, Hadriaca
Patera region of Mars: U.S. Geological Survey Scientific
Investigations Map 2936, scale 1:1,004,000.
- Crown, D.A., Price, K.H., and Greeley, Ronald, 1992, Geologic
evolution of the east rim of the Hellas basin, Mars: *Icarus*,
v. 100, p. 1–25.
- Crumpler, L.S., Craddock, R.A., and Aubele, J.C., 2001,
Geologic map of the MTM 25047 and 20047 quadrangles,
central Chryse Planitia/Viking 1 Lander site, Mars: U.S.
Geological Survey Geologic Investigations Series Map
I–2693, scale 1:1,000,000.
- Crumpler, L.S., Head, J.W., and Aubele, J.C., 1996, Calderas
on Mars—Characteristics, structure, and associated
flank deformation: Geological Society, London, Special
Publications, January 1, 1996, v. 110, p. 307–348
(doi:10.1144/GSL.SP.1996.110.01.24).
- Davila, A.F., Fairén, A.G., Stokes, C.R., and 5 others, 2013,
Evidence for Hesperian glaciation along the Martian
dichotomy boundary: *Geology*, v. 41, no. 7, p. 755–758
(doi:10.1130/G34201.1).
- Des Marais, D.J., 2010, Exploring Mars for evidence of habit-
able environments and life: *Proceedings of the American
Philosophical Society*, v. 154, no. 4, p. 402–421.
- DiAchille, Gaetano, and Hynek, B.M., 2010, Ancient ocean on
Mars supported by global distribution of deltas and val-
leys: *Nature Geoscience*, v. 3, p. 459–463 (doi:10.1038/
ngeo891).
- DiBiase, R.A., Limaye, A.B., Scheingross, J.S., Fischer, W.W.,
and Lamb, M.P., 2013, Deltaic deposits at Aeolis Dorsa—
Sedimentary evidence for a standing body of water on
the northern plains of Mars: *Journal of Geophysical
Research, Planets*, v. 118, p. 1285–1302 (doi:10.1002/
jgre.20100).
- Dickson, J.L., Head, J.W., and Marchant, D.R., 2008, Late
Amazonian glaciation at the dichotomy boundary on
Mars—Evidence for glacial thickness and multiple
glacial phases: *Geology*, v. 36, 411–414 (doi:10.1130/
G24382A.1).
- Dohm, J.M., Anderson, R.C., Barlow, N.G., and 19 others,
2008, Recent geological and hydrological activity on
Mars—The Tharsis/Elysium corridor: *Planetary and
Space Science*, v. 56, no. 7, p. 985–1013 (doi:10.1016/j.
pss.2008.01.001).
- Dohm, J.M., Baker, V.R., Boynton, W.V., and 18 others,
2009a, GRS evidence and the possibility of ancient
oceans on Mars: *Planetary and Space Science*, v. 57, p.
664–684.
- Dohm, J.M., Ferris, J.C., Baker, V.R., and 7 others, 2001b,
Ancient drainage basin of the Tharsis region, Mars—
Potential source for outflow channel systems and putative
oceans or paleolakes: *Journal of Geophysical Research*, v.
106, p. 32,943–32,958.
- Dohm, J.M., Miyamoto, Hirdy, Maruyama, Shigenori, and 11
others, 2013, Mars evolution, in A.G. Fairén, ed., *Mars—
Evolution, geology, and exploration*: Hauppauge, NY,
Nova Science Publishers, Inc., p. 1–34.
- Dohm, J.M., Tanaka, K.L., and Hare, T.M., 2001a, Geologic,
paleotectonic, and paleoerosional maps of the Thaumasia
region, Mars: U.S. Geological Survey Geologic
Investigations Series Map I–2650, scale 1:5,000,000.
- Dohm, J.M., Williams, J.-P., Anderson, R.C., and 13 others,
2009b, New evidence for a magmatic influence on the
origin of Valles Marineris, Mars: *Journal of Volcanology
and Geothermal Research*, v. 185, p. 12–27.
- Edwards, C.S., Nowicki, K.J., Christensen, P.R., and 3
others, 2011, Mosaicking of global planetary image
datasets—1. Techniques and data processing for Thermal
Emission Imaging System (THEMIS) multi-spectral data:
Journal of Geophysical Research, v. 116, no. E10008
(doi:10.1029/2010JE003755).
- Ehlmann, B.L., Mustard, J.F., Murchie, S.L., and 11 others,
2008, Orbital identification of carbonate-bearing rocks on
Mars: *Science*, v. 322, p. 1828–1832.
- Ehlmann, B.L., Mustard, J.F., Murchie, S.L., and 4 others,
2011, Subsurface water and clay mineral formation
during the early history of Mars: *Nature*, v. 479, p. 53–60
(doi:10.1038/nature10582).
- Ehlmann, B.L., Mustard, J.F., Swayze, G.A., and 9 others,
2009, Identification of hydrated silicate minerals on
Mars using MRO-CRISM—Geologic context near

- Nili Fossae and implications for aqueous alteration: *Journal of Geophysical Research*, v. 114, no. E00D08 (doi:10.1029/2009JE003339).
- El Maarry, M.R., Dohm, J.M., Marzo, G.A., and 5 others, 2012, Searching for evidence of hydrothermal activity at Apollinaris Mons, Mars: *Icarus*, v. 217, p. 297–314 (doi:10.1016/j.icarus.2011.10.022).
- Fairén, A.G., Davila, A.F., Gago-Duport, L., Haqq-Misra, J.D., Gil, C., McKay, C.P., and Kasting, J.F., 2011, Cold glacial oceans would have inhibited phyllosilicate sedimentation on early Mars: *Nature Geoscience*, v. 4667–4670.
- Fairén, A.G., Dohm, J.M., Baker, V.R., de Pablo, M.A., Ruiz, J., Ferris, J.C., and Anderson, R.C., 2003, Episodic flood inundations of the northern plains of Mars: *Icarus*, v. 165, p. 53–67.
- Fassett, C.I., and Head, J.W., III, 2008a, The timing of Martian valley network activity—Constraints from buffered crater counting: *Icarus*, v. 195, p. 61–89 (doi:10.1016/j.icarus.2007.12.009).
- Fassett, C.I., and Head, J.W., III, 2008b, Valley network-fed, open-basin lakes on Mars—Distribution and implications for Noachian surface and subsurface hydrology: *Icarus*, v. 198, p. 37–56 (doi:10.1016/j.icarus.2008.06.016).
- Federal Geographic Data Committee [prepared for the Federal Geographic Data Committee by the U.S. Geological Survey], 2006, FGDC Digital Cartographic Standard to Geologic Map Symbolization: Reston, Va., Federal Geographic Data Committee Document Number FGDC-STD-013–2006, 290 p., 2 plates.
- Ferguson, R.L., Christensen, P.R., and Kieffer, H.H., 2006, High resolution thermal inertia derived from THEMIS—Thermal model and applications: *Journal of Geophysical Research*, v. 111, no. E12004 (doi:10.1029/2006JE002735).
- Frey, H.V., 2006, Impact constraints on, and a chronology for, major events in early Mars history: *Journal of Geophysical Research*, v. 111, no. E08S91 (doi:10.1029/2005JE002449).
- Frey, H.V., Roark, J.H., Shockey, K.M., Frey, E.L., and Sakimoto, S.E.H., 2002, Ancient lowlands on Mars: *Geophysical Research Letters*, v. 29, no. 10, 1384, (doi:10.1029/2001GL013832).
- Frey, H.V., Semeniuk, A.M., Semeniuk, J.A., and Tokarcik, Susan, 1988, A widespread common age resurfacing event in the highland-lowland transition zone in eastern Mars: *Proceedings of the Lunar and Planetary Science Conference*, 18th, p. 679–699.
- Fuller, R.R., and Head, J.W., III, 2002, Amazonis Planitia—The role of geologically recent volcanism and sedimentation in the formation of the smoothest plains on Mars: *Journal of Geophysical Research*, v. 107, no. E10, p. 11–1—11–25 (doc. no. 5081, doi:10.1029/2002JE001842).
- Ghatan, G.J., and Head, J.W., III, 2004, Regional drainage of meltwater beneath a Hesperian-aged south circumpolar ice sheet on Mars: *Journal of Geophysical Research*, v. 109, no. E07006 (doi:10.1029/2003JE002196).
- Ghatan, G.J., Head, J.W., III, and Pratt, Stephen, 2003, Cavi Angusti, Mars—Characterization and assessment of possible formation mechanisms: *Journal of Geophysical Research*, v. 108, no. E5, p. 11–1 to 11–19 (doc. no. 5045, doi:10.1029/2002JE001972).
- Golombek, M.P., Anderson, F.S., and Zuber, M.T., 2001, Martian wrinkle ridge topography—Evidence for subsurface faults from MOLA: *Journal of Geophysical Research*, v. 106, no. E10, p. 23,811–23,821 (doi:10.1029/2000JE001308).
- Golombek, M.P., Cook, R.A., Economou, Thanasis, and 11 others, 1997, Overview of the Mars Pathfinder mission and assessment of landing site predictions: *Science*, v. 278, p. 1743–1748.
- Golombek, M.P., Grant, J.A., Crumpler, L.S., and 8 others, 2006, Erosion rates at the Mars Exploration Rover landing sites and long-term climate change on Mars: *Journal of Geophysical Research*, v. 111, no. E12S10 (doi:10.1029/2006JE002754).
- Goudge, T.A., Head, J.W., Mustard, J.F., and Fassett, C.I., 2012, An analysis of open-basin lake deposits on Mars—Evidence for the nature of associated lacustrine deposits and post-lacustrine modification processes: *Icarus*, v. 219, p. 211–229 (doi:10.1016/j.icarus.2012.02.027).
- Grant, J.A., and Schultz, P.H., 1990, Gradational epochs on Mars—Evidence from west-northwest of Isidis Basin and Electris: *Icarus*, v. 84, p. 166–195.
- Grant, J.A., and Wilson, S.A., 2011, Late alluvial fan formation in southern Margaritifer Terra, Mars: *Geophysical Research Letters*, v. 38, no. L08201 (doi:10.1029/2011GL046844).
- Grant, J.A., Wilson, S.A., Fortezzo, C.M., and Clark, D.A., 2009, Geologic map of MTM –20012 and –25012 quadrangles, Margaritifer Terra region of Mars: U.S. Geological Survey Scientific Investigations Map 3041, scale 1:1,000,000.
- Greeley, Ronald, and Crown, D.A., 1990, Volcanic geology of Tyrrhena Patera, Mars: *Journal of Geophysical Research*, v. 95, p. 7133–7149.
- Greeley, Ronald, Foing, B.H., McSween, H.Y., Jr., and 6 others, 2005, Fluid lava flows in Gusev crater, Mars: *Journal of Geophysical Research*, v. 110, no. E05008 (doi:10.1029/2005JE002401).
- Greeley, Ronald, and Guest, J.E., 1987, Geologic map of the eastern equatorial region of Mars: U.S. Geological Survey Miscellaneous Investigations Series Map I–1802–B, scale 1:15,000,000.
- Gregg, T.K.P., Crown, D.A., and Greeley, Ronald, 1998, Geologic map of MTM quadrangle –20252, Tyrrhena Patera region of Mars: U.S. Geological Survey Miscellaneous Investigations Series Map I–2556, scale 1:500,000.
- Grosfils, E.B., and Head, J.W., 1994, The global distribution of giant radiating dike swarms on Venus—Implications for the global stress state: *Geophysical Research Letters*, v. 21, p. 701–704.
- Grotzinger, J.P., Arvidson, R.E., Bell, J.F., III, and 17 others, 2005, Stratigraphy and sedimentology of a dry to wet eolian depositional system, Burns formation, Meridiani

- Planum, Mars: *Earth and Planetary Science Letters*, v. 240, p. 11–72 (doi:10.1016/j.epsl.2005.09.039).
- Hamilton, C.W., 2013, Flood lavas associated with the Cerberus Fossae 2 unit in Elysium Planitia, Mars [abs.], *in* Lunar and Planetary Science Conference LXXV, Abstract #3070 [CD-ROM; online].
- Hamilton, C.W., Fagents, S.A., and Wilson, Lionel, 2010, Explosive lava-water interactions in Elysium Planitia, Mars—Constraints on the formation of the Tartarus Colles cone groups: *Journal of Geophysical Research*, v.115, no. E9 (doi:10.1029/2009JE003546).
- Hansen, V.L., 2000, Geologic mapping of tectonic planets: *Earth and Planetary Science Letters*, v. 176, p. 527–542.
- Hartmann, W.K., 2005, Martian cratering 8—Isochron refinement and the chronology of Mars: *Icarus*, v. 174, p. 294–320 (doi:10.1016/j.icarus.2004.11.023).
- Hartmann, W.K., and Neukum, Gerhard, 2001, Cratering chronology and the evolution of Mars: *Space Science Reviews*, v. 96, p. 165–194.
- Hauber, Ernst, Brož, Petr, Jagert, Felix, Jodłowski, Piotr, and Platz, Thomas, 2011. Very recent and wide-spread basaltic volcanism on Mars: *Geophysical Research Letters*, v. 38, no. L10201 (doi:10.1029/2011GL047310).
- Hauber, Ernst, Grott, Matthias, and Kronberg, Peter, 2010, Martian rifts—Structural geology and geophysics: *Earth and Planetary Science Letters*, v. 294, p. 393–410 (doi:10.1016/j.epsl.2009.11.005).
- Hayward, R.K., Mullins, K.F., Fenton, L.K., and 5 others, 2007, Mars global digital dune database and initial science results: *Journal of Geophysical Research*, v. 112, no. E11007 (doi:10.1029/2007JE002943).
- Head, J.W., III, Kreslavsky, M.A., and Pratt, Stephen, 2002, Northern lowlands of Mars—Evidence for widespread volcanic flooding and tectonic deformation in the Hesperian Period: *Journal of Geophysical Research*, v. 107, no. E1, 5004 (10.1029/2000JE001445).
- Head, J.W., Mustard, J.F., Kreslavsky, M.A., Milliken, R.E., and Marchant, D.R., 2003, Recent ice ages on Mars: *Nature*, v. 426, p. 797–802.
- Head, J.W., III, and Pratt, Stephen, 2001, Extensive Hesperian-aged south polar ice sheet on Mars—Evidence for massive melting and retreat, and lateral flow and ponding of meltwater: *Journal of Geophysical Research*, v. 106, no. E6, p. 12,275–12,299.
- Hiesinger, Harald, and Head, J.W., III, 2000, Characteristics and origin of the polygonal terrain in southern Utopia Planitia, Mars—Results from Mars Orbiter Laser Altimeter and Mars Orbiter Camera data: *Journal of Geophysical Research*, v. 105, p. 11,999–12,022.
- Hiesinger, Harald, and Head, J.W., III, 2002, Topography and morphology of the Argyre Basin, Mars—Implications for its geologic and hydrologic history: *Planetary and Space Science*, v. 50, p. 929–981.
- Hiesinger, Harald, and Head, J.W., III, 2004, The Syrtis Major volcanic province, Mars—Synthesis from Mars Global Surveyor data: *Journal of Geophysical Research*, v. 109, no. E01004 (doi:10.1029/2003JE002143).
- Hodges, C.A., and Moore, H.J., 1994, Atlas of volcanic landforms on Mars: U.S. Geological Survey Professional Paper 1534, 194 p.
- Hoke, M.R.T., and Hynek, B.M., 2009, Roaming zones of precipitation on ancient Mars as recorded in valley networks: *Journal of Geophysical Research*, v. 114, no. E08002 (doi:10.1029/2008JE003247).
- Howard, A.D., 1978, Origin of the stepped topography of the Martian poles: *Icarus*, v. 34, p. 581–599.
- Howard, A.D., 2000, The role of eolian processes in forming surface features of the Martian polar layered deposits: *Icarus*, v. 144, p. 267–288.
- Howard, A.D., Moore, J.M., and Irwin, R.P., III, 2005, An intense terminal epoch of widespread fluvial activity on early Mars—1. Valley network incision and associated deposits: *Journal of Geophysical Research*, v. 110, no. E12S14 (doi:10.1029/2005JE002459).
- Hynek, B.M., Beach, Michael, and Hoke, M.R.T., 2010, Updated global map of Martian valley networks and implications for climate and hydrologic processes: *Journal of Geophysical Research*, v. 115, no. E09008 (doi:10.1029/2009JE003548).
- Hynek, B.M., and Phillips, R.J., 2008, The stratigraphy of Meridiani Planum, Mars, and implications for the layered deposits’ origin: *Earth and Planetary Science Letters*, v. 274, p. 214–220 (doi:10.1016/j.epsl.2008.07.025).
- Hynek, B.M., Phillips, R.J., and Arvidson, R.E., 2003, Explosive volcanism in the Tharsis region—Global evidence in the Martian geologic record: *Journal of Geophysical Research*, v. 111, no. E9 (doc no. 5111, doi:10.1029/2003JE002062).
- Irwin, R.P., III, and Grant, J.A., 2009, Large basin overflow floods on Mars, *in* Burr, D.M., Carling, P.A., and Baker, V.R., eds., *Megaflooding on Earth and Mars*: Cambridge, UK, Cambridge University Press, p. 209–224.
- Irwin, R.P., III, and Grant, J.A., 2013, Geologic map of MTM –15027, –20027, –25027, and –25032 quadrangles, Margaritifer Terra region of Mars: U.S. Geological Survey Science Investigations Map 3209, scale 1:1,000,000.
- Irwin, R.P., III, Howard, A.D., Craddock, R.A., and Moore, J.M., 2005, An intense terminal epoch of widespread fluvial activity on early Mars—2. Increased runoff and paleolake development: *Journal of Geophysical Research*, v. 110, no. E12S15 (doi:10.1029/2005JE002460).
- Irwin, R.P., III, Howard, A.D., and Maxwell, T.A., 2004, Geomorphology of Ma’adim Vallis, Mars, and associated paleolake basins: *Journal of Geophysical Research*, v. 109, no. E12009 (doi:10.1029/2004JE002287).
- Irwin, R.P., III, Tanaka, K.L., and Robbins, S.J., 2013, Distribution of Early, Middle, and Late Noachian cratered surfaces in the Martian highlands—Implications for resurfacing events and processes: *Journal of Geophysical Research*, v. 118, 1–14 (doi:10.1002/jgr.20053).
- Ivanov, B.A., 2001, Mars/Moon cratering rate ratio estimates: *Space Science Reviews*, v. 96, p. 87–104.
- Ivanov, M.A., and Head, J.W., 2006, Alba Patera, Mars—Topography, structure, and evolution of a unique

- late Hesperian–early Amazonian shield volcano: *Journal of Geophysical Research*, v. 111, no. E09003 (doi:10.1029/2005JE002469).
- Kadish, S.J., Head, J.W., and Barlow, N.G., 2010, Pedestal crater heights on Mars—A proxy for the thicknesses of past, ice-rich, Amazonian deposits: *Icarus*, v. 210, p. 92–101 (doi:10.1016/j.icarus.2010.06.021).
- Kargel, J.S., and Strom, R.G., 1992, Ancient glaciation on Mars: *Geology*, v. 20, p. 3–7.
- Kerber, Laura, and Head, J.W., 2010, The age of the Medusae Fossae Formation—Evidence of Hesperian emplacement from crater morphology, stratigraphy, and ancient lava contacts: *Icarus*, v. 206, p. 669–684 (doi:10.1016/j.icarus.2009.10.001).
- Kerber, Laura, Head, J.W., Madeleine, J.-B., Forget, François, and Wilson, Lionel, 2011, The dispersal of pyroclasts from Apollinaris Patera, Mars—Implications for the origin of the Medusae Fossae Formation: *Icarus*, v. 216, p. 212–220 (doi:10.1016/j.icarus.2011.07.035).
- Klein, H.P., Horowitz, N.H., and Biemann, Klaus, 1992: The search for extant life on Mars, *in* Kieffer, H.H., Jakosky, B.M., Snyder, C.W., and Matthews, M.S., eds., *Mars: Tucson*, University of Arizona Press, p. 1221–1245.
- Kneissl, Thomas, van Gasselt, Stephan, and Neukum, Gerhard, 2011, Map-projection-independent crater size-frequency determination in GIS environments—New software tool for ArcGIS: *Planetary and Space Science*, v. 59, p. 1243–1254 (doi:10.1016/j.pss.2010.03.015).
- Kolb, E.J., and Tanaka, K.L., 2001, Geologic history of the polar regions of Mars based on Mars Global Surveyor data—II. Amazonian Period: *Icarus*, v. 154, p. 22–39.
- Kopparapu, R.K., Ramirez, Ramses, Kasting, J.F., and 7 others, 2013, Habitable zones around main-sequence stars—New estimates: *The Astrophysics Journal*, v. 265, no. 2, 131 (doi:10.1088/0004-637X/765/2/131).
- Koutnik, M.R., Byrne, Shane, and Murray, B.C., 2002, South polar layered deposits of Mars—The cratering record: *Journal of Geophysical Research*, v. 107, no. E11, p. 5100–5112.
- Kreslavsky, M.A., and Head, J.W., III, 2000, Kilometer-scale roughness of Mars—Results from MOLA data analysis: *Journal of Geophysical Research*, v. 105, no. E11, p. 26,695–26,711.
- Kreslavsky, M.A., and Head, J.W., III, 2002, Fate of outflow channel effluents in the northern lowlands of Mars—The Vastitas Borealis Formation as a sublimation residue from frozen ponded bodies of water: *Journal of Geophysical Research*, v. 107, no. E12, p. 4–1 to 4–25 (doc. no. 5121, doi:10.1029/2001JE001831).
- Kronberg, Peter, Hauber, Ernst, Grott, Matthias, and 6 others, 2007, Acheron Fossae, Mars—Tectonic rifting, volcanism, and implications for lithospheric thickness: *Journal of Geophysical Research*, v. 112, no. E04005 (doi:10.1029/2006JE002780).
- Langevin, Ives, Poulet, François, Bibring, J.-P., and Gondet, Brigitte, 2005, Sulfates in the north polar region of Mars detected by OMEGA/Mars Express: *Science*, v. 307, p. 1584–1586.
- Langlais, B., Purucker, M.E., and Manda, Mioara, 2004, Crustal magnetic field of Mars: *Journal of Geophysical Research*, v. 109, no. E02008 (doi:10.1029/2003JE002048).
- Laskar, Jacques, Correia, A.C.M., Gastineau, Mickaël, and 3 others, 2004, Long term evolution and chaotic diffusion of the insolation quantities of Mars: *Icarus*, v. 170, p. 343–364 (doi:10.1016/j.icarus.2004.04.005).
- Laskar, Jacques, Levrard, Benjamin, and Mustard, J.F., 2002, Orbital forcing of the martian polar layered deposits: *Nature*, v. 419, p. 375–377.
- Lemoine, F.G., Smith, D.E., Rowlands, D.D., and 4 others, 2001, An improved solution of the gravity field of Mars (GMM–2B) from Mars Global Surveyor: *Journal of Geophysical Research*, v. 106, no. E10, p. 23,359–23,376.
- Leonard, G.J., and Tanaka, K.L., 2001, Geologic map of the Hellas region of Mars: U.S. Geological Survey Geologic Investigations Series Map I–2694, scale 1:5,000,000.
- Leverington, D.W., 2011, A volcanic origin for the outflow channels of Mars: Key evidence and major implications: *Geomorphology*, v. 132, p. 51–75 (doi:10.1016/j.geomorph.2011.05.022).
- Lucchitta, B.K., 1982, Ice sculpture in the Martian outflow channels: *Journal of Geophysical Research*, v. 87, no. B12, p. 9951–9973.
- Malin, M.C., Bell, J.F., III, Cantor, B.A., and 11 others, 2007, Context Camera investigation on board the Mars Reconnaissance Orbiter: *Journal of Geophysical Research*, v. 112, no. E5 (doi:10.1029/2006JE002808).
- Mandt, K.E., de Silva, S.L., Zimelman, J.R., and Crown, D.A., 2008, Origin of the Medusae Fossae Formation, Mars: Insights from a synoptic approach: *Journal of Geophysical Research*, v. 113, no. E12011 (doi:10.1029/2008JE003076).
- Mangold, Nicolas, Ansan, Véronique, Masson, Phillipe, and 2 others, 2008, Geomorphic study of fluvial landforms on the northern Valles Marineris plateau, Mars: *Journal of Geophysical Research*, v. 113, no. E08009 (doi:10.1029/2007JE002985).
- Maxwell, T.A., and McGill, G.E., 1988, Ages of fracturing and resurfacing in the Amenethes region, Mars: *Proceeding of the Lunar and Planetary Science Conference*, 18th, p. 701–711.
- McGill, G.E., 1989, Buried topography of Utopia, Mars: Persistence of a giant impact depression: *Journal of Geophysical Research*, v. 94, p. 2753–2759.
- McGill, G.E., 2002, Geologic map transecting the highland/lowland boundary zone, Arabia Terra, Mars—Quadrangles 30332, 35332, 40332, and 45332: U.S. Geological Survey Geologic Investigations Series Map I–2746, scale 1:1,000,000.
- McGill, G.E., 2005, Geologic map of Cydonia Mensae—southern Acidalia Planitia, Mars—Quadrangles MTM 40007, 40012, 40017, 45007, 45012, and 45017: U.S. Geological Survey Geologic Investigations Series Map I–2811, scale 1:1,000,000.
- McGovern, P.J., and Morgan, J.K., 2009, Volcanic spreading and lateral variations in the structure of Olympus Mons,

- Mars: *Geology*, v. 37, no. 2, p. 139–142 (doi:10.1130/G25180A.1).
- Mest, S.C., and Crown, D.A., 2002, Geologic map of MTM –40252 and –40257 quadrangles, Reull Vallis region of Mars: U.S. Geological Survey Geologic Investigations Series Map I–2730, scale 1:1,000,000.
- Mest, S.C., and Crown, D.A., 2003, Geologic map of MTM –45252 and –45257 quadrangles, Reull Vallis region of Mars: U.S. Geological Survey Geologic Investigations Series Map I–2763, scale 1:1,000,000.
- Mest, S.C., and Crown, D.A., 2006, Geologic map of MTM –20272 and –25272 quadrangles, Tyrrena Terra region of Mars: U.S. Geological Survey Scientific Investigations Map 2934, scale 1:1,004,000.
- Michael, G.G., 2013, Planetary surface dating from crater size–frequency distribution measurements—Multiple resurfacing episodes and differential isochron fitting: *Icarus*, v. 226, p. 885–890 (doi:10.1016/j.icarus.2013.07.004).
- Michael, G.G., and Neukum, Gerhard, 2010, Planetary surface dating from crater size–frequency distribution measurements—Partial resurfacing events and statistical age uncertainty: *Earth and Planetary Science Letters*, v. 294, p. 223–229 (doi:10.1016/j.epsl.2009.12.041).
- Michael, G.G., Platz, Thomas, Kneissl, Thomas, and Schmedemann, Nico, 2012, Planetary surface dating from crater size frequency distribution measurements: Spatial randomness and clustering: *Icarus*, v. 218, p. 169–177 (doi:10.1016/j.icarus.2011.11.033).
- Michalski, J.R., and Bleacher, J.E., 2013, Supervolcanoes within an ancient volcanic province in Arabia Terra, Mars: *Nature*, v. 502, p. 47–52 (doi:10.1038/nature12482).
- Moore, H.J., 2001, Geologic map of the Tempe Mareotis region of Mars: U.S. Geological Survey Geologic Investigations Series Map I–2727, scale 1:1,000,000.
- Moore, J.M., and Wilhelms, D.E., 2001, Hellas as a possible site of ancient ice-covered lakes on Mars: *Icarus*, v. 154, p. 258–276 (doi:10.1006/icar.2001.6736).
- Moore, J.M., and Wilhelms, D.E., 2007, Geologic map of part of western Hellas Planitia, Mars: U.S. Geological Survey Scientific Investigations Map 2953, scale 1:1,004,000.
- Morris, E.C., 1982, Aureole deposits of the Martian volcano Olympus Mons: *Journal of Geophysical Research*, v. 87, no. B2, p. 1164–1178.
- Morris, E.C., and Tanaka, K.L., 1994, Geologic maps of the Olympus Mons region of Mars: U.S. Geological Survey Miscellaneous Investigations Series Map I–2327, scales 1:2,000,000 and 1:1,000,000.
- Murchie, S.L., Mustard, J.F., Ehlmann, B.L., and 14 others, 2009, A synthesis of Martian aqueous mineralogy after 1 Mars year of observations from the Mars Reconnaissance Orbiter: *Journal of Geophysical Research*, v. 114, no. E00D06 (doi:10.1029/2009JE003342).
- Mustard, J.F., Cooper, C.D., and Rifkin, M.K., 2001, Evidence for recent climate change on Mars from the identification of youthful near-surface ground ice: *Nature*, v. 412, p. 411–414.
- Neukum, Gerhard, Basilevsky, A.T., Kneissl, Thomas, and 6 others, 2010, The geologic evolution of Mars—Episodicity of resurfacing events and ages from cratering analysis of image data and correlation with radiometric ages of Martian meteorites: *Earth and Planetary Science Letters*, v. 294, p. 204–222 (doi:10.1016/j.epsl.2009.09.006).
- Neumann, G.A., Smith, D.E., and Zuber, M.T., 2003, Two Mars years of clouds detected by the Mars Orbiter Laser Altimeter: *Journal of Geophysical Research*, v. 108, no. E4, 5023 (doi:10.1029/2002JE001849).
- Nimmo, Francis, and Tanaka, K.L., 2005, Early crustal evolution of Mars: *Annual Review of Earth and Planetary Sciences*, v. 33, p. 133–161.
- Nummedal, Dag, and Prior, D.B., 1981, Generation of Martian chaos and channels by debris flows: *Icarus*, v. 45, p. 77–86.
- Ody, Anouck, Poulet, François, Langevin, Yves, and 7 others, 2012, Global maps of anhydrous minerals at the surface of Mars from OMEGA/MEx: *Journal of Geophysical Research*, v. 117, no. E00J14 (doi:10.1029/2012JE004117).
- Osterloo, M.M., Anderson, F.S., Hamilton, V.E., and Hynek, B.M., 2010, Geologic context of proposed chloride-bearing materials on Mars: *Journal of Geophysical Research*, v. 115, no. E10012, doi:10.1029/2010JE003613.
- Parker, T.J., Saunders, R.S., and Schneeberger, D.M., 1989, Transitional morphology in west Deuteronilus Mensae, Mars—Implications for modification of the lowland/upland boundary: *Icarus*, v. 82, p. 111–145.
- Phillips, R.J., Davis, B.J., Tanaka, K.L., and 15 others, 2011, Massive CO₂ ice deposits sequestered in the south polar layered deposits of Mars: *Science*, v. 332, p. 838–841 (doi:10.1126/science.1203091).
- Phillips, R.J., Zuber, M.T., Smrekar, S.E., and 24 others, 2008, Mars north polar deposits—Stratigraphy, age, and geodynamical response: *Science*, v. 320, p. 1182–1185.
- Phillips, R.J., Zuber, M.T., Solomon, S.C., and 8 others, 2001, Ancient geodynamics and global-scale hydrology on Mars: *Science*, v. 291, p. 2587–2591, doi:10.1126/science.1058701.
- Pierce, T.L., and Crown, D.A., 2003, Morphologic and topographic analyses of debris aprons in the eastern Hellas region, Mars: *Icarus*, v. 163, p. 46–65 (doi:10.1016/S0019-1035(03)00046-0).
- Platz, Thomas, and Michael, G.G., 2011, Eruption history of the Elysium Volcanic Province, Mars: *Earth and Planetary Science Letters*, v. 312, p. 140–151 (doi:10.1016/j.epsl.2011.10.001).
- Platz, Thomas, Michael, G.G., Tanaka, K.L., and 2 others, 2013, Crater-based dating of geological units on Mars—Methods and application for the new global geological map: *Icarus*, v. 225, p. 806–827 (doi:10.1016/j.icarus.2013.04.021).
- Plaut, J.B., Safaeinili, Ali, Holt, J.W., and 5 others, 2009, Radar evidence for ice in lobate debris aprons in the mid-northern latitudes of Mars: *Geophysical Research Letters*, v. 36, no. L02203 (doi:10.1029/2008GL036379).
- Plescia, J.B., 2003, Cerberus Fossae, Elysium, Mars—A source for lava and water: *Icarus*, v. 164, p. 79–95.
- Plescia, J.B., 2004, Morphometric properties of Martian volcanoes: *Journal of Geophysical Research*, v. 109, no. E03003 (doi:10.1029/2002JE002031).

- Poulet, François, Bibring, J.-P., Mustard, J.F., and 31 others, 2005, Phyllosilicates on Mars and implications for early martian climate: *Nature*, v. 438, p. 623–627 (doi:10.1038/nature04274).
- Price, K.H., 1998, Geologic map of the Dao, Harmakhis, and Reull Valles region of Mars: U.S. Geological Survey Miscellaneous Investigations Series Map I-2557, scale 1:1,000,000.
- Putzig, N.E., and Mellon, M.T., 2007, Apparent thermal inertia and the surface heterogeneity of Mars: *Icarus*, v. 191, p. 68–94 (doi:10.1016/j.icarus.2007.05.013).
- Putzig, N.E., Phillips, R.J., Campbell, B.A., and 7 others, 2009, Subsurface structure of Planum Boreum from Mars Reconnaissance Orbiter Shallow Radar soundings: *Icarus*, v. 204, p. 443–457 (doi:10.1016/j.icarus.2009.07.034).
- Quantin, Cathy, Allemand, Pascal, Mangole, Nicolas, and Delacourt, Christophe, 2004, Ages of Valles Marineris (Mars) landslides and implications for canyon history: *Icarus*, v. 172, p. 555–572 (doi:10.1016/j.icarus.2004.06.013).
- Reed, J.C., Jr., Wheeler, J.O., and Tucholke, B.E., comps., 2005, Geologic Map of North America: Boulder, Colorado, Geological Society of America, Continent-Scale Map-001, scale 1:5,000,000.
- Robbins, S.J., and Hynek, B.M., 2012, A new global database of Mars impact craters ≥ 1 km—1. Database creation, properties, and parameters: *Journal of Geophysical Research*, v. 117, no. E05004 (doi:10.1029/2011JE003966).
- Robbins, S.J., Hynek, B.M., Lillis, R.J., and Bottke, W.F., 2013, Large impact crater histories of Mars—The effect of different model crater age techniques: *Icarus*, v. 225, p. 173–184 (doi:10.1016/j.icarus.2013.03.019).
- Rotto, Sue, and Tanaka, K.L., 1995, Geologic/geomorphologic map of the Chryse Planitia region of Mars: U.S. Geological Survey Miscellaneous Investigations Series Map I-2441, scale 1:5,000,000.
- Russell, P.S., and Head, J.W., 2003, Elysium-Utopia flows as mega-lahars—A model of dike intrusion, cryosphere cracking, and water-sediment release: *Journal of Geophysical Research*, v. 108, no. E6, 5064 (doi:10.1029/2002JE001995).
- Schultz, P.H., Schultz, R.A., and Rogers, John, 1982, Structure and evolution of ancient impact basins on Mars: *Journal of Geophysical Research*, v. 87, p. 9803–9820.
- Schultz, R.A., Moore, J.M., Grosfils, E.B., Tanaka, K.L., and Mège, Daniel, 2007, The Canyonlands model for planetary grabens—Revised physical basis and implications, in Chapman, M.G. (ed.), *The geology of Mars—Evidence from Earth-based analogs*: Cambridge, UK Cambridge University Press, p. 371–399.
- Schultz, R.A., and Tanaka, K.L., 1994, Lithospheric-scale buckling and thrust structures on Mars—The Coprates rise and south Tharsis ridge belt: *Journal of Geophysical Research*, v. 99, no. E4, p. 8371–8385.
- Scott, D.H., and Carr, M.H., 1978, Geologic map of Mars: U.S. Geological Survey Miscellaneous Investigations Series Map I-1083, scale 1:25,000,000.
- Scott, D.H., Dohm, J.M., and Zimbelman, J.R., 1998, Geologic map of Pavonis Mons volcano, Mars: U.S. Geological Survey Miscellaneous Investigations Series Map I-2561, scale 1:1,000,000.
- Scott, D.H., and Tanaka, K.L., 1981a, Mars—A large highland volcanic province revealed by Viking images, in Lunar and Planetary Science Conference, Proceedings, Houston, Texas, March 16–20, 1981, New York: Pergamon Press, v. 12B, p. 1449–1458.
- Scott, D.H., and Tanaka, K.L., 1981b, Mars—Paleostratigraphic restoration of buried surfaces in Tharsis Montes: *Icarus*, v. 45, p. 304–319.
- Scott, D.H., and Tanaka, K.L., 1982, Ignimbrites of Amazonis Planitia region of Mars: *Journal of Geophysical Research*, v. 87, no. B2, p. 1179–1190.
- Scott, D.H., and Tanaka, K.L., 1986, Geologic map of the western equatorial region of Mars: U.S. Geological Survey Miscellaneous Investigations Series Map I-1802-A, scale 1:15,000,000.
- Scott, D.H., and Zimbelman, J.R., 1995, Geologic map of Arsia Mons volcano, Mars: U.S. Geological Survey Miscellaneous Investigations Series Map I-2480, scale 1:1,000,000.
- Seidelmann, P.K., Abalakin, V.K., Bursa, Michal, and 8 others, 2002, Report of the IAU/IAG Working Group on Cartographic Coordinates and Rotational Elements of the Planets and Satellites—2000: *Celestial Mechanics and Dynamical Astronomy*, v. 82, p. 83–110.
- Sharp, R.P., 1973, Mars—Fretted and chaotic terrain: *Journal of Geophysical Research*, v. 78, p. 4073–4083.
- Skinner, J.A., Jr., and Fortezzo, C.M., 2013, The role of photogeologic mapping in traverse planning—Lessons from DRATS 2010 activities: *Acta Astronautica*, v. 90, no. 2, p. 242–263 (doi:10.1016/j.actaastro.2011.11.011).
- Skinner, J.A., Jr., Hare, T.M., and Tanaka, K.L., 2006, Digital renovation of the atlas of Mars 1:15,000,000-scale global geologic series maps [abs.]: Lunar and Planetary Science Conference XXXVII, Abstract 2331 [CD-ROM; online].
- Skinner, J.A., Jr., and Herkenhoff, K.E., 2012, Geologic map of the MTM 85200 quadrangle, Olympia Rupēs region of Mars: U.S. Geological Survey Science Investigations Map 3197, scale 1:500,000.
- Skinner, J.A., Jr., and Mazzini, Adriano, 2009, Martian mud volcanism—Terrestrial analogs and implications for formation scenarios: *Marine and Petroleum Geology*, v. 26, p. 1866–1878 (doi:10.1016/j.marpetgeo.2009.02.006).
- Skinner, J.A., Jr., and Tanaka, K.L., 2007, Evidence for and implications of sedimentary diapirism and mud volcanism in the southern Utopia highland–lowland boundary plain, Mars: *Icarus*, v. 186, p. 41–59 (doi:10.1016/j.icarus.2006.08.013).
- Skinner, J.A., Jr., Tanaka, K.L., and Platz, Thomas, 2012, Widespread loess-like deposit in the Martian northern lowlands identifies Middle Amazonian climate change: *Geology*, v. 40, no. 12, p. 1127–1130 (doi:10.1130/G33513.1).

- Smith, D.E., Zuber, M.T., Frey, H.V., and 21 others, 2001, Mars Orbiter Laser Altimeter—Experiment summary after the first year of global mapping of Mars: *Journal of Geophysical Research*, v. 106, no. E10, p. 23,689–23,722.
- Smith, D.E., Zuber, M.T., Solomon, S.C., and 16 others, 1999, The global topography of Mars and implications for surface evolution: *Science*, v. 284, p. 1495–1503.
- Smith, I.B., and Holt, J.W., 2010, Onset and migration of spiral troughs on Mars revealed by orbital radar: *Nature*, v. 465, p. 450–453 (doi:10.1038/nature09049).
- Smith, M.J., and Pain, C.F., 2009, Applications of remote sensing in geomorphology: *Progress in Physical Geography*, v. 33, no. 4, p. 568–582 (doi:10.1177/0309133309346648).
- Snyder, C.W., and Moroz, V.I., 1992, Spacecraft exploration of Mars, in Kieffer, H.H., Jakosky, B.M., Snyder, C.W., and Matthews, M.S., eds., *Mars: Tucson*, University of Arizona Press, p. 71–119.
- Squyres, S.W., Arvidson, R.E., Bell, J.F., III, and 47 others, 2004, The Spirit rover's Athena science investigation at Gusev crater, Mars: *Science*, v. 304, no. 5685, p. 794–799 (doi: 10.1126/science.3050794).
- Squyres, S.W., Arvidson, R.E., Bollen, Diane, and 51 others, 2006, Overview of the Opportunity Mars Exploration Rover Mission to Meridiani Planum—Eagle Crater to Purgatory Ripple: *Journal of Geophysical Research*, v. 111, no. E12S12 (doi:10.1029/2006JE002771).
- Squyres, S.W., Wilhelms, D.E., and Moosman, A.C., 1987, Large-scale volcano-ground ice interactions on Mars: *Icarus*, v. 70, p. 385–408.
- Tanaka, K.L., 1986, The stratigraphy of Mars, in *Proceedings of the Lunar and Planetary Science Conference*, 17th, Part 1, November, 1986: *Journal of Geophysical Research*, v. 91, supplement, no. B13, p. E139–158.
- Tanaka, K.L., 1990, Tectonic history of the Alba Patera-Ceraunius Fossae region of Mars: *Proceedings of the Lunar and Planetary Science Conference*, 20th, p. 515–523.
- Tanaka, K.L., 1997, Sedimentary history and mass flow structures of Chryse and Acidalia Planitiae, Mars: *Journal of Geophysical Research*, v. 102, no. E2, p. 4131–4149.
- Tanaka, K.L., 2005, Geology and insolation-driven climatic history of Amazonian north polar materials on Mars: *Nature*, v. 437, p. 991–994.
- Tanaka, K.L., Banerdt, W.B., Kargel, J.S., and Hoffman, Nick, 2001, Huge, CO₂-charged debris-flow deposit and tectonic sagging in the northern plains of Mars: *Geology*, v. 29, no. 5, p. 427–430.
- Tanaka, K.L., Chapman, M.G., and Scott, D.H., 1992, Geologic map of the Elysium region of Mars: U.S. Geological Survey Miscellaneous Investigations Series Map I-2147, scale 1:5,000,000.
- Tanaka, K.L., and Davis, P.A., 1988, Tectonic history of the Syria Planum province of Mars: *Journal of Geophysical Research*, v. 93, no. B12, p. 14,893–14,917.
- Tanaka, K.L., and Fortezzo, C.M., 2012, Geologic map of the north polar region of Mars: U.S. Geological Survey Science Investigations Map 3177, scale 1:2,000,000.
- Tanaka, K.L., Fortezzo, C.M., Hayward, R.K., and 2 others, 2011, History of plains resurfacing in the Scandia region of Mars: *Planetary and Space Science*, v. 59, p. 1128–1142 (doi:10.1016/j.pss.2010.11.004).
- Tanaka, K.L., Golombek, M.P., and Banerdt, W.B., 1991, Reconciliation of stress and structural histories of the Tharsis region of Mars: *Journal of Geophysical Research*, v. 96, no. E1, p. 15,617–15,633.
- Tanaka, K.L., Isbell, N.K., Scott, D.H., Greeley, R., and Guest, J.E., 1988, The resurfacing history of Mars—A synthesis of digitized, Viking-based geology: *Proceedings of the Lunar and Planetary Science Conference*, 18th, p. 665–678.
- Tanaka, K.L., and Kolb, E.J., 2001, Geologic history of the polar regions of Mars based on Mars Global Surveyor data—1. Noachian and Hesperian Periods: *Icarus*, v. 154, p. 3–21 (doi:10.1006/icar.2001.6675).
- Tanaka, K.L., and Leonard, G.J., 1995, Geology and landscape evolution of the Hellas region of Mars: *Journal of Geophysical Research*, v. 100, no. E3, p. 5407–5432.
- Tanaka, K.L., Robbins, S.J., Fortezzo, C.M., Skinner, J.A., Jr., and Hare, T.M., 2014, The digital global geologic map of Mars—Chronostratigraphic ages, topographic and crater morphologic characteristics, and updated resurfacing history: *Planetary and Space Science*, v. 95, p. 11–24, (doi:10.1016/j.pss.2013.03.006).
- Tanaka, K.L., Rodriguez, J.A.P., Skinner, J.A., Jr., and 5 others, 2008, North polar region of Mars—Advances in stratigraphy, structure, and erosional modification: *Icarus*, v. 196, p. 318–358.
- Tanaka, K.L., and Scott, D.H., 1987, Geologic map of the polar regions of Mars: U.S. Geological Survey Miscellaneous Investigations Series Map I-1802-C, scale 1:15,000,000.
- Tanaka, K.L., Skinner, J.A., Jr., Crumpler, L.S., and Dohm, J.M., 2009, Assessment of planetary geologic mapping techniques for Mars using terrestrial analogs—The SP Mountain area of the San Francisco Volcanic Field, Arizona: *Planetary and Space Science*, v. 57, p. 510–532 (doi:10.1016/j.pss.2008.06.012).
- Tanaka, K.L., Skinner, J.A., Jr., and Hare, T.M., 2005, Geologic map of the northern plains of Mars: U.S. Geological Survey Science Investigations Map 2888, scale 1:15,000,000.
- Tanaka, K.L., Skinner, J.A., Jr., and Hare, T.M., 2010, Planetary geologic mapping handbook—2010, in Bleamaster, L.F., III, Tanaka, K.L., and Kelley, M.S., eds., *Abstracts of the Annual Meeting of Planetary Geologic Mappers*, Flagstaff, AZ, 2010: Washington DC, NASA Conference Publication CP-2010-217041, appendix, 21 p.
- Tanaka, K.L., Skinner, J.A., Jr., Hare, T.M., Joyal, T., and Wenker, A., 2003, Resurfacing history of the northern plains of Mars based on geologic mapping of Mars Global Surveyor data: *Journal of Geophysical Research*, v. 108, no. E4 (doc. no: 8043, doi:10.1029/ 2002JE001908).
- Thomson, B.J., and Head, J.W., III, 2001, Utopia Basin, Mars—Characterization of topography and morphology and assessment of the origin and evolution of basin internal

- structure: *Journal of Geophysical Research*, v. 106, no. E10, p. 23,209–23,230.
- U.S. Geological Survey, 2003, Topographic map of Mars: U.S. Geological Survey Geologic Investigations Series Map I-2782, scale 1:25,000,000, two sheets.
- Varnes, D.J., 1974, The logic of geological maps, with reference to their interpretation and use for engineering purposes: U.S. Geological Survey Professional Paper 837, 49 p.
- Vaucher, Julien, Baratoux, David, Mangold, Nicolas, and 3 others, 2009, The volcanic history of central Elysium Planitia—Implications for Martian magmatism: *Icarus*, v. 204, p. 418–442.
- Watters, T.R., 1993, Compressional tectonism on Mars: *Journal of Geophysical Research*, v. 98, no. E9, p. 17,049–17,060.
- Watters, T.R., Campbell, Bruce, Carter, Lynn, and 10 others, 2007, Radar sounding of the Medusae Fossae Formation Mars—Equatorial ice or dry, low-density deposits?: *Science*, v. 318, p. 1125–1128.
- Werner, S.C., 2008, The early martian evolution—Constraints from basin formation ages: *Icarus*, v. 195, p. 45–60 (doi:10.1016/j.icarus.2007.12.008).
- Werner, S.C., 2009, The global martian volcanic evolutionary history: *Icarus*, v. 201, p. 44–68 (doi:10.1016/j.icarus.2008.12.019).
- Werner, S.C., and Tanaka, K.L., 2011, Redefinition of the crater-density and absolute-age boundaries for the chronostratigraphic system of Mars: *Icarus*, v. 215, p. 603–607, (doi:10.1016/j.icarus.2011.07.024).
- Werner, S.C., Tanaka, K.L., and Skinner, J.A., Jr., 2011, Mars—The evolutionary history of the northern lowlands based on crater counting and geologic mapping: *Planetary and Space Science*, v. 59, p. 1143–1165 (doi:10.1016/j.pss.2011.03.022).
- Wilhelms, D.E., 1990, Geologic mapping, in Greeley, Ronald, and Batson, R.M., eds., *Planetary Mapping*: New York, Cambridge University Press, p. 208–260.
- Williams, D.A., Greeley, Ronald, Ferguson, R.L., and 13 others (including the HRSC Co-Investigator Team), 2009, The circum-Hellas volcanic province, Mars—Overview: *Planetary and Space Science*, v. 57, p. 895–916 (doi:10.1016/j.pss.2008.08.010).
- Witbeck, N.E., Tanaka, K.L., and Scott, D.H., 1991, Geologic map of the Valles Marineris region, Mars: U.S. Geological Survey Miscellaneous Investigations Series Map I-2010, scale 1:5,000,000.
- Wyrick, Danielle, Ferrill, D.A., Morris, A.P., and 2 others, 2004, Distribution, morphology, and origins of Martian pit crater chains: *Journal of Geophysical Research*, v. 109, no. E06005 (doi:10.1029/2004JE002240).
- Xiao, Long, Huang, Jun, Christensen, P.R., and 4 others, 2012, Ancient volcanism and its implication for thermal evolution of Mars: *Earth and Planetary Science Letters*, v. 323–324, p. 9–18 (doi:10.1016/j.epsl.2012.01.027).
- Zimbelman, J.R., and Scheidt, S.P., 2012, Hesperian age for western Medusae Fossae Formation, Mars: *Science*, v. 336, p. 1683 (doi:10.1126/science.1221094).

Table 1. Martian epoch lower boundary ages from Michael (2013) based on the Hartmann (2004 iteration in Hartmann, 2005) and Neukum (Ivanov, 2001; Hartmann and Neukum, 2001) chronology systems derived from reference crater densities of Tanaka (1986) as updated by Werner and Tanaka (2011). Referent units are chosen from this map. ---, no data.

Epoch	Reference crater diameter (km)	Cumulative crater density (no. > reference diameter per 10 ⁶ km ²)	Start of epoch, Ga		Referent unit
			Hartmann 2004 iteration	Neukum system	
Late Amazonian	1	160	0.274	0.328	Apu
Middle Amazonian	1	600	1.03	1.23	mAl
Early Amazonian	1	2,100	3.24	3.37	eAb
Late Hesperian	5	125	3.39	3.61	IHI
Early Hesperian	5	200	3.56	3.71	eHv
Late Noachian	16	100	3.85	3.83	INh
Middle Noachian	16	200	3.96	3.94	mNh
Early Noachian	---	---	---	---	eNh

Table 2. Assigned model ages¹ for selected Mars global map units from 48 representative counting localities² sorted by latitude from north to south (compare to Platz and others, 2013).

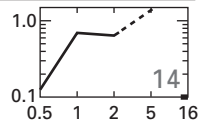
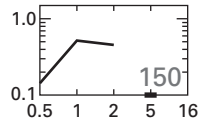
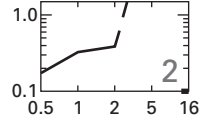
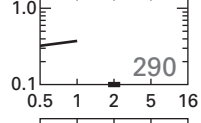
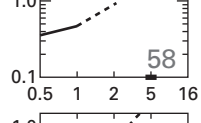
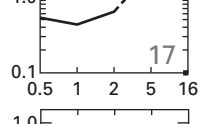

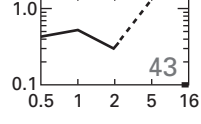
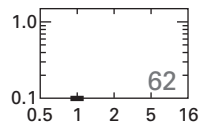
Locality Number ²	Unit label	Center coordinates of counting area ³		Area (km ²)	Age (Ga)					Epoch ⁴			Resurfacing graph ⁵
		lat °N.	long °E.		best fit	error +	error -	max. fit	min. fit	best fit	max. fit	min. fit	
1	IHl	71.10	24.78	69,980	3.51	0.10	0.38	3.61	3.13	IH	IH	eA	
					3.07	0.16	0.31	3.23	2.76	eA	eA	eA	
2	eHt	49.91	49.50	40,170	3.65	0.04	0.06	3.69	3.59	eH	eH	IH	
3	eAb	47.90	114.00	39,280	3.57	0.07	0.12	3.64	3.45	IH	eH	IH	
					1.98	0.31	0.31	2.29	1.67	eA	eA	eA	
4	Av	38.06	128.28	13,810	3.52	0.11	0.49	3.63	3.03	IH	eH	eA	
					0.728	0.095	0.095	0.823	0.633	mA	mA	mA	
5	eAb	37.95	111.20	26,100	3.33	0.11	0.26	3.44	3.07	eA	IH	eA	
					0.885	0.075	0.075	0.960	0.810	mA	mA	mA	
6	IHl	35.96	330.66	89,930	3.60	0.05	0.08	3.65	3.52	IH	eH	IH	
					2.00	0.11	0.11	2.11	1.89	eA	eA	eA	
7	mNh	35.50	47.87	48,850	3.97	0.03	0.03	4.00	3.94	eN	eN	mN	
					3.57	0.02	0.02	3.59	3.55	IH	IH	IH	
8	IHt	34.91	166.95	23,130	3.71	0.06	0.10	3.77	3.61	eH	IN	IH	
					3.20	0.14	0.35	3.34	2.85	eA	eA	eA	
					1.07	0.07	0.07	1.14	1.00	mA	mA	mA	
9	IAv	31.17	193.68	80,780	3.12	0.34	1.70	3.46	1.42	eA	IH	eA	
					0.072	0.018	0.018	0.090	0.054	IA	IA	IA	

Table 2. Assigned model ages¹ for selected Mars global map units—Continued

Locality Number ²	Unit label	Center coordinates of counting area ³		Area (km ²)	Age (Ga)					Epoch ⁴			Resurfacing graph ⁵
		lat °N.	long °E.		best fit	error +	error -	max. fit	min. fit	best fit	max. fit	min. fit	
10	IHl	29.75	108.01	30,060									
					30.27	105.85	3.62	0.05	0.07	3.67	3.55	eH	
11	IHl	26.70	106.38	27,410									
					3.53	0.07	0.13	3.60	3.40	IH	IH	IH	
12	Hto	22.84	316.70	20,360									
					1.78	0.15	0.15	1.93	1.63	eA	eA	eA	
13	INh	22.70	16.95	9,684									
					3.78	0.05	0.07	3.83	3.71	IN	IN	eH	
14	mNh	22.46	32.20	9,668									
					3.35	0.06	0.10	3.41	3.25	eA	IH	eA	
15	IHt	18.08	117.37	19,190									
					3.99	0.03	0.04	4.02	3.95	eN	eN	eN	
16	eHt	15.92	311.47	31,990									
					0.767	0.070	0.070	0.837	0.697	mA	mA	mA	
17	IHv	14.17	237.52	17,230									
					3.70	0.05	0.07	3.75	3.63	eH	IN	eH	
18	HNt	11.19	161.48	19,700									
					2.01	0.09	0.09	2.10	1.92	eA	eA	eA	
					3.72	0.03	0.04	3.75	3.68	IN	IN	eH	
					2.29	0.11	0.11	2.40	2.18	eA	eA	eA	
					3.63	0.07	0.13	3.70	3.50	eH	eH	IH	
					2.66	0.27	0.31	2.93	2.35	eA	eA	eA	
					3.91	0.08	0.18	3.99	3.73	mN	eN	IN	
					3.77	0.05	0.07	3.82	3.70	IN	IN	eH	
					1.56	0.12	0.12	1.68	1.44	eA	eA	eA	

Table 2. Assigned model ages¹ for selected Mars global map units—Continued

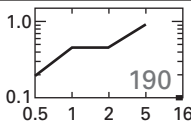
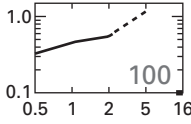
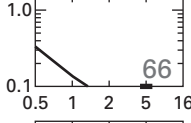
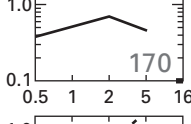
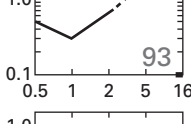
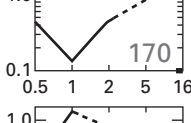
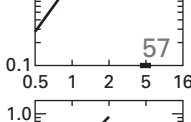
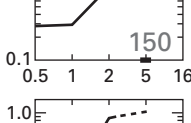
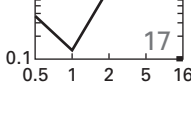
Locality Number ²	Unit label	Center coordinates of counting area ³		Area (km ²)	Age (Ga)					Epoch ⁴			Resurfacing graph ⁵
		lat °N.	long °E.		best fit	error +	error -	max. fit	min. fit	best fit	max. fit	min. fit	
19	mNh	9.52	51.36	43,600									
					3.94	0.02	0.03	3.96	3.91	mN	eN	mN	
					3.69	0.01	0.01	3.70	3.68	eH	eH	eH	
20	mNh	9.43	342.48	22,820									
					3.91	0.05	0.07	3.96	3.84	mN	eN	mN	
					3.34	0.04	0.04	3.38	3.30	eA	IH	eA	
21	IAv	5.41	177.26	45,340									
					3.37	0.18	1.50	3.55	1.87	eA	IH	eA	
					0.014	0.002	0.002	0.016	0.012	IA	IA	IA	
22	mNh	4.39	16.91	32,160									
					3.93	0.05	0.08	3.98	3.85	mN	eN	mN	
					3.68	0.02	0.02	3.70	3.66	eH	eH	eH	
23	mNh	3.98	318.74	26,290									
					3.89	0.03	0.03	3.92	3.86	mN	mN	mN	
					3.55	0.02	0.02	3.57	3.53	IH	IH	IH	
24	HNhu	2.76	355.64	11,680									
					3.91	0.04	0.05	3.95	3.86	mN	eN	mN	
					2.68	0.33	0.40	3.01	2.28	eA	eA	eA	
25	AHtu	1.16	141.90	8,208									
					3.46	0.06	0.11	3.52	3.35	IH	IH	eA	
26	Htu	0.51	148.66	20,100									
					3.70	0.04	0.06	3.74	3.64	eH	IN	eH	
					1.65	0.15	0.15	1.80	1.50	eA	eA	eA	
27	AHtu	-0.01	152.68	57,350									
					3.50	0.07	0.14	3.57	3.36	IH	IH	eA	

Table 2. Assigned model ages¹ for selected Mars global map units—Continued

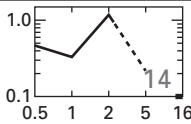
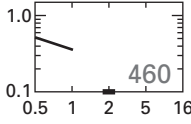
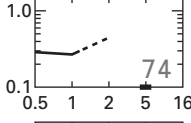
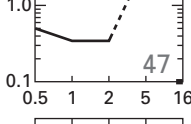

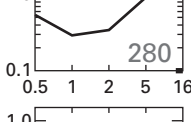
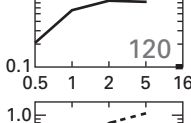
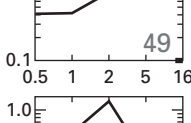
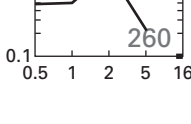
Locality Number ²	Unit label	Center coordinates of counting area ³		Area (km ²)	Age (Ga)					Epoch ⁴			Resurfacing graph ⁵
		lat °N.	long °E.		best fit	error +	error -	max. fit	min. fit	best fit	max. fit	min. fit	
28	Htu	-4.53	174.64	10,410									
					3.88	0.08	0.17	3.96	3.71	mN	eN	IN	
29	IHv	-7.50	252.99	6,508									
					2.79	0.27	0.35	3.06	2.44	eA	eA	eA	
30	AHtu	-8.12	182.28	23,890									
					3.49	0.15	2.10	3.64	1.39	IH	eH	eA	
31	mNh	-8.50	345.53	21,190									
					3.55	0.09	0.28	3.64	3.27	IH	eH	eA	
32	eNh	-14.05	49.41	19,900									
					1.59	0.20	0.20	1.79	1.39	eA	eA	eA	
33	eNh	-15.00	82.62	21,530									
					3.49	0.15	2.10	3.64	1.39	IH	eH	eA	
34	INh	-17.74	330.63	39,000									
					0.231	0.032	0.032	0.263	0.199	IA	IA	IA	
35	INh	-21.85	354.96	35,180									
					3.87	0.04	0.05	3.91	3.82	mN	mN	IN	
36	eNh	-23.57	35.53	42,060									
					3.50	0.03	0.03	3.53	3.47	IH	IH	IH	
					3.99	0.04	0.05	4.03	3.94	eN	eN	mN	
					3.50	0.02	0.03	3.52	3.47	IH	IH	IH	
					3.99	0.03	0.04	4.02	3.95	eN	eN	eN	
					3.50	0.02	0.03	3.52	3.47	IH	IH	IH	
					4.08	0.07	0.13	4.15	3.95	eN	eN	eN	
					3.79	0.02	0.02	3.81	3.77	IN	IN	IN	
					3.72	0.06	0.09	3.78	3.63	IN	IN	eH	
					3.36	0.04	0.06	3.40	3.30	eA	IH	eA	
					4.03	0.05	0.07	4.08	3.96	eN	eN	eN	
					3.82	0.02	0.03	3.84	3.79	IN	mN	IN	
					3.66	0.01	0.01	3.67	3.65	eH	eH	eH	

Table 2. Assigned model ages¹ for selected Mars global map units—Continued

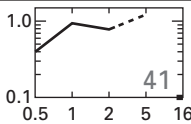
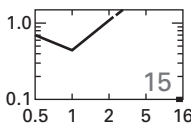
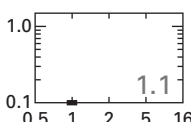
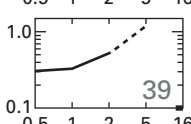
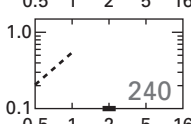
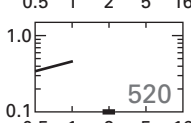
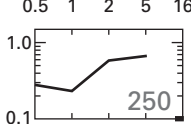
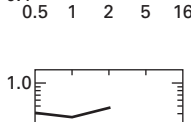

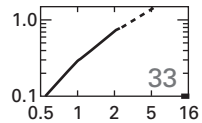
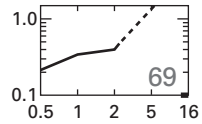
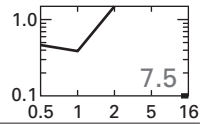
Locality Number ²	Unit label	Center coordinates of counting area ³		Area (km ²)	Age (Ga)					Epoch ⁴			Resurfacing graph ⁵
		lat °N.	long °E.		best fit	error +	error -	max. fit	min. fit	best fit	max. fit	min. fit	
37	Nhu	-27.04	288.95	19,210	3.73	0.02	0.03	3.75	3.70	IN	IN	eH	
38	eHv	-28.26	117.58	40,740	3.65	0.04	0.05	3.69	3.60	eH	eH	IH	
					3.01	0.05	0.05	3.06	2.96	eA	eA	eA	
39	IHb	-32.07	65.62	8,412	3.02	0.35	1.10	3.37	1.92	eA	eA	eA	
					0.394	0.036	0.036	0.430	0.358	mA	mA	mA	
40	HNb	-32.78	62.82	74,590	3.70	0.04	0.05	3.74	3.65	eH	IN	eH	
		-33.54	59.73		1.96	0.15	0.15	2.11	1.81	eA	eA	eA	
		-35.48	55.30										
41	eAb	-36.83	52.81	4,172	3.11	0.28	1.10	3.39	2.01	eA	IH	eA	
		-38.88	51.92		0.098	0.011	0.011	0.109	0.087	IA	IA	IA	
42	eHv	-41.92	254.04	7,631	3.59	0.08	0.16	3.67	3.43	IH	eH	IH	
					0.935	0.073	0.073	1.01	0.862	mA	mA	mA	
43	eNhm	-45.19	43.33	53,860	3.99	0.03	0.04	4.02	3.95	eN	eN	eN	
					3.87	0.02	0.02	3.89	3.85	mN	mN	mN	
					3.46	0.02	0.03	3.48	3.43	IH	IH	IH	
44	eHb	-45.99	86.77	36,310	3.78	0.03	0.04	3.81	3.74	IN	IN	IN	
					3.34	0.05	0.07	3.39	3.27	eA	IH	eA	
45	eNhm	-52.52	106.74	26,810	4.11	0.06	0.11	4.17	4.00	eN	eN	eN	
					3.31	0.09	0.18	3.40	3.13	eA	IH	eA	

Table 2. Assigned model ages¹ for selected Mars global map units—Continued

Locality Number ²	Unit label	Center coordinates of counting area ³		Area (km ²)	Age (Ga)					Epoch ⁴			Resurfacing graph ⁵
		lat °N.	long °E.		best fit	error +	error -	max. fit	min. fit	best fit	max. fit	min. fit	
46	INv	-56.66	68.40	60,380	3.89	0.08	0.21	3.97	3.68	mN	eN	eH	
					3.67	0.04	0.05	3.71	3.62	eH	eH	eH	
47	INv	-57.05	35.18	26,420	3.78	0.05	0.08	3.83	3.70	IN	IN	eH	
					2.54	0.28	0.30	2.82	2.24	eA	eA	eA	
48	Hp	-73.21	301.28	33,160	3.76	0.02	0.03	3.78	3.74	IN	IN	IN	
					3.57	0.01	0.01	3.58	3.56	IH	IH	IH	

¹Crater size-frequency distribution model absolute age and Martian epoch fits using production function of Ivanov (2001) and epoch boundaries in the Neukum chronology system as defined by Michael (2013) (see table 1 for epoch boundaries, Age Determinations section for discussion, and Platz and others (2013) for detailed analysis). Each age fit is shown on separate rows, where the oldest fit reflects the age of the unit in most cases (except for crater localities 3, 9, 15, 21, 34, 39, 44, 46, and 48). For locality 18, the first two age fits apply to unit HNT, which is a composite unit.

²Crater counting localities are documented in figure 1.

³Center coordinates of counting area; multiple coordinates indicate multiple subareas.

⁴N, Noachian; H, Hesperian; A, Amazonian; e, Early; m, Middle; l, Late.

⁵Resurfacing graphs give an at-a-glance impression of both crater density and resurfacing history (crater loss at lesser diameters) (see Platz and others, 2013). They show cumulative crater density per million square kilometers (gray digits, rounded to two significant figures) at a given reference diameter (heavy black mark on axis) and plot relative crater density in a given reference diameter interval with respect to the predicted value, based on the observed density at the next larger reference diameter (assuming the Ivanov, 2001, production function). Vertical axis shows the degree of resurfacing at a given diameter, where a value of 1.0 indicates no resurfacing, and a value of 0.1 indicates that 90 percent of the craters have been erased. The value is the ratio of the observed number of craters in the diameter interval to the number predicted from the observed number in the next larger interval using the Ivanov (2001) production function (Platz and others, 2013).

Table 3. Total crater densities for map units on Mars, based on intersection of crater center points with unit outcrops.

[Crater data are from Robbins and Hynek (2012). $N(x)$ = number of craters $> x$ km in diameter/counting area (in units of 10^6 km²). Error = (number of craters $> x$ km in diameter) $0.5 /$ counting area (in units of 10^6 km²). The impact unit is not included but has been assimilated into underlying map units to more accurately and completely measure their crater densities. See Age Determinations section and table 5 for how these data relate to unit ages]

Unit name	Unit label	Area (10 ⁶ km ²)	N(1)	Error	N(2)	Error	N(5)	Error	N(16)	Error
LOWLAND UNITS										
Middle Amazonian lowland unit	mAl	3.13	1,544.9	22.2	489.5	12.5	121.0	6.2	23.3	2.7
Late Hesperian lowland unit	lHl	17.28	1,573.5	9.5	512.4	5.4	109.7	2.5	23.8	1.2
POLAR UNITS										
Late Amazonian polar cap unit	lApc	0.70	14.3	4.5	11.5	4.1	10.0	3.8	7.2	3.2
Late Amazonian polar dunes unit	lApd	0.30	163.4	23.3	103.4	18.6	46.7	12.5	3.3	3.3
Amazonian polar undivided unit	Apu	2.00	271.3	11.7	143.6	8.5	76.6	6.2	32.0	4.0
Amazonian polar unit	Ap	0.22	808.2	60.6	254.3	34.0	113.5	22.7	22.7	10.2
Hesperian polar unit	Hp	1.35	3378.2	50.0	997.4	27.2	233.6	13.1	62.1	6.8
Hesperian polar undivided unit	Hpu	0.03	465.5	116.4	436.4	112.7	87.3	50.4	0.0	0.0
Hesperian polar edifice unit	Hpe	0.28	795.4	53.6	412.2	38.6	162.7	24.3	32.5	10.8
BASIN UNITS										
Early Amazonian basin unit	eAb	0.54	1,286.6	48.7	309.2	23.9	75.5	11.8	9.2	4.1
Late Hesperian basin unit	lHb	0.92	939.2	32.0	415.2	21.2	132.6	12.0	20.7	4.7
Early Hesperian basin unit	eHb	0.42	1,649.2	62.6	535.5	35.7	188.0	21.2	38.1	9.5
Hesperian and Noachian basin unit	HNb	0.66	1,361.1	45.5	583.3	29.8	203.6	17.6	53.2	9.0
VOLCANIC UNITS										
Late Amazonian volcanic unit	lAv	3.43	551.8	12.7	203.9	7.7	72.5	4.6	19.5	2.4
Late Amazonian volcanic field unit	lAvf	0.31	192.7	24.9	96.4	17.6	35.3	10.7	9.6	5.6
Amazonian volcanic unit	Av	2.16	772.6	18.9	255.8	10.9	74.5	5.9	7.4	1.9
Amazonian and Hesperian volcanic unit	AHv	13.33	1,303.3	9.9	339.1	5.0	85.2	2.5	16.4	1.1
Late Hesperian volcanic unit	lHv	2.47	2171.5	29.7	509.7	14.4	98.4	6.3	15.4	2.5
Late Hesperian volcanic field unit	lHvf	0.44	1670.2	61.6	402.18	30.3	111.5	15.9	15.9	6.0
Early Hesperian volcanic unit	eHv	6.24	2,960.1	21.8	820.3	11.5	246.7	6.3	73.4	3.4
Late Noachian volcanic unit	lNv	2.45	2,213.9	30.1	804.8	18.1	258.7	10.3	74.3	5.5
Amazonian volcanic edifice unit	Ave	0.82	457.7	23.6	97.4	10.9	15.8	4.4	0.0	0.0
Hesperian volcanic edifice unit	Hve	0.38	2,230.0	76.4	568.0	38.6	175.4	21.4	28.8	8.7
Noachian volcanic edifice unit	Nve	0.21	2,658.4	113.7	845.6	64.1	330.5	40.1	34.0	12.9
APRON UNITS										
Late Amazonian apron unit	lAa	0.28	158.0	23.6	63.2	14.9	14.0	7.0	0.0	0.0

Table 3. Total crater densities for map units on Mars, based on intersection of crater center points with unit outcrops.—Continued

Unit name	Unit label	Area (10 ⁶ km ²)	N(1)	Error	N(2)	Error	N(5)	Error	N(16)	Error
APRON UNITS—continued										
Amazonian apron unit	Aa	0.99	130.7	11.5	71.4	8.5	18.1	4.3	2.0	1.4
Amazonian and Noachian apron unit	ANa	0.38	1,017.7	51.5	481.5	35.4	195.2	22.2	44.2	10.7
TRANSITION UNITS										
Amazonian and Hesperian transition undivided unit	AHtu	2.23	614.5	16.6	230.7	10.2	62.8	5.3	6.7	1.7
Hesperian transition undivided unit	Htu	0.75	2,262.8	54.8	608.4	28.4	176.3	15.3	37.1	7.0
Late Hesperian transition unit	lHt	2.40	1,950.2	28.5	549.7	15.1	160.6	8.2	33.3	3.7
Early Hesperian transition unit	eHt	3.95	2,715.1	26.2	848.2	14.7	238.7	7.8	50.9	3.6
Hesperian transition unit	Ht	0.91	1,191.6	36.2	479.5	22.9	184.3	14.2	66.9	8.6
Hesperian transition outflow unit	Hto	1.35	1,868.6	37.1	481.4	18.9	130.7	9.8	32.5	4.9
Hesperian and Noachian transition unit	HNt	3.15	2,557.4	28.5	906.7	17.0	328.0	10.2	99.6	5.6
HIGHLAND UNITS										
Hesperian and Noachian highland undivided unit	HNhu	1.07	3,125.4	54.1	1185.5	33.3	379.5	18.9	109.6	10.1
Noachian highland undivided unit	Nhu	1.65	1,667.3	31.7	504.1	17.4	148.5	9.5	39.2	4.9
Early Hesperian highland unit	eHh	1.89	2,730.9	38.0	727.6	19.6	181.8	9.8	32.3	4.1
Late Noachian highland unit	lNh	8.98	3,646.9	20.1	1183.8	11.5	385.3	6.5	116.0	3.6
Middle Noachian highland unit	mNh	34.80	4,172.3	11.0	1487.1	6.5	581.1	4.1	177.4	2.3
Early Noachian highland unit	eNh	15.33	3,877.3	15.9	1481.7	9.8	665.4	6.6	249.2	4.0
Noachian highland edifice unit	Nhe	0.22	3,894.6	132.9	1459.9	81.4	702.8	56.4	172.3	27.9
Middle Noachian highland massif unit	mNhm	1.97	2,669.1	36.8	1134.5	24.0	468.7	15.4	147.3	8.6
Early Noachian highland massif unit	eNhm	1.98	2,707.9	37.0	1231.9	24.9	598.3	17.4	217.9	10.5

Table 4. Impact craters and basins (and possible impact-like features of other origin) on Mars >150 km in diameter totaling 101 in number, from largest to smallest, as identified by Robbins and others (2013).

[One feature in their database located at lat 29.9° S., long 168.6° E. is an error (S.J. Robbins, personal commun., 2013) and is not included in this table. Crater names are from the International Astronomical Union where available (see <http://planetarynames.wr.usgs.gov/>); for some unnamed craters (---), the name of a chaos feature within the crater is indicated in parentheses. Crater ages are chronostratigraphic period and epoch designations: N, Noachian; H, Hesperian; e, Early; m, Middle; l, Late. Age basis provides the primary basis for the age assignments, including crater counts in table 2, Werner (2008), and Irwin and others (2013); stratigraphic relations; and crater densities, where N(5 or 16) equals the number of superposed craters ≥ 5 or 16 km diameter per 10^6 km² using the database of Robbins and Hynek (2012). The unit(s) column shows how we mapped preserved and, in some cases, overlying surfaces of the impact features. See text for further discussion]

Crater name	Diameter (km)	Latitude (°N.)	Longitude (°E.)	Crater age	Age basis	Unit(s)
Hellas basin	~2,400	-42	71	eN	table 2	eNhm
Isidis basin	~1,500	13	89	mN	N(16)=185±20	mNhm
Argyre basin	~900	-50	318	mN	N(16)=133±10	mNhm
Huygens	467	-13.9	55.6	eN	Werner (2008)	eNh
Schiaparelli	446	-2.5	16.8	mN	N(16)=187±55	mNh
---	427	-36.8	2.8	eN	N(16)=302±47	eNh
Cassini	408	23.4	32.1	eN	N(16)=213±38	eNh
Antoniadi	401	21.4	60.8	eN	superposed by Baldet	eNh
---*	376	36.7	192.4	~N	map unit	HNt
Dollfus	359	-21.6	356.2	eN	N(16)=351±88	eNh, mNh
Tikhonravov	344	13.3	35.9	eN	N(16)=334±54	eNh
---*	341	-58.8	283.2	eN/mN	map unit	mNh
---*	340	23.5	53.2	eN	map unit	eNh
---*	327	-52.7	250.5	eN	map units	eNh, mNh, AHi
---	326	-0.4	28.9	eN	N(16)=229±45	eNh, mNh, AHi
Newton	312	-40.4	201.9	eN	N(16)=212±57	eNh, mNh
de Vaucouleurs	312	-13.3	171.1	mN	Werner (2008)	eNh, mNh
---	302	-59.9	275.9	eN	N(16)=235±65	eNh, mNh
Copernicus	302	-48.8	191.2	eN	Werner (2008)	eNh
Herschel	298	-14.5	129.9	mN	N(16)=154±40	mNh
Schroeter	292	-1.9	56.0	mN	N(16)=119±38	mNh
Koval'sky	285	-29.6	218.6	eN	map unit	eNh
---*	285	12.9	41.9	eN	buried	mNh
---	279	54.4	82.0	H/N	buried	lHi
--- (Aram Chaos)	276	2.8	338.8	mN	N(16)=196±49	mNh
Orcus Patera	263	14.2	178.6	lN	N(5)=343±83	lNh
---*	261	-4.3	333.1	N	buried	Ht, mNh
--- (Atlantis Chaos)	261	-34.4	182.4	eN	N(16)=299±86	eNh
---	257	-58.5	265.5	eN	N(16)=224±56; degraded	eNh, mNh
Newcomb	256	-24.2	1.1	eN	N(16)=229±57	eNh
---* (Gorgonum Chaos)	250	-37.7	189.3	eN	degraded	eNh, mNh
Flaugergues	236	-16.8	19.2	mN	map unit	mNh
---	229	-50.1	243.1	eN	N(16)=282±92	eNh, AHi

Table 4. Impact craters and basins (and possible impact-like features of other origin) on Mars >150 km in diameter totaling 101 in number, from largest to smallest, as identified by Robbins and others (2013).—Continued

Crater name	Diameter (km)	Latitude (°N.)	Longitude (°E.)	Crater age	Age basis	Unit(s)
Galle	223	-50.6	329.1	eA	N(5)=43±16 to 55±18	AHi
Kepler	222	-46.7	141.2	eN	N(16)=285±62	eNh
Lyot	220	50.5	29.3	eA	Werner (2008)	AHi
---*	218	43.7	18.4	N	buried, degraded	eHt, INh, ANa
Secchi	217	-57.8	102.0	mN	N(16)=103±46	mNh
---*	215	11.7	0.8	eN	buried	eNh, mNh
---*	211	-41.8	130.9	eN	degraded	eNh, mNh
Vinogradov	210	-19.8	322.3	eN	N(16)=253±64	eNh
---*	204	-42.8	215.0	eN	degraded	eNh, mNh
---*	202	47.9	89.8	N/H	buried	IHi
Kaiser	202	-46.2	19.1	eN	N(16)=339±71	eNh
Schmidt	201	-72.0	281.9	eN	N(16)=226±100	eNh
---	199	-71.1	314.2	eN	N(16)=331±162	eNh
Lowell	199	-52.0	278.6	eH	Werner (2008)	AHi
Schöner	199	19.9	50.7	eN	N(16)=436±115	eNh, mNh
Mutch	199	0.6	304.8	mN	N(16)=159±88	mNh
---*	199	-9.1	20.5	eN	degraded	eNh, mNh
---*	197	-38.2	197.5	eN	degraded	eNh, mNh
---*	197	-21.1	217.0	eN	degraded, buried	eNh, AHv
---*	195	-31.1	293.7	mN?	degraded, buried	mNh, INh
---*	195	41.8	21.9	mN?	degraded, buried	mNh, eHt, ANa
---*	194	-41.6	237.4	eN	degraded, deformed	eNh
---*	190	31.1	186.8	N	degraded, buried	HNt, IAv
---	189	-48.3	196.7	eN	N(16)=472±193	eNh, mNh
Phillips	185	-66.3	315.2	mN	map unit	mNh
Dawes	185	-9.1	38.1	eN	map unit	eNh
Green	182	-52.3	351.5	IN	N(5)=270±75	INh
Baldet	181	22.8	65.5	mN	N(16)=209±104	mNh, AHi
---*	180	-39.3	76.8	N	buried	eHb, IHb
Savich	179	-27.5	96.1	eN	N(16)=655±258	eNhm, mNh, eHv, AHi
---*	179	-11.5	356.0	eN	N(16)=477±229; buried	mNh
---*	177	-37.5	19.1	eN	degraded	eNh, mNh
Darwin	176	-57.0	341.0	eN	N(16)=241±73	eNh
Molesworth	175	-27.5	149.2	eN	N(16)=403±212	eNh
Wallace	175	-52.4	110.9	eN	N(16)=241±141	eNhm
---	175	-23.1	8.5	eN	N(16)=627±189	eNh, mNh
Flammarion	174	25.2	48.3	eN	N(16)=209±106	eNh, mNh
Terby	171	-28	74.1	eN	N(16)=426±219	eNhm, mNh, INh
---*	171	-23.7	30.4	eN	degraded	eNh, AHi

Table 4. Impact craters and basins (and possible impact-like features of other origin) on Mars >150 km in diameter totaling 101 in number, from largest to smallest, as identified by Robbins and others (2013).—Continued

Crater name	Diameter (km)	Latitude (°N.)	Longitude (°E.)	Crater age	Age basis	Unit(s)
---	169	-63.2	167.9	eN	N(16)=620±235	eNh, INh
Henry	168	10.8	23.4	eN	N(16)=248±157	eNh
Proctor	167	-47.6	29.7	eN	N(16)=409±262	eNh, mNh, INh
---*	167	-23.2	219.7	eN	degraded, buried	eNh, Nve
---	166	-18.2	1.6	eN	N(16)=259±136	eNh, mNh
---*	166	1.8	125.4	eN/mN	degraded	mNh, HNt
Becquerel	165	21.9	352.1	IN	N(5)=295±85	INh
Ptolemaeus	165	-45.9	202.3	eN	N(16)=256±148	eNh
---	164	3.2	308.0	eN	N(16)=284±128	eNh, AHi
Stoney	161	-69.6	221.6	eN	N(16)=376±213	eNh
Denning	160	-17.4	33.5	eN	N(16)=483±141	eNh, AHi
---	159	30.6	9.1	eN	N(16)=374±205	eNh
Schaeberle	159	-24.4	50.2	eN	N(16)=439±235	eNh
---*	158	-26.8	193.0	eN	degraded	eNh, mNh
Gusev	158	-14.5	175.5	eN	N(16)=899±345	eNh, mNh
Mariner	157	-34.7	195.8	eN	N(16)=587±254	eNh
Lohse	155	-43.2	343.4	mN	N(16)=104±81	mNh
Gale	154	-5.4	137.8	eH	N(5)=173±45	AHi
---	154	-51.5	231.5	eN	N(16)=405±159	eNh
---	154	-20.2	191.9	eN	N(16)=598±241	eNh, mNh
Janssen	154	2.7	37.6	mN	N(16)=117±84	mNh
Bakhuysen	153	-23.0	15.8	eH	N(5)=151±36	AHi
---*	153	-54.7	244.6	eN	buried	eNh, mNh, INh
Holden	153	-26.0	326.0	eH/IH	Irwin and Grant (2013)	AHi
Arago	152	10.2	29.9	eN	N(16)=455±254	eNh, mNh, AHi
Dejnev	152	-25.1	195.4	eN	N(16)=253±123	eNh, AHi
---*	151	6.8	182.2	N	degraded, buried	HNt, IHT
---	151	-9.0	353.1	mN	map unit	mNh

* The impact origin of these features is considered to be uncertain due to poorly preserved or inferred buried rims.

Table 5. Basis for time-stratigraphic assignments for each map unit as shown in the Correlation of Map Units.

[Key stratigraphic relations (<, younger than; ~, coeval with; >, older than) are derived from mapping observations (see Description of Map Units for more detail). Crater size-frequency data are sourced from tables 2 to 4 and from within literature references (however, not all units have useful crater size-frequency data). Locality numbers refer to specific crater size-frequency data in table 2. N(x), where x = 1, 5, or 16, refers to specific crater-density values in table 3. ---, no data]

Unit label	Key stratigraphic relations	Crater size-frequency data
LOWLAND UNITS		
mAl	< IHI; > IApd, most of Apu	Werner and others (2011); Skinner and others (2012)
IHI	< IHT, Hto; > eAb, Av	Localities 2, 6, 10, and 11; N(5); Werner and others (2011)
IMPACT UNIT		
AHi	< INh	---
POLAR UNITS		
IAPc	< Apu	---
IAPd	< mAl, most of Apu	---
Apu	< IHI, Hpu, most of Ap; > Apu	Koutnik and others (2002); Tanaka (2005); Tanaka and others (2008); Banks and others (2010)
Ap	< Hp; > most of Apu	N(1); Tanaka and Kolb (2001)
Hp	< INh; > Ap, Apu	Locality 48; N(5)
Hpu	> Apu	Tanaka and Fortezzo (2012)
Hpe	~ Hp, IHI; > Apu, mAl	N(5)
BASIN UNITS		
eAb	< IHb, IHI; ~ Av; > mAl	Localities 3, 5, 41; Tanaka and others (2005)
IHb	< eHb; > eAb	Locality 39; N(5)
eHb	< INb; > IHb	Locality 44; N(5)
HNb	< mNh; ~ INv; > eHb	Locality 40; N(5) and N(16)
VOLCANIC UNITS		
IAv	< Av; ~ IAvf	Localities 9 and 21; Tanaka and others (2005); Vaucher and others (2009); Hauber and others (2011)
IAvf	~ IAv	Tanaka and others (2005); Vaucher and others (2009); Hauber and others (2011)
Av	< IHI; ~ eAb; > mAl, IAv	Locality 4; Tanaka and others (2005)
AHv	< IHI, Hve; ~ eHv, IHv, eAb, IAvf; > Av, mAl, IAa, IAv	N(1) and N(5); Tanaka and others (2005); Hauber and others (2011)
IHv	< eHv, eHh; > AHv, AHtu, Aa	Localities 17 and 29; N(5); Dohm and others (2001a)
IHvf	< eHh; ~ IHv	N(5); Hauber and others (2011)
eHv	< INv, INh; ~ eHt, eHh; > IHv, IHT, IHI	Localities 38 and 42; Dohm and others (2001a)
INv	< mNh; ~ INh; > eHv, eHh, eHb	Localities 46 and 47; N(5) and N(16); Tanaka and Leonard (1995); Dohm and others (2001a)
Ave	~ IAvf, AHv; > IAa	N(1)
Hve	< eNhm; ~ IHv, IHvf, IHT, IHI, eHv; > AHv	N(5); Tanaka and others (1992); Tanaka and Leonard (1995); Crown and Greeley (2007); El Maary and others (2012)
Nve	~ INv, mNh, eNh; > eHv, Htu	N(5); Greeley and Crown (1992), Gregg and others (1998); Werner (2009); Xiao and others (2012)
APRON UNITS		
IAa	> Aa, Ave	---
Aa	< Av, IHT, IHv; > IAv, IAvf, IAa	N(1); Quantin and others (2004)
ANa	Noachian part: ~ Hnt, INh, mNh, eNhm. Amazonian part: < AHv, IHT	N(1) and N(16)

Table 5. Basis for time-stratigraphic assignments for each map unit as shown in the Correlation of Map Units. —Continued

Unit label	Key stratigraphic relations	Crater size-frequency data
TRANSITION UNITS		
AHtu	< Aa, Ave, IHv, eHv; ~ AHv; > IAv	Localities 25, 27, and 30; N(5); Tanaka and others (2005); Kerber and Head (2010); Zimbelman and Scheidt (2012)
Htu	< Nhu, Nve; ~ eHt, Hve; > IHt, Ht, Hto, AHtu	Localities 26 and 28; N(5); Kerber and Head (2010); Zimbelman and Scheidt (2012)
IHt	< eHt, eHv, eHh; ~ AHv; > Hto, IHI, AHtu	Localities 8 and 15; Tanaka and others (2005)
eHt	< INh; ~ eHv, Htu, HNt; > Ht, Hto, IHI, IHt, AHtu	Localities 2 and 16; Tanaka and others (2005)
Ht	< eHt, eHh, eHv; ~ Hto; > Htu, IHt	N(5)
Hto	< AHv, IHt, eHh; ~ Ht; > IHI	Locality 12; N(5); Rotto and Tanaka (1995); Tanaka (1997); Tanaka and others (2005); Chapman and others (2010)
HNt	Noachian part: ~ eNh, mNh, INh. Hesperian part: < INv; ~ eHt, eHh, Htu, Hve; > eHv, IHt, IHI, AHtu	Locality 18; N(1), N(5), and N(16); Tanaka and others (2005)
HIGHLAND UNITS		
HNhu	< eHh, INh; ~ eHb; > eHv	Locality 24; N(5) and N(16); Hynek and Phillips (2008)
Nhu	~ INh, INv, mNh, eNh; > eHt, eHv, eHt	Locality 37; Dohm and others (2001a)
eHh	< INh, INv; ~ eHv; > Hto, IHv, IHvf, IHt	N(5)
INh	< mNh, mNhm; ~ INv; > eHv, eHh, eHt, eHb	Localities 13, 34, and 35; N(5) and N(16); Dohm and others (2001a)
mNh	< eNh, eNhm; ~ mNhm; > INh, INv	Localities 7, 14, 19, 20, 22, 23, and 31; N(5) and N(16)
eNh	~ eNhm; > mNhm, mNh	Localities 32 and 36; N(16)
Nhe	~ INh, mNh, eNh; > INh, INv	N(5) and N(16); Xiao and others (2012)
mNhm	~ mNh, eNh; > INh	N(5) and N(16); N(16) for Isidis and Argyre basins; Robbins and others (2013)
eNhm	~ eNh; > mNh	Localities 43 and 45; N(16); Robbins and others (2013)

Table 6. Percentages of previously mapped Viking-based map units for each unit in this Mars global map; values <5 percent not shown.

[Former mapping from digital map of Skinner and others (2006), which was adapted from Scott and Tanaka (1986), Greeley and Guest (1987), and Tanaka and Scott (1987)]

Global map unit name, this map	Unit label	Area (10 ⁶ km ²)	Previously mapped Viking-based units (% intersect)
POLAR UNITS			
Middle Amazonian lowland unit	mAl	3.09	Am (21), Hvk (20), Hvm (18), Apk (14), Hvg (6), HNu (6)
Late Hesperian lowland unit	lHl	16.11	Hvk (31), Hvm (16), Aa ₁ (11), Hvg (11), Hvr (8), Apk (6), Am (5)
IMPACT UNIT			
Amazonian and Hesperian impact unit	AHi	7.83	cs (35), Npl ₁ (17), Hr (7), Npld (7), Npl ₂ (5)
POLAR UNITS			
Late Amazonian polar cap unit	lApc	0.70	Api (82), Apl (18)
Late Amazonian polar dunes unit	lApd	0.30	Adl (66), Adc (28), Am (5)
Amazonian polar undivided unit	Apu	2.01	Apl (79), Api (10)
Amazonian polar unit	Ap	0.22	Hnu (53), Hdl (24), Hdu (14), Am (5)
Hesperian polar unit	Hp	1.22	Hdu (53), Hdl (21), HNu (9), Npl ₂ (7)
Hesperian polar undivided unit	Hpu	0.03	Apl (52), Am (32), Hvg (14)
Hesperian polar edifice unit	Hpe	0.26	Am (55), HNu (14), Api (9), Nplh (5)
BASIN UNITS			
Early Amazonian basin unit	eAb	0.55	Ael ₃ (77), Hvg (9)
Late Hesperian basin unit	lHb	0.91	Hh ₃ (69), Hh ₂ (14), Ah ₈ (13)
Early Hesperian basin unit	eHb	0.40	Hh ₂ (77), Hh ₃ (21)
Hesperian and Noachian basin unit	HNB	0.60	Hh ₂ (28), Nple (27), Hpl ₃ (20), Hr (8), Ah ₇ (7), Ah ₆ (5)
VOLCANIC UNITS			
Late Amazonian volcanic unit	lAv	3.23	Aa ₃ (34), Achu (22), Aop (9), Aa ₄ (7), Aps (5)
Late Amazonian volcanic field unit	lAvf	0.30	Aps (21), At ₅ (18), At ₆ (16), AHcf (11), Aop (11), Apk (10), Achu (7)
Amazonian volcanic unit	Av	2.02	Ael ₃ (37), Aa ₄ (18), Aa ₃ (13), Aa ₁ (7)
Amazonian and Hesperian volcanic unit	AHv	13.44	At ₅ (21), Ael ₁ (15), Hal (13), At ₄ (9), Aam (8), AHt ₃ (6), At ₆ (5)
Late Hesperian volcanic unit	lHv	2.41	Hsu (36), Hsl (20), Hf (15), Hf (9), Hr (7)
Late Hesperian volcanic field unit	lHvf	0.45	Hsu (26), Ael ₁ (24), Htu (15), AHcf (8), Ht ₂ (6), Htm (6)
Early Hesperian volcanic unit	eHv	5.83	Hr (42), Hs (22), Hpl ₃ (8), Nf (5)
Late Noachian volcanic unit	lNv	2.32	Hr (49), Had (19), Nplr (7), Hh ₂ (5)
Amazonian volcanic edifice unit	Ave	0.83	Aos (43), AHt ₃ (37), Aau (15)
Hesperian volcanic edifice unit	Hve	0.37	v (25), Ael ₂ (23), Ahh (23), Ael ₁ (9), Hhet (6), AHa (5), AHat (5)
Noachian volcanic edifice unit	Nve	0.16	Hr (22), AHt (21), Had (20), Hap (13), AHa (13)
Late Amazonian apron unit	lAa	0.29	As (87), AHt ₃ (5)
Amazonian apron unit	Aa	0.99	Aoa ₁ (40), Aoa ₄ (24), Aoa ₃ (13), Aoa ₂ (7), Ae (5)
Amazonian-Noachian apron unit	ANa	0.28	As (53), HNu (9), Hr (7), Hch (7)
TRANSITION UNITS			
Amazonian and Hesperian transition undivided unit	AHtu	2.20	Amu (43), Amm (26), Aml (15)
Hesperian transition undivided unit	Htu	0.50	Aml (28), Amm (23), Hvl (11), Avf (7), Achu (7), Apk (6), HNu (5), Npl ₂ (5)
Late Hesperian transition unit	lHt	2.37	Aa ₁ (29), Aps (20), Hr (13), Apk (12)

Table 6. Percentages of previously mapped Viking-based map units for each unit in this Mars global map; values <5 percent not shown. — continued

Global map unit name, this map	Unit label	Area (10 ⁶ km ²)	Previously mapped Viking-based units (% intersect)
Early Hesperian transition unit	eHt	3.72	Hr (40), AHpe (11), Apk (10), Aa ₁ (8), Aps (7), HNu (7), Npld (5)
Hesperian transition unit	Ht	0.91	Hcht (58), Hch (14), Npl ₂ (7)
Hesperian transition outflow unit	Hto	1.28	Hch (33), Hchp (33), Aa ₁ (19), Hr (12)
Hesperian and Noachian transition unit	HNt	2.81	HNu (48), Apk (13), Aa ₁ (8), Npl ₂ (5)
HIGHLAND UNITS			
Hesperian and Noachian highland undivided unit	HNhu	0.36	Npl ₂ (47), Ah ₅ (21), Nple (6), Hpl ₃ (5)
Noachian highland undivided unit	Nhu	2.54	Hch (24), HNu (20), Hchp (14), Npl ₁ (8), Npl ₂ (5), Hr (5), Nf (5)
Early Hesperian highland unit	eHh	1.84	Hr (70), Hf (7), Npl ₂ (6)
Late Noachian highland unit	INh	8.78	Hr (29), Hpl ₃ (16), Npl ₂ (12), Npl ₁ (10), Nplr (7), Npld (6)
Middle Noachian highland unit	mNh	30.41	Npl ₁ (32), Npld (22), Npl ₂ (14), Hr (8), Nplr (7)
Early Noachian highland unit	eNh	16.05	Npl ₁ (36), Npld (30), Nplr (8), Npl ₂ (5)
Noachian highland edifice unit	Nhe	0.21	Npl ₁ (22), v (19), Nf (16), Nb (10), Nplh (7), Npl ₂ (6), Hr (5)
Middle Noachian highland massif unit	mNhm	1.86	Nplh (57), Hpl ₃ (15), Npld (11), Npl ₂ (6)
Early Noachian highland massif unit	eNhm	1.95	Nh ₁ (67), Nm (11), Npl ₂ (11)

Table 7. Percentages of map units in this Mars global map for each previously mapped Viking-based map unit; values <5 percent not shown. Units organized as in Tanaka and others (1988, table 1)

[Former mapping from digital map of Skinner and others (2006), which was adapted from Scott and Tanaka (1986), Greeley and Guest (1987), and Tanaka and Scott (1987)]

Previously mapped Viking-based unit name	Unit label	Area (10 ⁶ km ²)	Global map units, this map (% interscet)
SURFICIAL MATERIALS			
aeolian deposits	Ae	0.16	AHtu (50), Aa (32), IAv (16)
dune material	Ad	0.01	INh (47), eNh (27), HNhu (11), Apu (9), mNh (5)
crescentic dune material	Adc	0.46	IHI (66), IApd (18), Apu (8), mAl (7)
linear dune material	Adl	0.23	IApd (87), Apu (7), Hpe (5)
mantle material	Am	1.76	IHI (50), mAl (36), Hpe (8)
slide material	As	0.62	IAa (40), ANa (27), mNh (5), AHi (5)
polar ice deposits	Api	0.96	IAPc (60), Apu (21), IHI (14)
polar layered deposits	Apl	1.84	Apu (87), IAPc (7)
CHANNEL-SYSTEM MATERIALS			
younger channel material	Ach	0.01	mAl (52), mNh (34), IHI (8)
older channel material	Hch	1.46	Hto (29), Nhu (27), mNh (10), Ht (9), eHt (6)
younger flood-plain material	Achp	0.05	IAv (83), eHt (11), IAv (5)
older flood-plain material	Hchp	1.05	Hto (40), Nhu (22), INh (10), AHv (10)
chaotic material	Hcht	0.81	Ht (66), HNt (13), mNh (8)
younger channel system material, undivided	Achu	0.97	IAv (78), Htu (5), AHtu (5)
channel bar	b	0.04	Hto (40), Nhu (32), AHv (11), mNh (7)
LOWLAND TERRAIN MATERIALS			
Northern plains assemblage			
Arcadia Formation, member 5	Aa ₅	0.21	Av (37), IAv (29), IHt (21), IHI (11)
Arcadia Formation, member 4	Aa ₄	0.67	Av (58), IAv (36)
Arcadia Formation, member 3	Aa ₃	1.74	IAv (67), Av (16), AHv (11)
Arcadia Formation, member 2	Aa ₂	0.14	Av (56), IHI (40)
Arcadia Formation, member 1	Aa ₁	3.94	IHI (47), IHt (17), eHt (7), AHv (7), Hto (6), HNt (6)
Medusae Fossae Formation, upper member	Amu	1.00	AHtu (94)
Medusae Fossae Formation, middle member	Amm	0.89	AHtu (63), Htu (19), HNt (6), IHt (5)
Medusae Fossae Formation, lower member	Aml	0.61	AHtu (54), Htu (33), HNt (7)
Vastitas Borealis Formation, mottled member	Hvm	3.27	IHI (79), mAl (17)
Vastitas Borealis Formation, grooved member	Hvg	2.10	IHI (88), mAl (8)
Vastitas Borealis Formation, ridged member	Hvr	1.38	IHI (94)
Vastitas Borealis Formation, knobby member	Hvk	5.93	IHI (84), mAl (10), AHi (5)
smooth plains material	Aps	2.51	IHI (24), IHt (19), AHv (13), eHt (11), IAv (8), eHv (6), AHi (6), mAl (5)
etched plains material	AHpe	0.47	eHt (87), HNt (5)

Table 7. Percentages of map units in this Mars global map for each previously mapped Viking-based map unit; values <5 percent not shown.—Continued

Previously mapped Viking-based unit name	Unit label	Area (10 ⁶ km ²)	Global map units, this map (% interscet)
Eastern volcanic assemblage			
Elysium Formation, member 4	Ael ₄	0.06	Av (77), eAb (9), AHv (9)
Elysium Formation, member 3	Ael ₃	1.33	Av (58), eAb (31)
Elysium Formation, member 2	Ael ₂	0.09	Hve (91), IHvf (5)
Elysium Formation, member 1	Ael ₁	2.58	AHv (78), IAv (9)
Albor Tholus Formation	AHat	0.02	Hve (96)
Hecates Tholus Formation	Hhet	0.03	Hve (95)
Syrtis Major Formation dome	Hs d	1.35 0.01	eHv (95) mAl (69), Hpe (27)
HIGHLAND TERRAIN MATERIALS			
Western volcanic assemblage			
Olympus Mons Formation, plains member	Aop	0.45	IAv (71), AHv (9), IAvf (8), AHtu (6)
Olympus Mons Formation, shield member	Aos	0.38	Ave (93)
Olympus Mons Formation, aureole member 4	Aoa ₄	0.24	Aa (100)
Olympus Mons Formation, aureole member 3	Aoa ₃	0.13	Aa (96)
Olympus Mons Formation, aureole member 2	Aoa ₂	0.08	Aa (91), IAvf (5)
Olympus Mons Formation, aureole member 1	Aoa ₁	0.47	Aa (86), AHtu (13)
Tharsis Montes Formation, member 6	At ₆	0.67	Ahv (91), IAvf (5)
Tharsis Montes Formation, member 5	At ₅	2.99	AHv (92)
Tharsis Montes Formation, member 4	At ₄	1.21	AHv (94)
Tharsis Montes Formation, member 3	AHt ₃	1.23	AHv (63), Ave (25)
Tharsis Montes Formation, member 2	Ht ₂	0.62	AHv (88), IHvf (5)
Tharsis Montes Formation, member 1	Ht ₁	0.18	Ahv (89), AHi (8)
Alba Patera Formation, upper member	Aau	0.19	Ave (65), Ahv (35)
Alba Patera Formation, middle member	Aam	1.00	AHv (100)
Alba Paterae, lower member	Hal	1.90	AHv (92)
Ceraunius Fossae Formation	Ahcf	0.47	AHv (73), IAv (8), IAvf (7), IHvf (7)
Syria Planum Formation, upper member	Hsu	1.35	IHv (63), AHv (14), IHvf (9), eHv (8)
Syria Planum Formation, lower member	Hsl	0.59	IHv (81), eHv (16)
Hellas assemblage			
knobby plains floor unit	Ah ₈	0.12	IHb (98)
rugged floor unit	Ah ₇	0.09	HNb (44), mNh (33), INv (14), eAb (8)
reticulate floor unit	Ah ₆	0.03	HNb (95), eAb (5)
channeled plains rim unit	Ah ₅	0.46	Nhu (47), INh (28), eHv (20),
lineated floor unit	Ah ₄	0.04	IHb (95), eHb (5)
dissected floor unit	Hh ₃	0.76	IHb (83), eHb (11)
ridged plains floor unit	Hh ₂	0.81	eHb (37), HNb (21), IHb (16), INv (13)
basin-rim unit	Nh ₁	1.88	eNhm (69), mNh (15), eNh (8)

Table 7. Percentages of map units in this Mars global map for each previously mapped Viking-based map unit; values <5 percent not shown.—Continued

Previously mapped Viking-based unit name	Unit label	Area (10 ⁶ km ²)	Global map units, this map (% interscet)
Plateau and high-plains assemblage			
Valles Marineris interior deposits, floor material	Avf	0.21	IHt (32), HNhu (25), Nhu (16), Ht (14), Aa (11)
Valles Marineris interior deposits, layered material	Hvl	0.09	HNhu (86), Nhu (7), IHt (5)
Tyrrhena Patera Formation	AHt	0.05	Nve (90), eHv (10)
Apollinaris Patera Formation	AHa	0.06	Nve (46), Hve (34), HNt (12)
Hadriaca Patera Formation	AHh	0.12	Hve (75), eHv (27)
Amphitrites Formation, patera member	Hap	0.12	INv (77), Nve (23)
Amphitrites Formation, dissected member	Had	0.48	INv (89), Nve (9)
Tempe Terra Formation, upper member	Htu	0.22	eHv (46), IHvf (31), INh (7), eHh (6)
Tempe Terra Formation, middle member	Htm	0.21	eHv (50), IHv (19), IHvf (13), AHv (6)
Tempe Terra Formation, lower member	Htl	0.04	mNh (56), IHvf (21), eHv (16), AHi (8)
highly-deformed terrain materials, younger fractured material	Hdu	0.84	Hp (78), Apu (7)
Dorsa Argentea Formation, upper member	Hdl	0.49	Hp (52), INh (14), mNh (12), Ap (11), Apu (5)
plateau sequence, smooth unit	Hpl ₃	3.66	INh (37), mNh (18), eHv (13), mNhm (8), AHi (5)
plateau sequence, mottled smooth plains unit	Hplm	0.30	INh (43), mNh (25), eNh (23)
plateau sequence, subdued cratered unit	Npl ₂	8.24	mNh (56), INh (12), eNh (8), HNhu (6), AHi (5)
plateau sequence, cratered unit	Npl ₁	18.54	mNh (56), eNh (28), AHi (7)
plateau sequence, dissected unit	Npld	13.38	mNh (53), eNh (32)
plateau sequence, etched unit	Nple	2.59	mNh (50), eNh (23), HNb (6), AHi (5)
plateau sequence, ridged unit	Nplr	4.61	mNh (53), eNh (25), INh (13)
plateau sequence, hilly unit	Nplh	2.61	mNhm (41), eNh (24), mNh (19), AHi (5)
younger fractured material	Hf	1.23	IHv (28), mNh (10), eHh (9), INh (6), AHi (5), Nhu (5)
highly-deformed terrain materials, older fractured material	Nf	1.52	mNh (26), eHv (19), INh (17), IHv (14), AHv (5), Nhu (5), eHh (5), eNh (5)
highly-deformed terrain materials, basement complex	Nb	0.29	mNh (38), eNh (25), AHv (8), Nhe (8), Nhu (7), INh (6)
undivided material	HNu	3.21	HNt (44), Nhu (10), eHt (8), IHI (6), mAl (5)
volcano (relative age unknown)	v	0.31	Hve (31), eHv (19), Nhe (14), mNh (12), eNh (10), AHv (6)
mountain material	Nm	0.36	eNhm (61), eHv (7), eNh (6), mNhm (5)
mountain (relative age unknown)	m	0.03	eNh (68), mNh (11), INh (9), AHv (8)
MATERIALS THROUGHOUT MAP AREA			
knobby plains material	Apk	2.67	IHI (35), mAl (16), eHt (14), HNt (14), IHt (10)
ridged plains material	Hr	13.56	mNh (19), eHv (18), INh (18), eHt (11), eHh (9), INv (8)
impact crater material, superposed	cs	3.45	AHi (81), mNh (7)
impact crater material, partly buried	cb	1.32	eNh (44), mNh (28), AHi (11), INh (10)
impact crater material, smooth floor	s	1.01	eNh (31), INh (22), mNh (17), AHi (13)

This page intentionally left blank.